UNIVERSITÀ DEGLI STUDI DI PADOVA

Dipartimento di Fisica e Astronomia "Galileo Galilei"

Master Degree in Physics

Final Dissertation

Characterization of innovative pixel detectors with 3D technology

Thesis supervisor

Prof. Gabriele Simi

Thesis co-supervisors

Prof. Gianmaria Collazuol

Dott.ssa Serena Mattiazzo

Candidate

Federica Borgato

Academic Year 2020/2021

Contents

Abstract

During the 4th run of LHC, the collider luminosity will increase up to $5 \cdot 10^{34}$ $\mathrm{cm}^{-2}\mathrm{s}^{-1}$ and the generation of tracks inside the charge particle detectors of the experiments LHCb, ATLAS, CMS, ALICE will become so high that the pattern-recognition and reconstruction system now available will be slowed down and a great number of ghost tracks will be created, causing an inefficient extraction of signals. This thesis work is performed in the context of the TIMESPOT project (TIME and SPace real-time Operating Tracker), which ambitiously aims to develop a complete tracking demonstrator capable of coping with the extremely high instantaneous luminosities foreseen in experiments at future facilities. This demand pushes towards a new concept of vertex detector system. In particular this work will focus on silicon pixel sensors with 3D technology.

A viable strategy to overcome the limitations deriving from the planned luminosity upgrades consists of building trackers able to measure time with a precision better than 200 ps/hit. In this thesis work the aim is to study and optimize the characteristics of an innovative pixel detector with 3D-trench technology, developed in Trento at the Fondazione Bruno Kessler (FBK). Detection efficiency and time resolution are measured with a 2 MeV proton beam at AN2000 accelerator in Legnaro. A time tag system is developed and built; it is based on the scintillation light emitted by a thin layer of organic scintillator deposited above the sensor. Scintillation light is detected by a SiPM put close to the 3D device. Moreover, the uniformity of time resolution as a function of the particle hit position inside the test structure is studied with a precision of 1 μm.

Beside the time resolution study, several test structures produced at the FBK are studied and characterized. A variety of devices have been produced considering differing geometries. In particular, two batches of sensors have been realized so far, one differing from one another by the fact that the second one has a p-spray between the n-doped trench and the silicon oxide. Moreover the second batch has many more available geometries.

This work will also be the basis for the radiation damage characterization of detectors based on pixel 3D trench technology, since high luminosities planned at colliders pose strict requirements not only on spatial and time resolution, but also on radiation hardness.

Chapter 1

Introduction

1.1 The LHCb experiment

The Large Hadron Collider beauty (LHCb) is an experiment at CERN LHC and its aim is to investigate the differences between matter and anti-matter by studying the decays of heavy flavour mesons and baryons containing beauty and charm quarks. The matter anti-matter asymmetry requires a violation of the CP symmetry in the standard model, which is described in the Cabibbo–Kobayashi–Maskawa (CKM) mechanism by a single weak phase. LHCb is capable of observing CP violation effects with high precision and search for tiny deviation from the predictions of the Standard Model.
LHCb started taking data in 2010. Run 1 started with an initial center of mass energy of $\sqrt{s} = 7$ TeV, which was then increased to $\sqrt{s} = 8$ TeV, collecting an integrated luminosity of 3.23 fb^{-1}. Run 2 started after a two year shutdown, taking data at $\sqrt{s} = 13$ TeV and recording an integrated luminosity of approximately 6 fb^{-1}.
LHCb recorded the highest number of b decays of any other experiment, enlarging also its scope to the study of charm physics, W and Z measurements, jets and nuclear collisions.

In the following we will briefly describe the LHCb detector that operated in Run 1 and 2 (Section 1.1.1). Successively we will present the detector upgrade performed during Long Shutdown 2 (Section 1.1.1.6) and the plans for the future upgrades (Section 1.1.2).

1.1.1 The LHCb detector

The main mechanism for heavy-quark production at the LHC is via gluon-gluon fusion. Consequently the angular distribution of $b\bar{b}$ or $c\bar{c}$ pairs, has a peak at small angles with respect to the beam-line and the constituents of the pair are highly correlated. This fact allows the detection with good acceptance of the resulting hadrons in a rather limited solid angle [1].
The LHCb detector is a forward spectrometer installed at Intersection Point 8 of the LHC. The detector is approximately 20 m long, with maximum transverse dimensions about 6x5 m^2. Its angular acceptance is $\approx [10; 300]$ mrad in the horizontal plane, $\approx [10; 250]$ mrad in the vertical plane. This configuration allows to reconstruct the $\approx 20\%$ of all $b\bar{b}$ pairs produced [1].

The LHCb detector has been built according to many requirements. In particular the ones related to the tracking system account for the fact that proton proton collisions in the TeV center of mass energy range produce a large number of tracks per collision and, as a consequence, a high track density [2]. Therefore the detector needs to reconstruct tracks and photons with high granularity in order to reduce the rate of fake elements. In addition the momentum distribution of forward tracks is relatively soft therefore the amount of material in the active tracking volume has to be kept at minimum in order to reduce multiple scattering and secondary interactions. Finally the trigger system must be capable of reconstructing tracks within the allowed system latency.

The momenta of charged particles is measured by means of a dipole magnet which produces a vertical magnetic field, providing an integrated field of 4 Tm.
The interaction region is surrounded by a silicon VErtex LOcator detector (VELO), described in Section 1.1.1.1. The tracking system is then completed by four planar tracking stations, the TT tracker placed between the interaction point and the dipole magnet and the T1-T3 placed after the magnet; these components are described in Section 1.1.1.2. The T1-T3 stations are composed by an Inner Tracker, positioned around the beam-pipe, and by an Outer Tracker (OT) for the outer regions [1].
The Particle Identification (PID) is performed using two Ring-Imaging Cherenkov (RICH) detectors, described in Section 1.1.1.3: the first one, RICH1, is placed upstream the dipole magnet and it is used to identify particles with low momentum ($\approx$ 2 to 60 GeV/c); the second one, RICH2, is placed downstream and covers the high momentum range ($\approx$ 15 to 100 GeV/c). PID is a crucial point for LHCb experiment, by separating pions, kaons and protons produced in heavy-flavour decays [1]. Also precise reconstruction of electrons and muons is fundamental for flavour tagging.
Then there are the two calorimeters, one electromagnetic (ECAL) and one hadronic (HCAL), described in Section 1.1.1.4, supplemented by a Preshower Detector (SPD/PS). They provide identification of electrons, photons, hadrons and their energy, used at the trigger level to select candidates considering their transverse energy.
To close the detector there are five muon stations (M1 – M5), interspersed with iron filters. These are described in Section 1.1.1.5. Muons are relevant to many LHCb's measurement thanks to their clean signature.
In Figure 1.1 and 1.2 there is a schematic view of the LHCb detector.

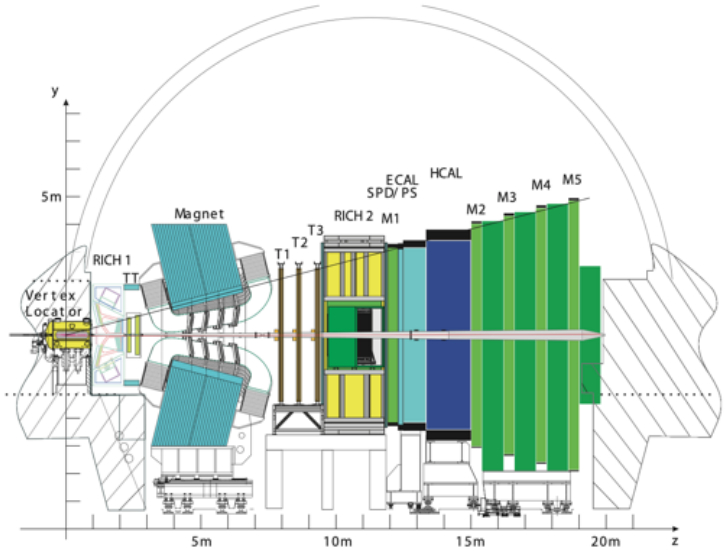

Figure 1.1: The LHCb detector: side view.

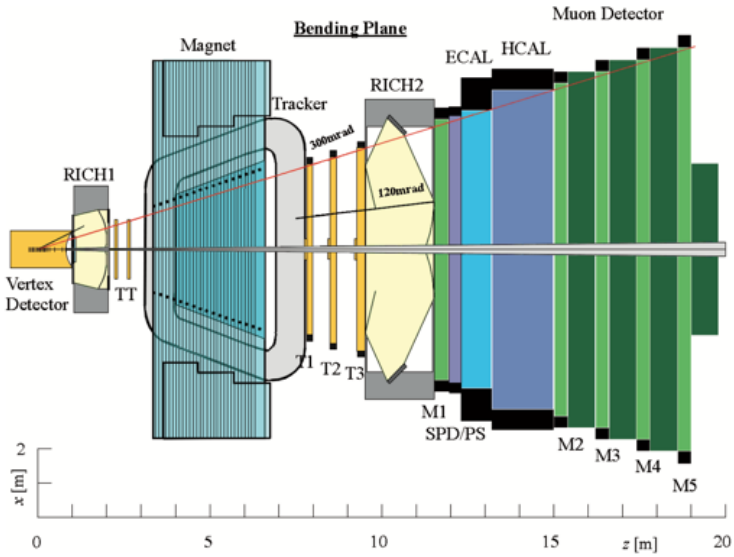

Figure 1.2: The LHCb detector: top view.

1.1.1.1 The Vertex Locator

The VELO is used to measure the impact parameter of all tracks relative to the primary (PV) and secondary vertices to reconstruct the production and decay points of hadrons containing b- and c-quarks and to allow precision measurements of their mean lifetimes. A distinctive feature of decaying beauty and charm mesons are tracks originating from secondary vertices with large impact parameters [3], so the VELO has to provide the impact parameter measurement to a high precision. This information is crucial for the trigger, that, by means of the impact parameter, apply cuts to identify interesting events.
The particles accepted by the VELO have pseudorapidities in the range $1.6 < \eta < 4.9$ and should have PVs within $|z| < 10.6$ cm from the collisional point [1].
The VELO is split in two halves composed by 21 modules, surrounding the beam pipe. Each module is divided in two Silicon half disks 300 μm thick: one has the strip in the radial direction (R sensors), another in the polar coordinate (ϕ sensors). The strips of the R sensors are separated into four 45° quadrants with the pitch ranging from $40 - 101.6$ μm. The strips of the ϕ sensors are divided into an inner and outer region with the pitch varying from $35.5 - 96.6$ μm [3]. The smaller pitches are placed the closest to the beam line, where the occupancy is the highest.
The VELO needs to be positioned the closest to the beam possible and first active silicon strips are brought to within 8.2 mm of the LHC beams [4]. The sensors operate in a "Roman pot", which means that they are located inside a secondary vacuum, separated from the primary LHC vacuum. This allows to remove them during the beam injection phases and to quickly re-insert them when the beam is stable. This is necessary because during the injection there are instabilities on the beam which induce a proton halo that would directly hit the VELO silicon detectors, damaging their crystalline structure.
For particles with transverse momentum higher than 1 GeV/c, the VELO is able to recontruct the impact parameter with a resolution less then 35 μm.

1.1.1.2 The TT and Downstream Tracking System

The purpose of the tracking system is to provide efficient reconstruction of charged-particle tracks. These information are used to determine the momenta of charged particles and to reconstruct Cherenkov rings in the RICH detectors. Its components are described in the following.
Right after the VELO, the tracking system is composed by the TT station, positioned in between the RICH1 and the magnet, and the three stations downstream the magnet.

The TT station is made of four stations grouped in pairs, called TTa and TTb, spaced by 30 cm. Each station is made of silicon microstrip planar modules. The strips of the first and the fourth stations are vertical and measure the bending x coordinate, whilst the second and third planes have stereo angles of $\pm 5°$, respectively [1].
Tracking stations T1 - T3 consist of an Inner Tracker (IT) surrounding the pipe, made of of four overlapping silicon layers, and of an Outer Tracker, that is a drift detector made of straw tubes filled with an Ar/CO_2 gas mixture.
The spatial resolutions of both the TT and IT are approximately 50 μm per hit; the straws provide a 35 ns maximum drift time and 205 μm spatial resolution. The OT spatial resolution is approximately 200 μm.

1.1.1.3 The RICH system

In order to provide an efficient Particle Identification, the RICH system is subdivided in two detectors, RICH1 and RICH2.
The design of the two subdetectors is similar and the principle of working is the following: when a charged particle hits the radiator material at the entrance of the detectors at a velocity exceeding that of light traversing the same medium, Cherenkov photons are emitted [3]. The photons are emitted in a cone and the emission angle, the Cherenkov angle, is linked to the particle velocity and the refractive index of the material. The photons are then reflected with a series of mirrors that focus them outside the LHCb acceptance on a plane filled with Hybrid Photon Detectors. In this way the Cherenkov angle is obtained, this information combined with the particle momentum extrapolated downstream the magnet allows to recover the mass of the incident particle.
The RICH1 is positioned close to the interaction point ($\approx$ 1 m), before the magnet. It has an acceptance from $\pm$25 mrad to $\pm$300mrad (horizontal plane) and to $\pm$250 mrad (vertical plane). Initially it was composed by two radiator materials: an aerogel layer 5 cm thick with refractive index n=1.03 and a C_4F_{10} gas layer of length 85 cm with refractive index n=1.0014. The former was removed during Run 2 due to occupancy reasons. The C_4F_{10} radiator is able to discriminate π/K with momenta from 10 to 60 GeV/c.
The RICH2 is positioned between T3 and the first muon station M1 and it is composed by a CF_4 gas radiator with refractive index n=1.00046. Its angular acceptance is from $\pm$15 mrad to $\pm$120 mrad (horizontal plane) and to $\pm$100 mrad (vertical plane). The RICH2 covers the high momentum range ($\approx$ 15 to 100 GeV/c).

1.1.1.4 Calorimeters

The calorimetry system is composed of four sub-detectors: the scintillator Pad Detector (SPD), the PreShower detector (PS), the Electromagnetic Calorimeter (ECAL), and the Hadron Calorimeter (HCAL). The main purpose of the LHCb calorimeter system is to trigger on electrons, photons and hadrons. It provides energy and position measurements of the particles produced in their angular acceptance and the combination of the ECAL and HCAL allows to measure photons and neutral pions. In general, the ECAL is responsible for measuring the energy of lighter particles, such as electrons and photons, the HCAL samples the energy of protons, neutrons and other particles containing quarks.

The ECAL has 66 layers of modules consisting of 2 mm of lead followed by 4 mm of scintillator material. The overall detector dimensions are 7.76x6.30 m, covering an acceptance of [25;300] mrad in the horizontal plane and [25;250] mrad in the vertical plane. The ECAL front surface is located at about 12.5 m from the interaction point and its energy resolution can be parametrized as following [5]:

$$\frac{\sigma(E)}{E} = \frac{(9.0 \pm 0.5)\%}{\sqrt{E}} \oplus (0.8 \pm 0.2)\% \oplus \frac{0.003}{Esen\theta}$$

where E is the particle energy in GeV and θ is the angle between the beam axis and a line from

the LHCb interaction point and the centre of the ECAL cell. The second contribution accounts for mis-calibrations, non-linearities, leakage; the third on is due to the electronics.

The HCAL is also a sampling calorimeter and it is constituted of iron absorber with scintillating tiles as the active material. Its thickness is 5.6 interaction lengths due to space limitations. The energy resolution estimated in test beams with pions is [5]:

$$\frac{\sigma(E)}{E} = \frac{(67 \pm 5)\%}{\sqrt{E}} \oplus (9 \pm 2)\%$$

where E is the particle energy in GeV.

1.1.1.5 The Muon System

Muons are present in the final states of many CP-sensitive B decays and play a major role in CP asymmetry and oscillation measurements, as muons from semi-leptonic b decays provide a tag of the initial state flavour of the accompanying neutral B mesons. So the detection of muons is fundamental for the LHCb experiment thanks to their clear signature. Muons are very penetrating particles, so a dedicated subsystem is necessary to detect them. In the case of LHCb, a gaseous detector is employed, since large areas needed to be covered and the occupancy is low: it detects muons through ionization, since when crossing the gas they create free electrons that drift towards the wires inducing a current in the readout detectors [3]. The gaseous detectors must be coupled with some material which absorbs everything other than muons.
The Muon System consists of five rectangular shape stations, M1-M5, placed along the beam axis. The stations are equipped with multi-wire proportional chambers (MWPC), with the exception of the inner part of the first station equipped with triple-GEM detectors [6]. MWPCs consist of gas volumes containing thin wires operated at high voltage. The complete system has an acceptance in the bending plane from 20 mrad to 306 mrad, and in the non-bending plane from 16 mrad to 258 mrad. This results in a total acceptance of about 20% for muons from semileptonic inclusive b decays [1].
The first station, M1, is placed upstream the calorimetry system and its aim is to measure precisely the muon transverse momentum, p_t, for the trigger. Concerning the other modules, they are placed downstream the calorimeters and they are interleaved with 80 cm thick iron absorbers: the minimum momentum for muons crossing the five stations is about 6 GeV/c [1]. The transverse dimensions of M2-M5 stations scale as the distance from the interaction point.

1.1.1.6 The LHCb Upgrade I

After successfully completing its first decade of data taking in the LHC Run 1 and Run 2, the LHCb has been upgraded during Long Shutdown 2. A panoramic of the modifications is displayed in Figure 1.3.

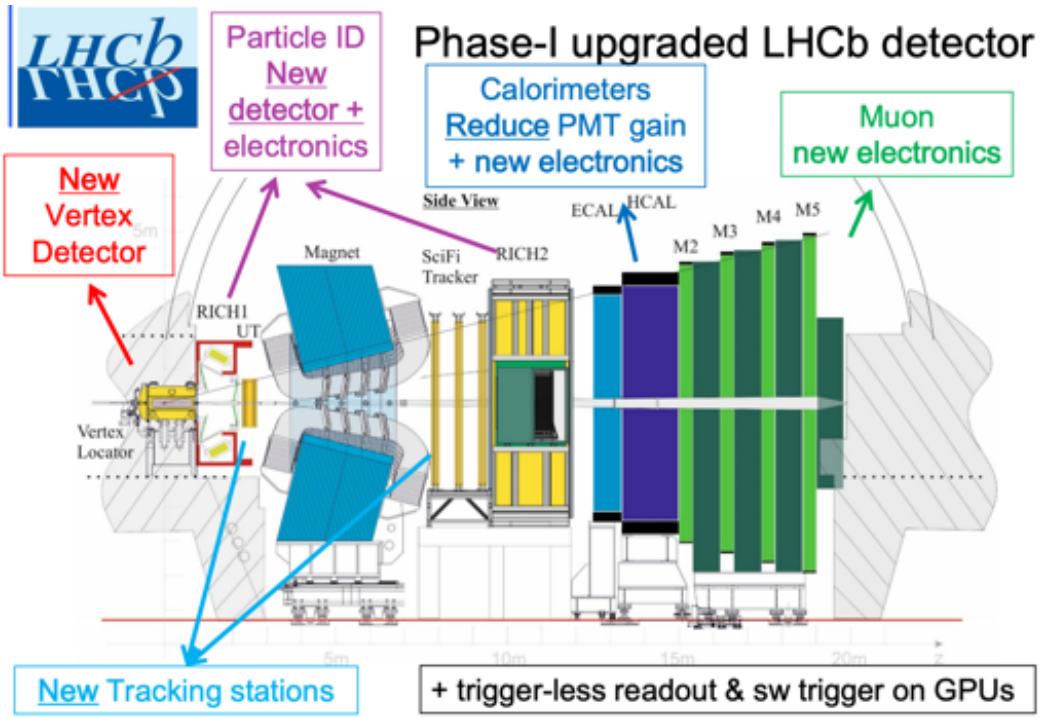

Figure 1.3: Schematic side view of LHCb Upgrade-I detector arrangement [7].

These are the major upgrades to the subdetectors:

- Trigger: design of a so-called "trigger-less" front-end electronics system capable of reading out the full detector. The hardware trigger is removed as a consequence of the increase of the output ratio to storage. Real-time event selection algorithms have been implemented, using offline quality tracks, real-time alignment and calibration.

- Upgraded VELO: the two movable halves can now move closer to the beam (5 mm to 3.5 mm) and the modules number is increased to 52.
  With the increased luminosity, the VELO will face increased occupancies, data rates and radiation damage. To cope with that, all of the VELO's silicon sensors and electronics have been replaced. To reduce occupancies, silicon hybrid pixel sensors were chosen, thanks to their high granularity [3]. In particular the modules are made of Hybrid n-on-p Pixel Silicon detectors 200 μm thick. A new cooling system has been designed to protect the very tip of the silicon from thermal runway after significant irradiation [3].
  Finally a new readout chip, the VeloPix, was developed to cope with the increased data rates.

- Upgraded Tracking System: the TT station is substituted with the Upstream Tracker (UT), composed by four layers of silicon micro-strip detector with finer granularity and closer to the beam. There is a new read-out ASIC and the Front-End electronics is mounted on the detector frame. The UT will be used for downstream reconstruction of long lived particles decaying after the VELO and it will be also essential to improve the trigger timing and the momentum resolution.
  The T1-T3 stations become a completely new detector based on Scintillating Thin Fibers (SciFi), that cover the full acceptance. There are 12 layers of modules, read out with SiPM at $-40°$. The modules will be based on 2.4 m long plastic scintillating fibres with 250 μm diameter, arranged on vertical direction [8].
  The usage of UT hits in the track extrapolation from the VELO to the SciFi detectors will allow to reduce the number of fake tracks reconstructed by the tracking algorithms, by a factor $50 - 70\%$ [8].

- Upgraded Particle ID: the Hybrid Pixel Detectors (HPD) where replaced by Multi Anode Photo-Multiplier Tubes (MaPMT) to reduce the occupancy of Cherenkov photons in the central regions of the focal plane. The 3x3 mm^2 pixels of the MaPMT are ten times smaller than those of the HPD effectively reducing the occupancy by a factor 10. In addition the optics of the detector was modified in order to optimize the contributions to the overall Cherenkov angle resolution. Finally the readout electronics was replaced with a 40 MHz capable electronics.

- Calorimetry: the previous calorimeter detectors are kept, but the PS/SPD are removed. The Front-End (FE) electronics have been redeveloped, since the upgraded trigger requires that it should work at 40 MHz. The ECAL and HCAL PMT gain will be reduced by factor of 5, to reduce PMT degradation, and, to compensate, the FE preamplifier gain is increased by a factor 5.

- Muon ID: the M1 station is removed, meanwhile M2-M5 stations are kept. The Front-End electronics have been redeveloped, in order to be adapted to the trigger-less readout.

1.1.2 The LHCb Upgrade II

During the future Run 4 and Run 5 the LHC experiments will face great challenges due to the High Luminosity Large Hadron Collider (HL-LHC) project, that is an upgrade of the LHC which aims at achieving instantaneous luminosities a factor of five larger than the LHC nominal value, thereby enabling the experiments to enlarge their data sample by one order of magnitude compared with the LHC baseline program. Such an upgrade will increase the potential for discoveries after 2027, but the LHC experiments will need as well to improve their performances in order to exploit the great enhancement in luminosity.
Concerning LHCb experiment, a Phase II upgrade is planned in order to take full advantage of the flavour physics opportunities at the HL-LHC. The Upgrade will take place during the Long Shutdown 4 of the LHC (2030).

Performing flavour physics at a luminosity of $2 \cdot 10^{34}$ $cm^{-2}s^{-1}$ presents significant challenges for the LHCb experiment, first of all the average number of interactions per bunch crossing will be of order 50, implying larger particle multiplicities and rates. Beside this fact, also the radiation damage to sub-systems will have a significant increase. Possible solutions to these challenges can be adapted to the already existing sub-systems arrangement: a schematic side view of the Phase-II detector is displayed in Figure 1.4.

In the following we sill briefly describe the current plans for the upgrade focusing on those more relevant for this work.

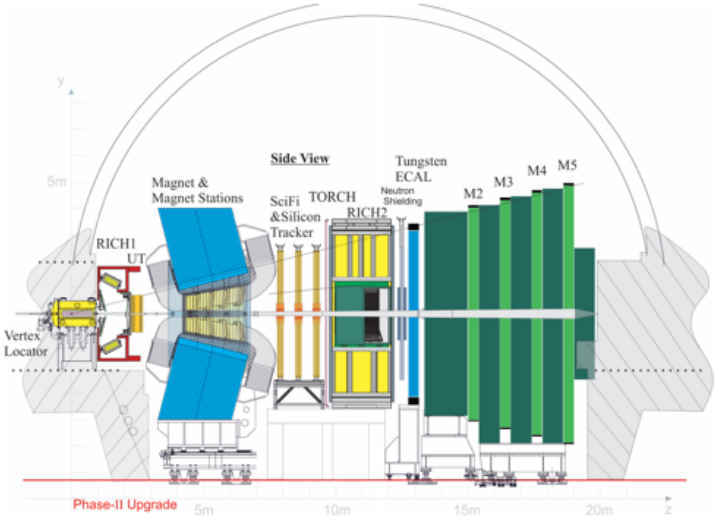

Figure 1.4: Schematic side view of LHCb Upgrade-II detector arrangement.

1.1.2.1 VELO Upgrade II

LHCb VErtex LOcator is one of the most sensitive parts to the luminosity enhancement expected with HL-LHC, since it is the subsystem closest to the beam line. There the fluence will be very intense, posing strict requirements on radiation hardness of VELO components. Moreover, at very high pile-up a fast-timing information become crucial for an experiment such LHCb, in order to avoid combinatorics and enable time-dependent CP-violating processes.
Since the bunch crossing has a finite time duration of about 180 ps, if it is possible to resolve interactions in time (within each crossing) as well as in space it would be possible to solve the complications due to the pile-up of events. But to do so, an excellent per track temporal resolution, of the order of 10 ps per hit, is required.
There is a need for R&D on achieving high-granularity 4D spatial and timing information in the VELO in this high-radiation environment. The time information will be crucial not only to better the VELO performances, but also to maintain the physics performance itself. In Figure 1.5, which displays the simulations of VELO efficiency in Primary Vertex reconstruction in function of the number of tracks, it is possible to notice that the Upgrade II VELO without the time information has significantly low efficiencies of primary vertex reconstruction, which are recovered if the timing information is considered.

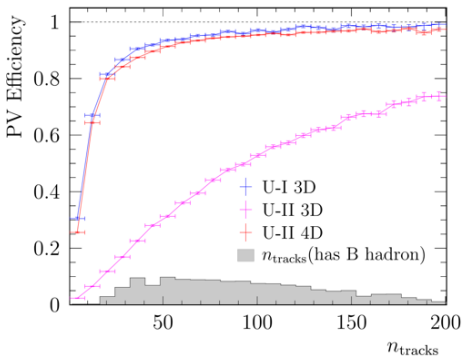

Figure 1.5: Simulations of VELO Primary Vertex reconstruction efficiency in function of the number of tracks.

Above all the possible solutions, a timing layer is not the preferred solution for LHCb Upgrade II: the technology used for the ATLAS and CMS timing layers is not directly applicable for the VELO because of the large dead region between the pixels, so a completely new technology should be implemented [9]. Moreover these timing layers are based on Low Gain Avalanch Detectors (LGADs) and at the present

time their radiation hardness is not yet sufficient for the high fluences present at the VELO level.
The 4D tracking has several advantages, such as the reduction of combinatorial tracks during pattern recognition which has a significant impact on CPU time consumed in the event filter farm. Another advantage is the reduction of ghost track candidates and a more efficient association of tracks to the primary vertex which has a significant impact on impact parameters resolution and tracking efficiency. In case of 4D tracking the timing is measured close to the primary vertex so the time measurement of slower moving particles will be less distorted [9].

Without 4D detectors the tracking performance would be highly affected by the increased luminosity and pile-up: tracking efficiency, with the integrated value within the LHCb acceptance, would fall from $\approx 99\%$ to $\approx 96\%$. These losses can be recovered with a small number of design improvements, such as decreasing the pixel pitch from 55 μm to 27.5 μm and reducing the sensor silicon thickness from 200 μm to 100 μm.

1.1.2.2 Tracking System Upgrade II

As previously mentioned, the tracking system of LHCb Upgrade I is composed by the Upstream Tracker (UT) and the three tracking station downstream the magnet. The goals for Upgrade II are to optimize the track segment matching between the detectors upstream and downstream the magnet and to improve the occupancy in the central region with finer segmentation in the tracking stations [10].
Concerning the UT, the addition of further tracking stations is considered.
For the downstream tracking stations, for the Upgrade II Inner, Middle and Outer Tracker regions are considered using a mixed technology solution: Outer Tracker region will be covered with vertical scintillating fibres, Middle and Inner Tracker will be made of silicon sensors.
Moreover the addition of tracking stations in order to perform low momentum tracking is considered. Particles with momenta lower than 1 GeV/c go out from the LHCb acceptance due to the magnetic field, and the momenta resolution of VELO and UT at this level is quite low. The idea is to instrument the internal surfaces of the magnet in the bending plane with two Magnet Stations. This would enhance the capabilities of the detector at a relatively modest cost [10].

1.1.2.3 Particle Identification with Upgrade II

The challenge for the RICH system Upgrade II will be to operate in the high radiation environment implied by the intense luminosity; this can be overcome through a natural evolution of the optics, photodetectors and readout of the existing two-RICH system.

Being able to measure the arrival time of charged particles with a precision of a few tens of ps is relevant also downstream of the dipole magnet, but in this case it is harder since there is the need to cover the acceptance of the spectrometer, which in this case imply a detector with area ≈ 30 m^2.
A possible solution can be TORCH (Time Of interally Reflected CHerenkov light) detector, an innovative time-of-flight (ToF) system based on internally-reflected Cherenkov light produced by traversing charged particles in a ≈ 1 cm thick quartz radiator [10]. The idea is to positioned it before the RICH2. The goal is to achieve a timing resolution of about 70 ps per photon and to collect approximately 30 photoelectrons per track, reaching a net precision of 15 ps.

A further possibility to improve the RICH performance is to improve the readout system of the photo detectors to measure the arrival time of the photons with a precision limited by the photodetectors itself. In the case of photomultipliers this would be about 200 ps.
In addition the extremely high luminosity will increase the occupancy in the central regions of the focal plane to very high levels. In order to keep the occupancy below $10 - 20\%$ a further reduction of the pixel size will be needed. A pixel size of 1x1 mm^2 could be achieved with SiPM readout, but in this case radiation hardness has to be verified. Other solutions based on HPD technology with a silicon pixel detector readout are being considered.

1.1.2.4 Calorimetry and Muon ID Upgrade II

For the Upgrade II the hadronic calorimeter will be removed according to the present proposal, leaving only a new electromagnetic calorimeter (ECAL), designed to work in high radiation environments. The removal of the HCAL is necessary in order to reduce the material generating secondaries in the muon chambers. In order to cope with the problems caused by overlapping clusters at high luminosity it will be necessary to change to an absorber with reduced Moliere radius, such as tungsten, and adjust the cell size accordingly [10]. Three planes of silicon pads or strips, to be evaluated whether embedded between absorber layers or behind a single converter plane at the front of the module, will provide fast timing and precise position information.

The Muon System will be reduced to four modules (M2-M5), with M2 located right after the calorimeter, and the other three stations will be embedded in the muon filter. The removal of station M1 was needed only for the hardware trigger, new off-detector readout electronics, and additional shielding in the beam-pipe region [10]. The high flux induce by the increased luminosity can be suppressed by replacing the HCAL with additional shielding.

To conclude, a brief summary of the foreseen upgrades is reported in the Table in Figure 1.6.

Detector	LS3	Phase-II
VELO	Deployment of prototype modules	New detector with fast timing
Tracking	Insert silicon IT, modify SciFi; install MS	Silicon UT and IT, SciFi OT
RICH	New photodetectors for selected regions; use of timing information	New optics; full replacement of photodetectors
TORCH	Installation for low-p hadron identification	Higher granularity photodetectors
CALO	Tungsten sampling modules installed in inner region	New modules in middle and outer regions
Muon	Replace HCAL with iron shielding; installation of high-rate chambers	Complete chamber installation
Trigger and data processing	Adiabatic software improvements; review of offline processing; installation of downstream track-finding processor	Expansion/replacement of links, readout boards and servers

Figure 1.6: Summary of the modifications under consideration for LS3, and those for Phase-II (LS4) [10].

1.2 Silicon detectors

1.2.1 Semiconductor properties

Semiconductors are a group of materials having conductivities between those of metals and insulators. The elemental materials are Silicon and Germanium.
From Quantum Mechanics one knows that an electron bound to an atom can take on only discrete values of energy, that is, the energies are quantized. Moreover since electrons are fermions (particles with spin 1/2), given Pauli exclusion principle, the probability to find two electrons in the same state is null.
These principles do not apply strictly to electrons in solid-state materials due to their crystalline structure, implying that the single atom hypothesis is not satisfied. In this case the large number of electrons and their arrangement in the regular crystalline structure causes a degeneration of the discrete energy levels in continuous energy bands separated by forbidden energy regions (Figure 1.7). The energy difference between allowed and forbidden energy bands is called "energy gap" (E_{gap}): its value characterizes the electrical properties of a material (Figure 1.8). As it is possible to see, semiconductor and insulator materials have a gap between allowed and forbidden energy bands. For Silicon $E_{gap} = 1.11$ eV [11].

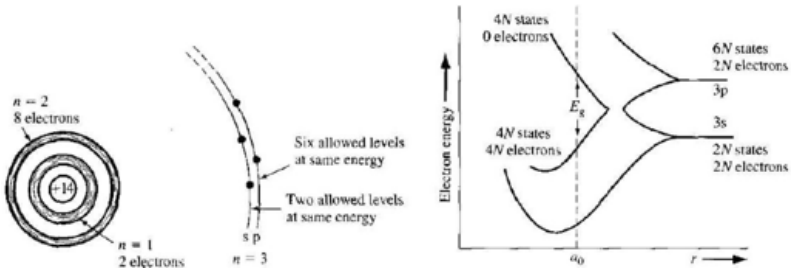

Figure 1.7: The splitting of the 3s and 3p states of Silicon into the allowed and forbidden energy bands.

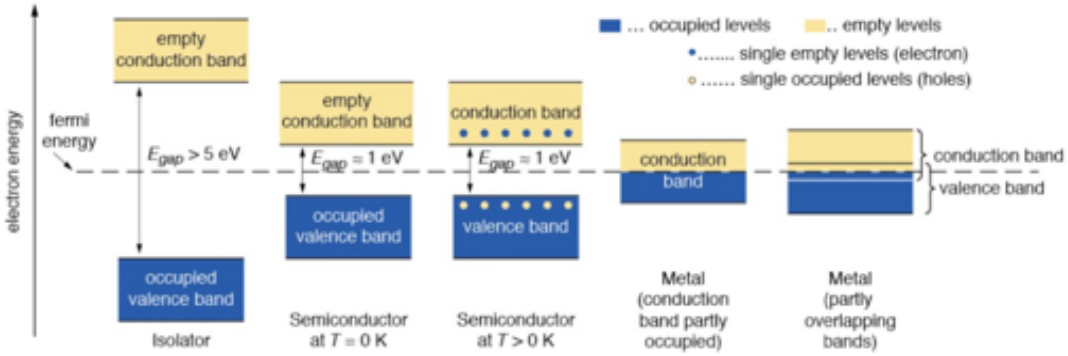

Figure 1.8: Representation of band structure for conductors, semiconductors and insulators.

Electrons follow the Fermi-Dirac statistics, with probability distribution function of the form:

$$f_F(E) = \frac{1}{1 + exp(\frac{E - E_F}{kT})}$$

The Fermi-Dirac probability distribution function is displayed in Figure 1.9. When $T = 0K$ electrons occupy the lowest energy band allowed, called *valence band*. The next one, with higher energy, can be empty or partially filled and is called *conduction band*. The Fermi level (E_F) is the energy level that has 50% probability of being occupied. For semiconductors and insulators E_F is in the band-gap, for metals is at the border of valence and conduction bands (Figure 1.8) [11].

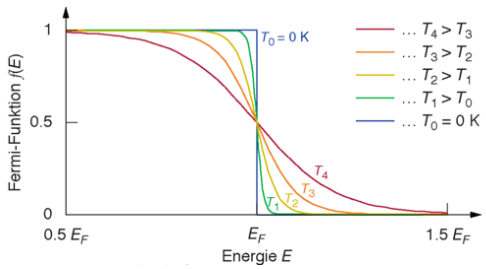

Figure 1.9: Fermi-Dirac probability distribution function at different temperatures.

When $T > 0K$ the probability that an electron has energy higher than the Fermi one is not null, thus if valence and conduction band are overlapped the material will be conductive. In the case of semiconductors, the small energy gap between valence and conduction band implies that only the most energetic electrons can occupy the latter, allowing current flow.
Since the semiconductor is neutrally charged, as the negatively charged electron breaks away from its covalent bonding position, a positively charged "empty state" is created in the original covalent bonding position in the valence band. As temperature increases, this happens more often. If an electron in the valence band at $T > 0K$ gains some thermal energy it may hop into the empty state: this is equivalent to the movement of the positively charged empty state itself. This positive charge carrier is called a *hole* [11].
Given the charge neutrality of an intrinsic semiconductor (i.e. a silicon crystal without any impurity), the number of holes in the valence band (n_p) is equal of the number of electrons in the conduction band (n_n), and can be expressed as:

$$n_i = \left(\frac{m^* k_B T}{2\pi\hbar^2}\right)^{\frac{3}{2}} \cdot e^{\frac{E_{gap}}{2kT}}$$

Typical values for n_i and E_{gap} are reported in Table 1.1.

	$n_i[cm^{-3}]$	$E_{gap}[eV]$
Silicon	$1.5 \cdot 10^{10}$	1.12
Germanium	$2.4 \cdot 10^{13}$	0.67

Table 1.1: Intrinsic electron concentration and energy gap for Silicon and Germanium at $T = 300K$.

A net current flow can be observed only in presence of an external electric field $\vec{E}$: in this condition, the drift velocity of the charge carriers can be written as:

$$\vec{v}_{p,n} = \pm\mu_{p,n} \cdot \vec{E}$$

where $\mu_{p,n}$ are the mobilities of holes and electrons, $\mu_{p,n} = \frac{e\tau_{p,n}}{m^*_{p,n}}$, with e the electron charge, $\tau_{p,n}$ the mean time between collisions for an electron, $m^*_{p,n}$ the effective mass.
Typical values for the mobilities are displayed in Table 1.2.

	$\mu_n[cm^2V^{-1}s^{-1}]$	$\mu_p[cm^2V^{-1}s^{-1}]$
Silicon	1350	480
Germanium	3900	1900

Table 1.2: Typical mobility values at $T = 300K$ and low doping concentrations.

So the total drift current density can be expressed as:

$$J_{drf} = e(\mu_n n_n + \mu_p n_p)E$$

from which one can deduce the resistivity of the semiconductor material:

$$\rho = \frac{1}{e(\mu_n n_n + \mu_p n_p)}$$

For pure Silicon at $T = 300K$ ($n_n = n_p = 1.45 \cdot 10^{10}$ cm^{-3}) the resistivity is equal to 230 Ωcm.

Another mechanism that can induce a current in the semiconductor is the carrier diffusion, that is the process whereby particles flow from a region of high concentration towards another with low concentration. This contribute can be expressed as:

$$J_{dif} = eD_n \nabla n - eD_p \nabla p$$

where $D_{n,p}$ is the electron/hole diffusion coefficient and it is a positive quantity.

Finally the total current density in a semiconductor is the sum of these four components, namely:

$$J = e\mu_n n_n E + e\mu_p n_p E + eD_n \nabla n - eD_p \nabla p$$

The electron mobility indicates how well an electron moves in a semiconductor as effect of an external electric field, the electron diffusion coefficient indicates the same but when there is a density gradient (it is the same for holes).

Mobilities and diffusion coefficients are not independent parameters and are linked by the Einstein relation, reported in Equation 1.1.

$$\frac{D_n}{\mu_n} = \frac{D_p}{\mu_p} = \frac{kT}{e} \tag{1.1}$$

1.2.2 Dopant atoms

Adding small, controlled quantities of a specific dopant, or impurity, atoms can greatly alter the electrical characteristics of the semiconductor. This process is addressed as "doping" and these semiconductors are addressed as *extrinsic*.
Silicon atoms have four valence electrons, which are shared with the four closest Silicon atoms in the lattice by means of double covalent bonds (Figure 1.10, left).

Now let's suppose to add to the lattice an atom from the group V, such as Phosphorus, as a substitutional impurity (Figure 1.10, center). Group V elements have five valence electrons: four will form covalent bonds with the nearby Silicon atoms, meanwhile the fifth one (called donor electron) will stay loosely bound to the Phosphorus atom. The energy required to promote the donor electron to the conduction band is significantly less then the one needed to promote the electrons involved in the covalent bond: a small amount of thermal energy can be enough to elevate the donor electron to the conduction band, that can now move through the crystal generating current.
The Phosphorus atom without the donor electron is positively charged; it donates an electron to the conduction band and so it is called a *donor impurity atom*. This kind of impurities allow to add electron to the conduction band without generating holes in the valence band.
A semiconductor with such impurities is referred as *n-type* semiconductor [11].

Now let's add to the lattice an atom from the group III, such as Boron, as a substitutional impurity (Figure 1.10, right). Group III elements have three valence electrons, all involved in covalent bonds

with the nearby Silicon atoms. One covalent bond is empty. Valence electrons may gain a small amount of thermal energy and move about in the crystal, so that the "empty" state becomes occupied leaving another empty state in the valence band. These other vacated electron positions can be thought of as holes in the semiconductor material. So the hole can move in the valence band leaving the negatively charged Boron atom fixed.
The Boron atoms accepts electrons from the valence band and so it is called a *acceptor impurity atom*. This kind of impurities allow to add holes to the valence band without generating electrons in the conduction band.
A semiconductor with such impurities is referred as *p-type* semiconductor [11].

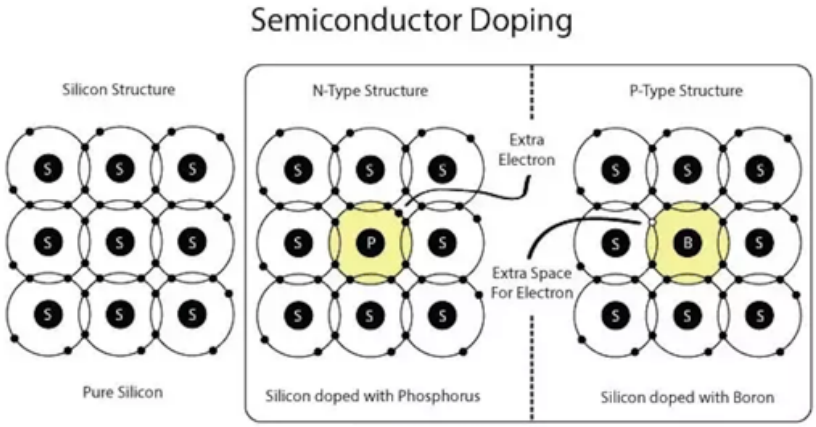

Figure 1.10: Two-dimensional representation of the intrinsic silicon lattice (left), of the silicon lattice doped with a Phosphorus atom (center), of the silicon lattice doped with a Boron atom (right).

It can be shown that adding dopants to the silicon lattice makes the Fermi energy shift closer to the conduction band for the n-type semiconductors, closer to the valence band for the p-type semiconductors. Moreover for extrinsic semiconductors at thermal equilibrium the following charge carrier density relation still holds:

$$n_i^2 = n_0 \cdot p_0$$

where n_0 is the electrons concentration, p_0 is the holes concentration, and n_i is the intrinsic carrier concentration that can be thought as a parameter describing the semiconductor material.
This relation derives from the fact that electrons and holes follow the Fermi-Dirac statistics and share the same Fermi energy.

1.2.3 The p-n junction

Large signal and low noise are two of the main requirements for a particle detector. Let's consider the case of an intrinsic Silicon device. Given that its mean ionization energy is $I_0 = 3.62$ eV and a Minimum Ionizing Particle (MIP) mean energy loss per flight path is $dE/dx = 3.87$ MeV/cm, assuming a detector with a thickness of $d = 100$ μm and an area of $A = 1$ cm^2, the signal produced by a MIP in such a detector will be:

$$\frac{dE/dx \cdot d}{I_0} \approx 3.2 \cdot 10^4 \quad e^- h^+\text{-pairs}$$

Meanwhile the number of intrinsic charge carriers in the same volume at $T = 300K$ is:

$$noise = n_i \cdot d \cdot A \approx 4.35 \cdot 10^8 \quad e^- h^+\text{-pairs}$$

This means that the number of thermal created $e^- h^+$-pairs is four orders of magnitude larger than the signal.

The only way to decrease the noise is to create a region in the detector where no mobile charge carriers are present: this can be obtained exploiting the properties of p-n junctions.

A p-n junction is an intrinsic semiconductor into which donor and acceptor impurities are diffused. This kind of semiconductor is a single-crystal material in which one region is doped with acceptor impurity atoms to form the p region and the adjacent region is doped with donor atoms to form the n region. The interface between the p-doped and n-doped region is called "metallurgical junction".
At first in the metallurgical junction there is a strong gradient of electrons and holes concentrations: the majority carriers of the n-doped region will diffuse in the p-doped region and, in the same way, the majority carriers of the p-doped region will diffuse in the n-doped region.
During this charge carriers migration process, holes diffusing in the n-doped region will uncover the respective acceptor atoms, and same the electrons with the donor atoms. The net positive and negative charges in the n and p regions induces an electric field near the metallurgical junction, with verse from the positive to the negative charge (i.e. from the n-doped region to the p-doped one). The electric field opposes to the charge carrier diffusion and at thermal equilibrium the diffusion force and the E-field force exactly balance each other (Equations 1.2 and 1.3) [11].

$$eD_n \frac{dn_n}{dx} + e\mu_n n_n E = 0 \tag{1.2}$$

$$eD_p \frac{dn_p}{dx} + e\mu_p n_p E = 0 \tag{1.3}$$

This implies the induction of the "built-in potential", V_{bi}, and of the so called "depletion region" or "space charge region", in which there are no free charge carriers (Figure 1.11).

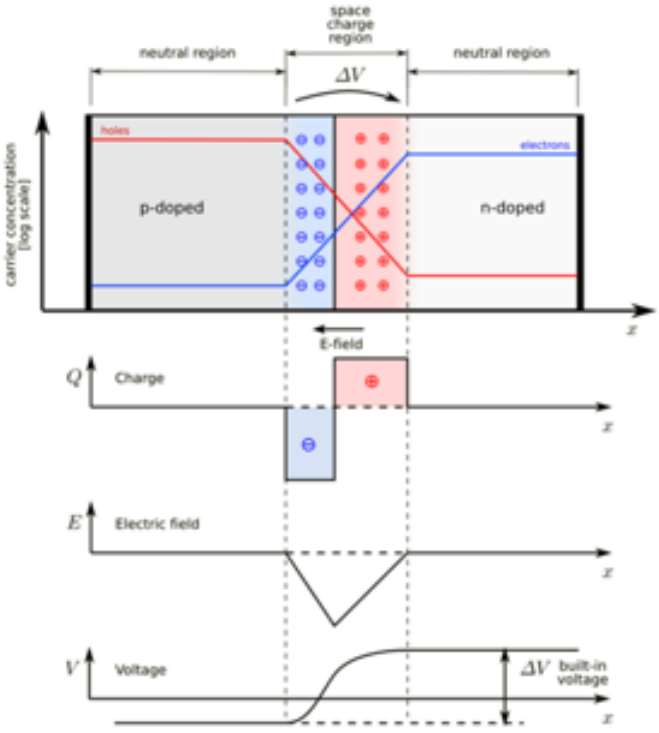

Figure 1.11: The p-n junction.

It can be demonstrated [11] that the depletion region extensions into the p and n region (respectively W_p and W_n) is given by Equation 1.4 and 1.3 and is a function of the doping concentration N_A (acceptor concentration) and N_D (donor concentration).

$$W_n = \sqrt{\frac{2\epsilon_s V_{bi}}{e} \frac{N_A}{N_D(N_A + N_D)}} \tag{1.4}$$

$$W_p = \sqrt{\frac{2\epsilon_s V_{bi}}{e} \frac{N_D}{N_A(N_A + N_D)}} \tag{1.5}$$

$$W = W_n + W_p = \sqrt{\frac{2\epsilon_s V_{bi}}{e} \frac{(N_D + N_A)}{N_A N_D}} \tag{1.6}$$

Opportunely tuning the doping concentration and applying an external potential to the p-n junction it is possible to extend the depletion region.
The bias voltage applied is called "reverse" if the positive pole is applied to the n-type substrate and the negative pole to the p-type one. This configuration allows to increase the total potential barrier of the junction, thus enlarging the depletion region (substituting $V_{tot} = V_{bi} + V_R$ to V_{bi} in Equation 1.6, with V_R the reverse bias).
It can be demonstrated [11] that the capacitance of the junction in reverse bias conditions is:

$$C = \sqrt{\frac{e\epsilon_s N_A N_D}{2(V_{bi} + V_R)(N_A + N_D)}} = \frac{\epsilon_s A}{W} \tag{1.7}$$

Measuring the device capacitance is therefore an effective way to estimate the full depletion voltage.

The bias voltage applied is called "forward" if the positive pole is applied to the p-type substrate and the negative pole to the n-type one. This implies a lowering of the voltage inside the p-n junction and the device allow the current to flow, eliminating the depletion zone. This kind of conditions are not suitable to build a detector.

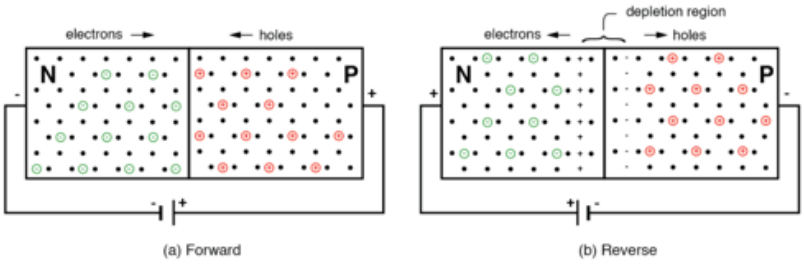

Figure 1.12: The p-n junction in forward bias conditions (a) and reverse bias conditions (b).

In forward bias the current flowing in the device grows as an exponential, in reverse bias it behaves as a constant, the so called "leakage current". For high reverse bias voltages, the current flow has a great enhancement and the voltage at which this happens is called "breakdown voltage".
A current-voltage characteristics is displayed in Figure 1.13.

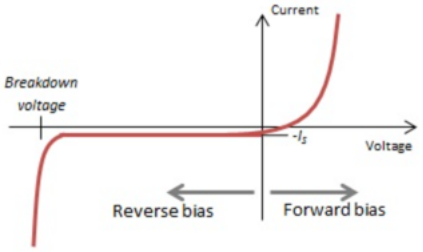

Figure 1.13: Typical current-voltage characteristics of a p-n junction.

1.2.3.1 Breakdown voltage

In the case of an ideal p-n junction, the reverse bias can assume any values and increase without any limit. But in the real case, at some particular voltage the current start to increase rapidly: a breakdown has happened.
Two physical mechanisms can produce the breakdown phenomena:

- *Avalanche effect*: electrons and/or holes moving across the depletion region can acquire enough energy from the electric field to create $e^- h^+$ pairs colliding with the atomic electrons inside the depletion zone. Then the newly created pairs contribute to the reverse bias current and can gain sufficient energy to ionize other atoms. In this way the breakdown occurs.
  For most p-n junctions, the predominant effect to induce breakdown is the avalanche effect [11].
- *Zener effect*: it happens in presence of highly doped p-n junction. In this condition valence and conduction band are so close during reverse bias that electrons could tunnel directly form the valence band on the p side to the conduction band on the n side, thus inducing a breakdown [11].

The breakdown voltage is a relevant quantity when characterizing a Silicon device, since it sets the voltage range that can be used without inducing damage on the sensor itself. Its value is strongly dependent on the geometry of the sensor, on temperature and on the thermal history of the sensor itself.

1.2.3.2 Leakage current

Leakage current is an important parameter when characterizing a silicon device as well, since it is related to its noise. It consists of thermally generated $e^- h^+$ couples which can not recombine due to the presence of the electric field.
Leakage current depends on temperature and it is a sensible quantity for radiation damage. It has multiple components, as shown in Equation 1.10 [12].

$$I_{leakage} = I_{gen} + I_{diff} + I_{surf} \tag{1.8}$$

- I_{gen} comes from the thermal generation of charge carriers in the depletion region;
- I_{diff} comes from diffusion of the minority carriers from the quasi-neutral region to the depletion region;
- I_{surf} is the current generated inside the depletion zone at the surface of the Silicon Dioxide passivation layer.

1.2.4 Radiation damage

Tracking detectors are usually the subsystems closest to the beam-line and so they undergo severe damage induced by radiation. This kind of detector is exposed to a mixed radiation field following a negative exponential law, which depends on the radial distance from the beam axis and also form the distance from the point of interaction.
From the practical point of view, radiation damage in silicon sensors can be subdivided in *surface damage* and *bulk damage*.

1.2.4.1 Surface damage

Surface passivation is a fundamental step for any Silicon device since it gives protection from any external agent or mechanical damage. Typically passivation is performed with 1 μm of Silicon Dioxide (SiO_2) [12].
It is known that Silicon Dioxide contains defects, which acts as charge traps. These can be subdivided in *interface trapped charge*, caused by structural or oxidation defects, which leads to an increase of

leakage current due to an increase in surface carriers generation-recombination; *oxide charge*, which can be due to ionic impurities or to exposure to ionizing radiation.
The main consequence of irradiation is that the properties of these defects can be modified. If the ionizing radiation is energetic enough, it can create electron-hole pairs in the oxide: some of them will recombine, but some of them will not since electrons have mobilities much higher than holes in the oxide. This fact implies that the former will quickly escape, meanwhile the latter will be trapped in the Si-SiO_2 interface. The overall result in an increase of positive charges in the oxide [12].

Let's consider a 3D sensor with substrate p-doped and readout electrodes n^+-doped. A reference image is Figure 1.20. The main consequences of ionizing radiation surface damage on this kind of sensors is firstly the overall change in charge concentration due to the presence of positive charge trapped in the oxide, in particular:

- segmentation defined by n^+ implanted electrodes are not well isolated and can eventually short. This would catastrophically compromise the position resolution;
- adjacent regions could show parasitic capacitance;
- in the Si-SiO_2 interface the electric field distribution is modified, possibly leading to anticipated breakdown.

Another ionizing radiation effect is the increase of interface states, thus implying higher surface recombination velocity and surface-related leakage current.

To minimize these effects there are two well known solutions:

1. *p-spray*: it is a medium-dose implantation of p dopant on the n^+ side of the wafer. This provide a charge compensation of the surface electron layer, since due to irradiation there is a prevalence of positive charges trapped in the oxide. The main disadvantage is that this technique implies rather low breakdown voltages before irradiation, due to the high-doping concentration of the p-spray region in contact with the n^+ electrodes. Moreover a larger inter electrode capacitance is observed.
2. *p-stop*: these are localized high-dose p^+ implants surrounding the n^+ electrodes, in order to interrupt the surface electron layer. Breakdown voltage with P-stop implants typically is high before irradiation, then starts decreasing. Inter electrodes capacitance increases with the charge oxide concentration.

1.2.4.2 Bulk damage

Bulk damage is typically caused by hadrons like protons, pions, neutrons or by highly energetic leptons as electrons and muons. The damage depends on the loss of kinetic energy of the particles going through the Silicon lattice: if the energy of the traversing particle is higher than the displacement threshold energy ($E_d = 25$ eV) then there will be a displacement of a primary knock-on atoms, implying the formation of an interstitial vacancy pair. When these pairs interact with impurities in the lattice they can form stable defects.
The displacement damage in silicon devices is quantified by the non-ionizing energy loss (NIEL). Typically fluences are expressed in terms of 1 MeV neutrons fluence, considering the so called "hardness factor", k, which is characteristics for each different radiation source [12].

The defects induced by displacements into the Silicon lattice translates to the creation of energy level inside the forbidden gap, behaving like acceptors or donors. This fact enhances the generation–recombination processes in silicon, so considering inverse bias p-n junctions the leakage current will have a significant increase, affecting the signal to noise performance of the detector.
Performing measurements on different irradiated devices, it was seen that the increase in leakage cur-

rent is linearly proportional to the irradiating fluence, Φ_{eq}, as reported in Equation 1.9, in which α is the so called damage parameter and V is the volume of the sensor depleted.

$$\Delta I = \alpha \cdot \Phi_{eq} \cdot V \tag{1.9}$$

In Figure 1.14 it is possible to see the linear trend of the increase of leakage current for several different semiconductors.

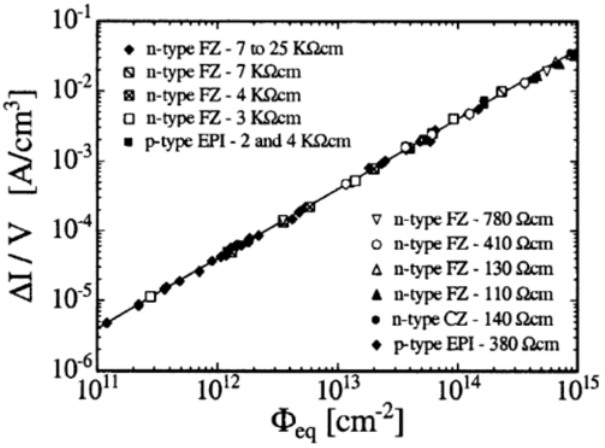

Figure 1.14: Damage-induced bulk current as function of particle fluence for different detector types [12].

Leakage currents at different temperatures can be correlated by Equation 1.10, in which T_R is the reference temperature, usually 20°, E_{eff} is the effective band gap ($\approx 1.21eV$), k_B is the Boltzmann constant. So the damage-induced leakage current can be annealed at high temperatures.

$$I(T_R) = I(T) \cdot \left(\frac{T_R}{T}\right)^2 \cdot exp\left[-\frac{E_{eff}}{2k_B} \cdot \left(\frac{1}{T_R} - \frac{1}{T}\right)\right] \tag{1.10}$$

Given that displacement defects behave as donors or acceptors depending on their position on the band gap, they can affect the full depletion voltage and also the effective polarity of the space charge. Since defects alters the effectiveness of the doping, after irradiation the doping concentration can not be well approximated with the concentration of donor atoms, N_D, or acceptor atoms, N_A: it is useful to define the "effective doping", N_{eff}. In Figure 1.15 it is possible to see that after a certain fluence the n-type semiconductor start behaving as a p-type [12].

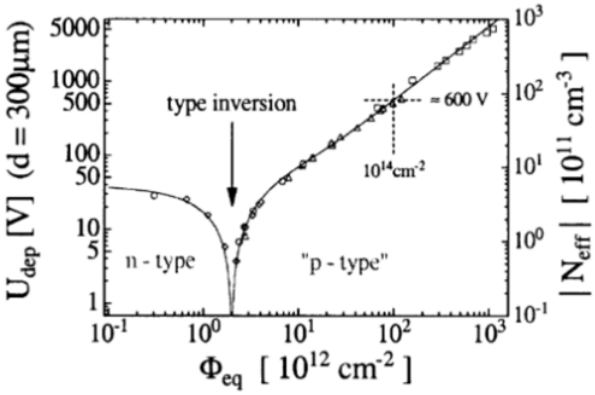

Figure 1.15: Variation of the effective doping concentration of an n-type silicon sensor as a function of the equivalent particle fluence.

Finally, one of the main consequences of charge trapping in the intermediate levels created by defects is the signal degradation. Indeed electron-hole pairs produced by particle interactions can fill those traps for time intervals longer than the signal collection time.
The total trapping probability is described by Equation 1.11, in which τ_{eff} is the effective trapping time and β is the trapping time constant (time, temperature and type of incident particle dependent).

$$\frac{1}{\tau_{eff}} = \beta(t, T) \cdot \Phi_{eq} \tag{1.11}$$

Trapping acts effectively reducing the free mean path of the charges: the longer the drift space, the higher the chance of being trapped. So the smaller the distance between the electrodes, the smaller the probability of traps formation [12]. Another effect is the increase of the leakage current as a consequence of the population of the energy levels induced by defects.

1.2.5 3D sensors

3D sensors were first proposed by Sherwood Parker and collaborators in 1997.
Unlikely planar sensors, with 3D technology the electrodes of both doping type are penetrating partially or entirely through a high-resistivity silicon substrate, perpendicularly to the wafer surface. As a consequence the electric field is parallel to the wafer surface, starting from one electrode type going to the another. The intensity of the electric field can be chosen by properly adjusting the voltage bias. Various connection layers made of polysilicon or metal can be used to join some electrodes, in order to create pixels, strips and pads with the same electrodes layout.
There are many advantages in exploiting the 3D configuration over the planar one [12]:

1. *Full depletion voltage*: in 3D sensors the depletion zone grows laterally between electrodes, whose distance L can be made smaller then the substrate thickness Δ (Figure 1.16, b). On the other hand, for planar sensor the voltage of full depletion is strictly linked to Δ, since the depletion region grows vertically (Figure 1.16, a). So the full depletion voltage can be reduced in the case of 3D sensors.

2. *Charge collection efficiency* (CCE): when a minimum ionizing particle traverses the Silicon sensor, it generates a uniform track of $e^- h^+$ pairs. The total charge produced depends on the thickness of the substrate and it is of the order of $76e^-$ per micron traversed. Considering 3D sensors, the charge collection distance is much shorter with respect to the planar configuration (Figure 1.16). Moreover high electric field and carrier velocity saturation can be obtained with low bias voltages. This implies that 3D sensors have much smaller collection time (with a standard 300 μm thickness, the collection time is of few ns for 3D, 10 ns for planar). Moreover, in planar sensors one obtains signals broader in time since each charge carrier is generated at different distances from the electrodes; this fact is attenuated in 3D sensors. Charges produced by the MIP ionization have much shorter distance from the electrodes, inducing fast signals.
   This fact not only allows to exploit this kind of detector for timing application, but also reduces the phenomena of charge carriers trapping in the bulk, making 3D pixel sensors more robust to bulk damage.

3. *Electric field shape*: thanks to the radial geometry of the electric field around the electrodes, it is observed an effect of self-shielding which implies, above all, a reduction of the charge sharing between nearby cells. Moreover, 3D sensors are not really sensible to magnetic fields, which is an important property given the large usage of magnet at LHC. 3D sensors have higher focal properties than planar sensors, as can be seen in Figure 1.17.

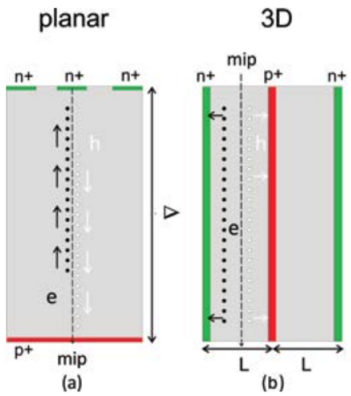

Figure 1.16: Schematic cross section of (a) planar sensors and (b) 3D sensors.

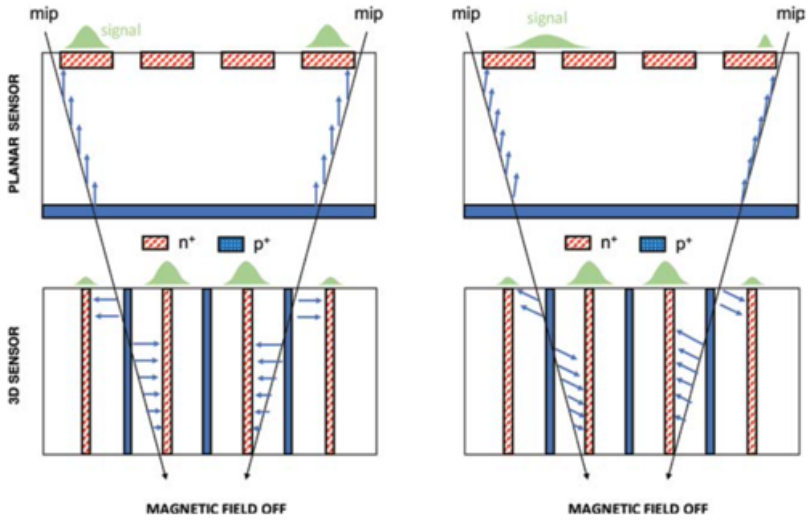

Figure 1.17: Effect of magnetic field in 3D (bottom) and planar (top) sensors.

There are also some disadvantages in 3D technologies. Depending on the chosen electrodes geometry, the electric field could not be homogeneous inside the junction, implying a delay of the overall signal response and possibly a decrease of the charge collection efficiency [12]. In addition, the small inter-electrode spacing and the electrodes extension inside the substrate cause a high sensor capacitance, that could degrade the signal rise time.

1.3 The TIMESPOT project

The TIME and SPace real-time Operating Tracker (TIMESPOT) is an INFN funded project that now is becoming a collaboration inside the Italian LHCb group. Its aim is to develop a complete tracking demonstrator capable of copying with the extremely high instantaneous luminosities foreseen in experiments at future facilities [13].
Ten INFN sections are involved (Bologna, Cagliari, Genova, Ferrara, Firenze, Milano, Padova, Perugia, Torino, TIFPA) with 65 people among physicists and engineers.

The demonstrator is supposed to comprehend a complete tracking chain, including pixel sensors, front end electronics, data acquisition system and fast pre-processing algorithms [13].

The project is divided in 6 work-packages: silicon sensors with 3D technology, diamond sensors with 3D technology, front-end electronics for pixel readout with timing using 28 nm CMOS technology, fast-tracking algorithms and devices, high speed read out boards, system integration and tests.
The Padova section collaborates for the development and characterization of silicon sensors with 3D technology.

The 3D sensors are a viable technology for the VELO Upgrade II, since they can provide good performances both regarding time and space precision measurements, alongside a great radiation hardness.

Figure 1.18: The Timespot collaboration logo.

As previously mentioned, the main goal of the TIMESPOT project is to develop and implement a complete integrated system for tracking having very high precision both in space and in time by means of innovative pixels with size 55 μm and a time resolution better than 100 ps. Within this project, Silicon 3D sensors have been developed: they should be optimized for timing measurements keeping low the depletion voltage and still ensuring good radiation damage (due to short inter-electrodes distance). The potential of 3D sensors has already been exploited: this kind of technology currently make up 25% of the ATLAS Insertable B-Layer (IBL) [14]. ATLAS 3D sensors are built with columnar electrodes not optimized for timing, thus they are only used for space-tracking.

In order to justify the design of the TIMESPOT sensors it is better to clarify the terms which contribute to the time resolution σ_t of a silicon detector when measuring the time of arrival of a high energy charged particle.
The expression can be summarized with Equation 1.12.

$$\sigma_t = \sqrt{\sigma_{tw}^2 + \sigma_{dr}^2 + \sigma_{un}^2 + \sigma_{ej}^2 + \sigma_{TDC}^2} \tag{1.12}$$

- σ_{tw} is the contribution relative to the jitter caused by event-by-event fluctuations of the signal amplitude;

- σ_{dr} is the contribution relative to the jitter due to delta rays: this can imply both event-by-event charge fluctuations and a modified signal shape, since they can be generated at different depths;
- σ_{un} is due to non-uniformities in the charge collecting field and carrier velocities inside the sensor sensitive area, changing the signal shape;
- σ_{ej} stands for jitter due to the analog noise of the preamplifier used to readout the sensor;
- σ_{TDC} is the jitter due to the digital resolution of the electronics used to measure the signal.

In the case of 3D sensors some of these contributions can be minimized. In particular, if the signal is triggered at a constant fraction the time-walk effect can be neglected. The delta rays contribution also can be neglected, since given the fact that in 3D sensors the charges are collected in a perpendicular direction to the track, delta rays produced at different depths have the same effect. In the case of σ_{TDC}, an adequate Time to Digital Converter (TDC) can make this term negligible.

The relevant contribution for a 3D sensor is σ_{un}, since the non-uniformity of the electric field and the carrier velocities highly affect the time resolution measurement. So to obtain a good time resolution the sensor should have a geometry as close as possible to a parallel plate capacitor, with uniform electric and weighting fields [15].
The other relevant contribution is the one relative to the analog noise of the preamplifier, σ_{ej}, which limits the sensor time resolution and scales as $\sigma_{ej} \approx \sigma_{noise}/\frac{dV}{dt}$ (Figure 1.19).

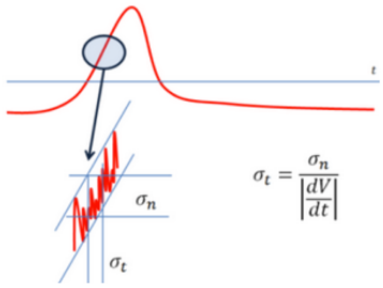

Figure 1.19: Jitter due to the analog noise of the preamplifier used to readout the sensor.

3D columnar sensor geometry was the first considered but, with this configuration, electric and weighting fields are not spatially uniform, thus resulting in a strong dependence of the position within a pixel, limiting the timing resolution. For this reason, the best choice was to switch to 3D trenched-electrode pixel sensors.

1.3.1 3D trenched-electrode sensors

3D trenched-electrode sensors consist of long p-type (ohmic) trenched electrodes along the entire length of the sensor separated by lines of segmented n-type (junction) trenched electrodes for readout. The active layer is a high-resistivity, p-type Float Zone silicon wafer of 150 μm thickness, directly bonded on top of a low-resistivity, p-type support wafer of 500 μm thickness. The p^+ electrodes pass through the active layer and reach the highly doped support wafer, so that the bias voltage can be applied from the backside. The support wafer can be thinned and covered with a metal layer. The n^+ electrodes are isolated one from each other at the front surface by means of a p-spray layer and the electrodes of both kinds are filled with doped poly-Si [16]. Concerning the p-spray layer, its peak concentration is located close to the oxide/silicon interface and must reach a value able to avoid the formation of an inversion layer of electrons underneath the oxide. A schematic layout and cross section of these sensors are displayed in Figure 1.20 and 1.21.
This configuration produces uniform electric and weighting fields and thus allows for the pulse rise

time to be largely independent of hit position. This can be observed in Figure 1.22, where the TCAD simulated electric field maps for different sensors geometry are displayed.

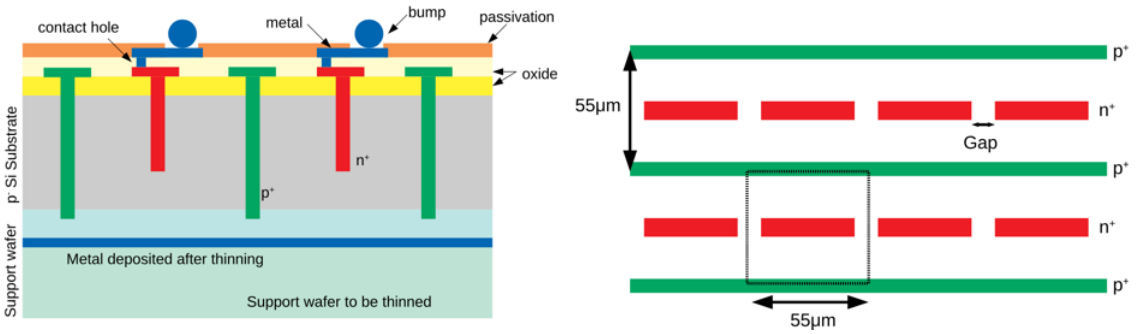

Figure 1.20: Schematic layout and cross section of the 3D trenched-electrodes sensors.

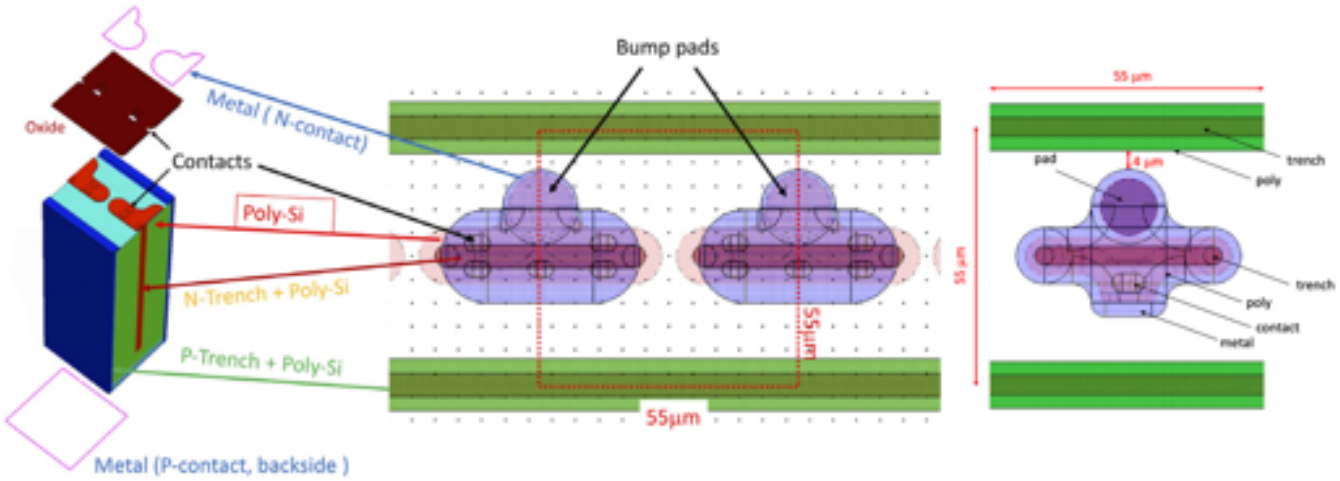

Figure 1.21: Schematic layout of the 3D trenched-electrodes sensors.

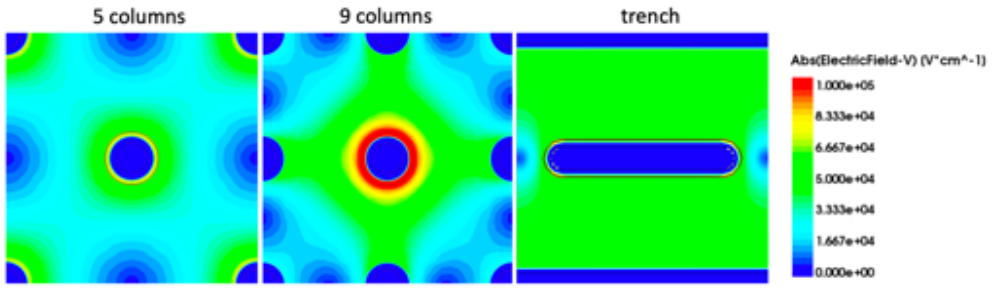

Figure 1.22: Simulated electric field maps for different sensors geometry.

Compared to columnar electrodes, this kind of sensors shows higher capacitance and an increased dead volume of the sensitive area. The former problem can be solved by considering a dedicated front-end chip, the latter by using multiple planes of sensors with an offset [14].
Moreover trenched electrodes can be straightforward adapted to strips, even though accurate studies are needed in order to find the best value for the gap between the n^+ doped trenches: making it small would improve the uniformity of the weighting field but would also increase the inter-pixel capacitance [14].

Several TCAD simulations were performed before the production of the sensors, considering some fixed design parameters such as the active thickness (150 μm) and the pixel size (55x55 μm^2) [16].

First of all simulations of electric and weighting fields were performed. As previously commented, the electric field is more uniform in between the two electrodes if compared to the columnar geometry (Figure 1.22), and the main non-uniformities appear in the gap between n^+ doped trenches.
Also the distribution of the weighting field was studied considering an array of 3×3 pixels (Figure 1.23), with 1 V bias applied to the central electrode and leaving all the others grounded. It is possible to see that the p-type trenches act as a perfect insulator [16].

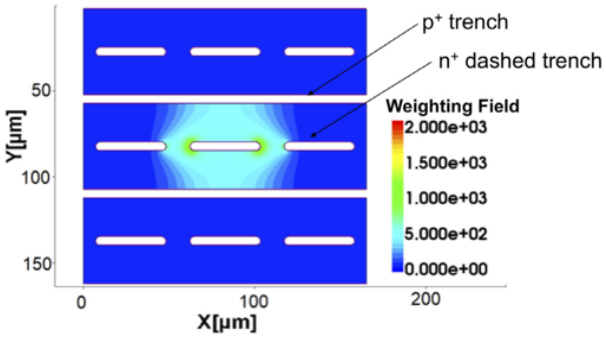

Figure 1.23: Distribution of the weighting field (V/cm) in an array of 3×3 different pixels.

3D trenched-electrodes sensors are also expected to be more radiation hard with respect to the columnar ones, due to the small inter-electrode distance and the uniform electric field. The charge collection efficiency (CCE) before and after irradiation was simulated: the 2D maps of the CCE were created starting from considerations about the Ramo's theorem and to account for bulk radiation damage the 3-level "new Perugia" trap model for p-type silicon was used [16]. In Figure 1.24 the CCE 2D maps are displayed after irradiation with fluences $5 \cdot 10^{15} n_{eq}$ cm^{-2}, $1 \cdot 10^{16} n_{eq}$ cm^{-2}, $2 \cdot 10^{16} n_{eq}$ cm^{-2}. In the first case it is possible to notice that a CCE of 80% is obtained almost everywhere in the sensitive zone between the electrodes, and with increasing fluence the CCE only slightly decreases due to charge sharing effects and due to hole trapping [16].

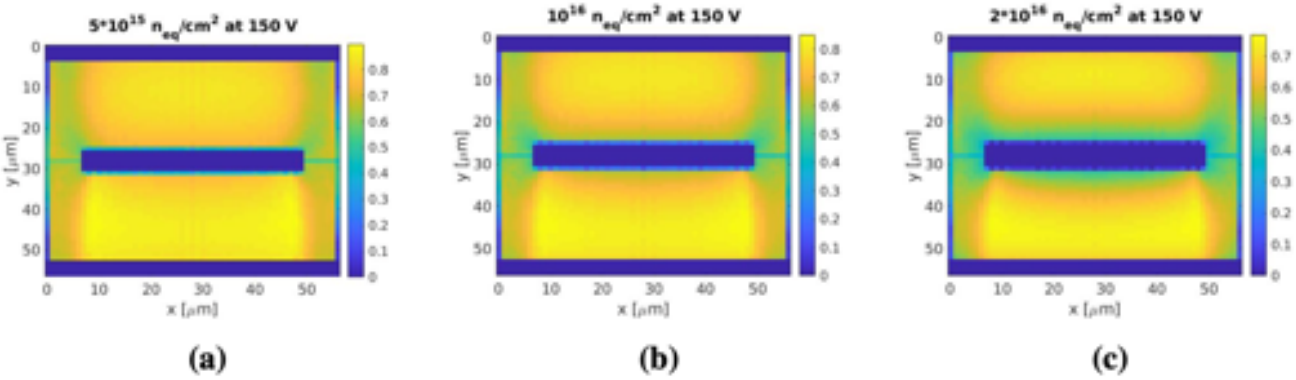

Figure 1.24: Charge collection efficiency in function of position at 100V inverse bias voltage in a 3D trenched-electrode pixel of 55x55 μm^2 irradiated at: (a) $5 \cdot 10^{15} n_{eq}$ cm^{-2}, (b) $1 \cdot 10^{16} n_{eq}$ cm^{-2}, (c) $2 \cdot 10^{16} n_{eq}$ cm^{-2}.

To choose the best design for the sensors also capacitance simulations were considered, incorporating the passivation layers, the poly-Si and metal layers, and the surface insulating layer (p-spray). For the simulation a full 3D domain was used, corresponding to the red square in Figure 1.21, including two adjacent half pixels. In this way it was possible to account for both backplane and interpixel capacitance.
Simulations were performed considering different gaps in between the n^+ electrodes and also different surface geometries (Figure 1.25). The simulated capacitance-voltage characteristics are displayed in Figure 1.26.
As it is possible to notice, the simulated capacitance is only slightly affected by the change on the

surface geometries (1.26, left). On the other hand, as expected the inter-pixel capacitance is strongly affected by the chosen gap between the trenches, meanwhile the backplane contribution is not sensitive to the gap dimension (1.26, right). In particular, backplane capacitance has a sudden decrease in the first few voltages of bias due to the lateral depletion, then slowly decreases due to the depletion of the p-spray layer on the surface area [16].
In order to obtain the total pixel capacitance from Figures 1.26, the two contributions should be multiplied by two since only half pixel is simulated. So at -100 V bias the capacitance goes from approximately 110 fF (14 μm gap) to 160 fF (6 μm gap). Since the timing performance is strictly linked to the sensor capacitance, for the production a gap of 15 μm was considered, implying a capacitance of about 105 fF and a risetime of 50 ps.

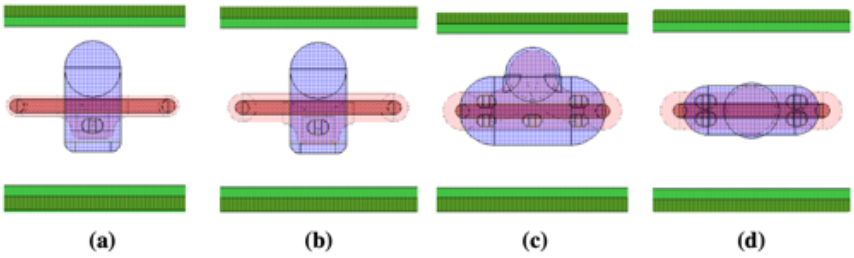

Figure 1.25: Pixel geometries used for capacitance simulations and fabrication tests [16].

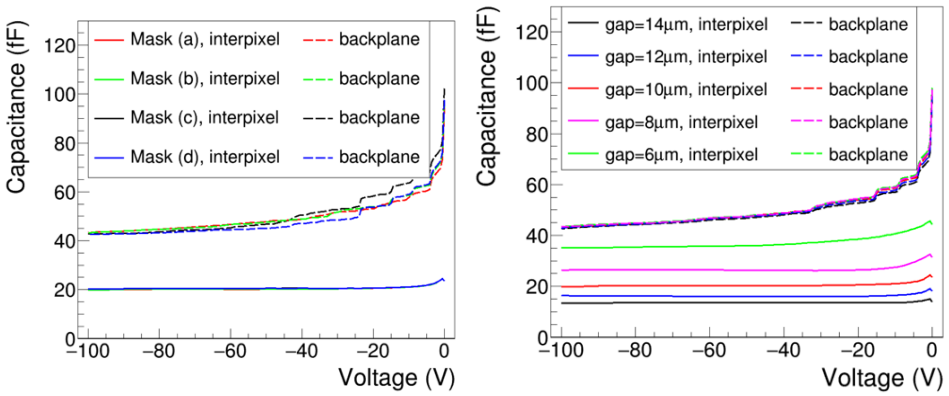

Figure 1.26: Capacitance of the four different geometries investigated with a gap of 10 μm (left) and capacitance considering different gaps in between n^+ electrodes (right) [16].

1.3.2 Sensor production

Within the TIMESPOT collaboration different kind of devices have been produced, namely strips, pixels and a pixel matrix that will be bump-bonded to the customized electronics produced by the collaboration. For my thesis work I focused on strip and pixel devices.
The sensors were produced at the Fondazione Bruno Kessler (FBK) using a single-sided fabrication process. Two batches have been produced so far, one in 2019 (batch 1) and the other in 2021 (batch 2). Batch 1 sensors have been produced by error without the p-spray deposition on the surface area and with a limited number of available geometries; batch 2 sensors have the p-spray layer and there are many more test structures with different characteristics. The presence of the p-spray layer will have consequences both regarding the capacitance trend as function of the bias voltage and on the breakdown voltage, as it will be deepened in Section 2.1.

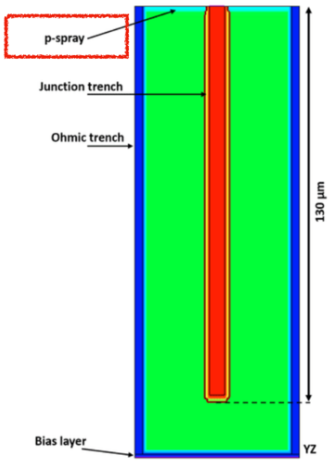

Figure 1.27: Cross section of a 3D-trenched sensor unit cell, pointing out the position of the p-spray layer.

Chapter 2

Static Characterization

2.1 Strip sensors

Strip sensor devices are composed by 10 fundamental 3D trench sensor units of 55x55 μm^2. The ten n^+ electrodes are shortcut by means of metal tracks to form a strip 550 μm long. Each device consists of 7 strips, connected to 5 metal pads to extract the signal (two pairs of them are connected to the same pad, see Figure 2.1 (left)). In the following, I will use the pad numbering shown in Figure 2.1 (right): pads A and E collect the signals from double strips, pads B, C, D from single strips.
Each device is identified by a reference number (e.g. 453 and 402 in Figure 2.1), composed as follows: the first two digits represent the length in micrometers of the n^+ doped trenches, the third digit is a code which stands for the geometry of the metal contact above the n^+ trenches. There are mainly three kinds of metal contacts, which are referred to as 1, 2, 3 (Figure 2.2). The first two have only one electric contact with the n^+ doped trench and a layer of poli-Silicon with length 1 and 2 μm out of the trench. The third one has five electric contacts and a larger layer of poli-Si.

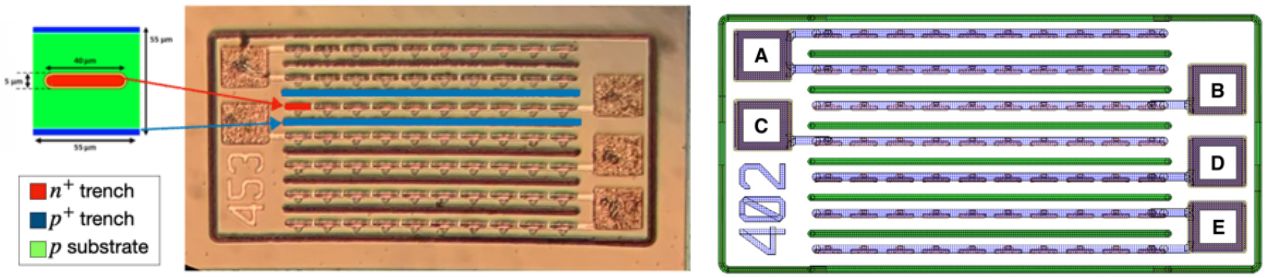

Figure 2.1: Layout of the strip devices and reference nomenclature for the single metal pads.

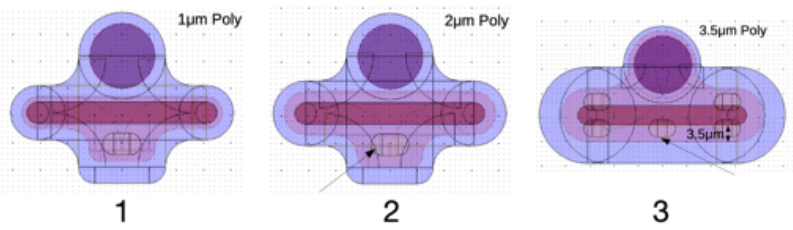

Figure 2.2: Different geometry of the metallic contacts.

Many strip devices have been produced with different combination of length of n^+ trenches and metal contact geometries in order to find the best sensor layout possible.
These strips have been tested performing both current-voltage characteristics and capacitance-voltage

characteristics; also studies with devices under X-rays irradiation have been performed.
These points will be treated in the following sections.

2.1.1 I-V characteristics

The current-voltage (I-V) characteristics study is relevant in order to extrapolate the breakdown voltage of the silicon devices, but also to investigate defects in the sensors which could lead to high leakage current and to establish the current that the bias voltage supply should deliver.
The I-V measurements have been performed by means of an HP 4142B Modular DC Source/Monitor, which allows high performance DC parametric measurements. It is equipped with four Source Monitor Units (SMUs) which can deliver respectively $\pm 100V$ and $\pm 200V$. The instrument is connected to the probe station by triaxial cables; the probe station is composed by a metal box containing a microscope, a 4" chuck and micro-manipulated needles. The metal box is needed both for safety reasons, since the voltage can be delivered only if the cage is closed thanks to a switch, and to test the device in dark conditions, to minimize the photo-generation of electron-hole pairs. The device under test (DUT) is placed on the metal chuck. The sensor bias is provided by the chuck itself (contacting the p-type bulk) and by a probe on the metal pad on the surface of the device (contacting the n^+ readout electrode). In order to reverse bias the sensor, negative voltage should be applied to the plate of the probe station, meanwhile the metal pads should be grounded. Both the chuck and the probe are connected by triaxial cables to a dedicated SMU.

For the I-V characteristics measurements the n^+ electrodes were fixed to ground and the p^+ electrodes voltage varied from 0 V down to -200 V or less depending on the value of their breakdown voltage. The I-V measurement was performed reading the current value of the probe connected to the n^+ electrode. A dedicated software could perform automatically the I-V characteristics of a certain strip. It allowed to choose the maximum bias voltage value and the number of voltage steps. Given that the expected leakage current values are small, for each voltage step it was chosen to average on 100 consecutive measurements.
In order to estimate the uncertainties on current measurements, several sets of 1000 repetitive measurements were taken considering different bias voltages: looking at their standard deviations, a reasonable estimation is ± 2 pA.
In Figure 2.3 the I-V characteristics for the strip device number 392 from batch 1 (left) and batch 2 (right) are displayed. The presence of the p-spray layer in batch 2 devices has two main consequences with respect to batch 1 ones:

- the leakage current is two order of magnitude smaller, since the presence of the p-spray layer implies that n^+ electrodes are well isolated;

- breakdown voltages are smaller in absolute value: the p-spray layer induces locally high electric field which implies an early breakdown, which appears to be around -70 V in the case of batch 2 devices, compared to the -200 V of batch 1 ones.

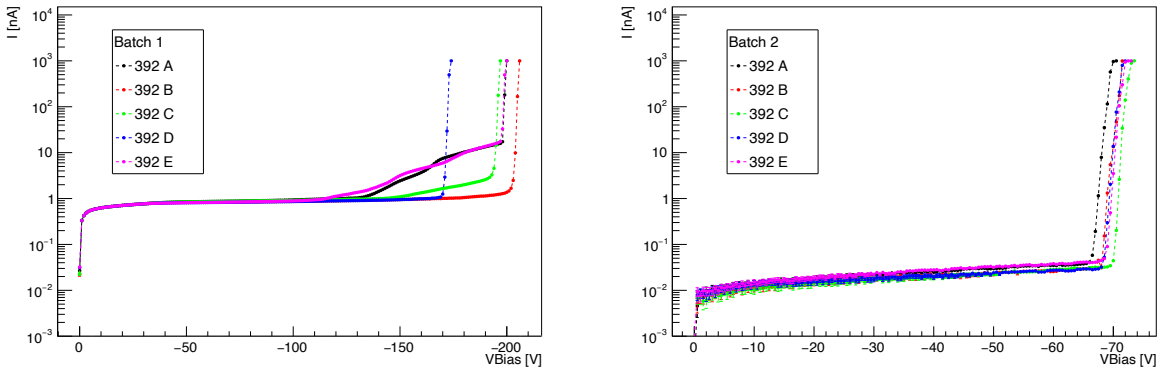

Figure 2.3: I-V characteristics of strip device 392 from batch 1 (left) and batch 2 (right).

These features are common to all the strip devices from batch 2, into which my thesis work has been focused. The I-V characteristics of all the strip devices from batch 2 I tested are reported in the Appendix.

It is clear that the presence of p-spray has important consequences on the breakdown voltage value, due to the fact that the highly-doped n^+ regions are directly in contact with the medium-dose p-spray. Simulation on the effect of the presence of p-spray in n^+-on-p microstrips have been performed [17] and an induced early breakdown was observed, but still it is not clear the consequences of a possible irradiation of the Silicon device. In fact the irradiation causes an increase of the effective substrate dopant concentration [17] implying a decrease of the breakdown voltage, but also the increase of the oxide charge with the particle fluence, which has the opposite effect. The prevailing effect can be established only by considering the type of device and the irradiation conditions.

2.1.2 Effect of X-ray irradiation

To investigate the effect of ionizing irradiation on 3D-trenched sensors, the device in Figure 2.4 was irradiated with an X-ray source with energy spectrum peaked at 10 keV. The irradiation was performed in steps (100 krad, 200 krad, 500 krad, 1 Mrad, 1.5 Mrad) and after each one the respective I-V characteristics were recorded for each of the five metal pads of the four devices.

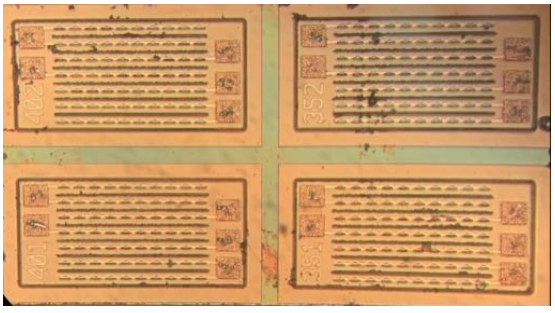

Figure 2.4: Wafer containing the four strip devices irradiated with X-rays.

In Figure 2.5 the I-V characteristic of strip A from device number 351 are displayed. It is possible to notice that after subsequent irradiations the breakdown voltage increases in absolute value, which means that the positive charges created in the oxide by the irradiation are able to partially compensate the negative charges present in the p-spray. Another effect is the increase of the leakage current: this is due to the contribution of surface currents produced by the electrons released from the Silicon Dioxide.

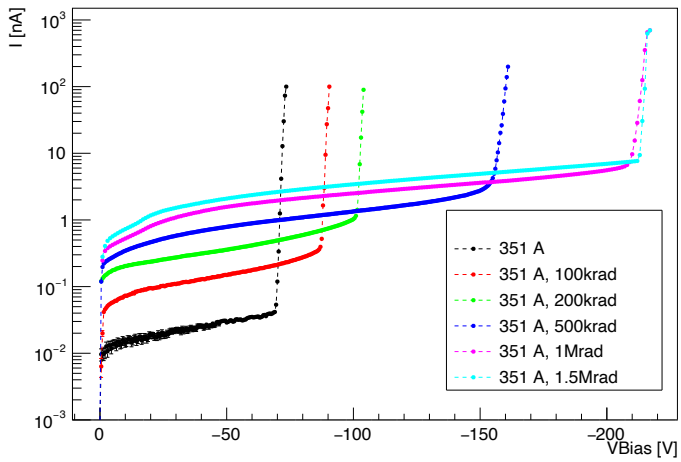

Figure 2.5: I-V characteristic of strip A from device number 351 after subsequent steps of irradiation.

Figure 2.6 displays the value of the breakdown voltage and the leakage current as function of the dose absorbed by the device, obtained respectively with a linear fit in the breakdown region and as a fit with a constant of the current before the breakdown. Uncertainties on the parameters deriving from the fit are too small to be visualized in the plot.
The breakdown voltage decreases linearly with dose, until the positive charges in the oxide fully compensate the negative ones on the p-spray after a dose of 1 Mrad.

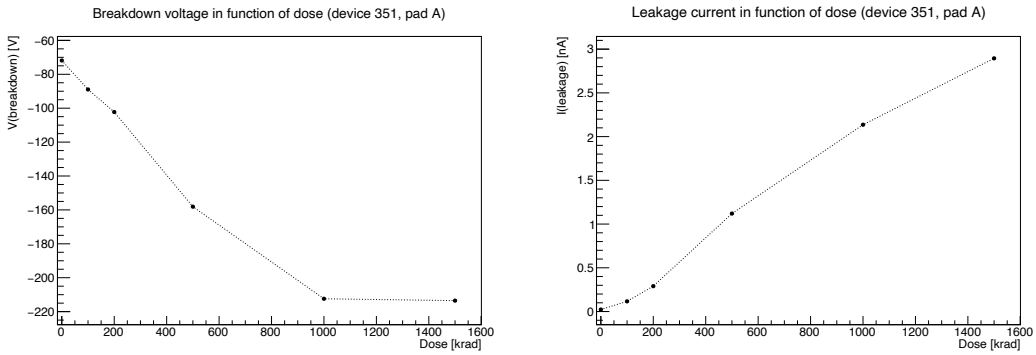

Figure 2.6: Trend of breakdown voltage and leakage current as a function of the dose absorbed by the device.

Given that several strip devices from batch 2 have been tested, it was possible to make comparisons between different metal contact geometries and different n^+ trenches lengths.
Figure 2.7 shows the I-V characteristic comparison between strip devices with metal contact geometry number 2 (left) and 3 (right) for several n^+ trenches length for the double strip E. In the case of surface geometry number 2, the different lengths of the n^+ trenches has no consequences on breakdown voltage and leakage current. On the other hand, for surface geometry number 3 the case in which n^+ trenches are 35 and 40 μm long show higher breakdown voltages, in the order of -120 V.

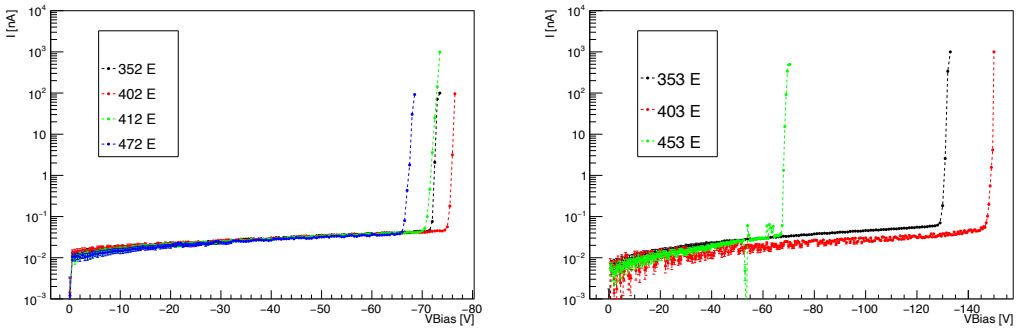

Figure 2.7: I-V characteristic comparison between strip devices from batch 2 with metal contact geometry number 2 (left) and 3 (right) for several n^+ trenches length for the double strip E.

It is possible to better understand the effect of the chosen metal contact geometry looking at Figure 2.8, which displays the comparison between the I-V characteristics of strip devices with n-doped trenches 35 μm long but different metal contact geometry. It is reported also the geometry number 5, which is equal to geometry number 2 but the metal tracks do not pass above the n-doped trenches, but beside them. So as far as one considers strips with n^+ electrodes shorter than 40 μm, the best layout choice is the one with surface geometry number 3 since it shows the highest breakdown voltage.

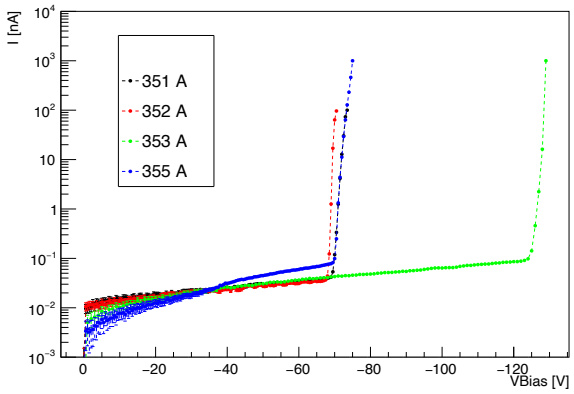

Figure 2.8: I-V characteristic comparison between strip devices with length of the n-doped trenches equal to 35 μm but different metal contact geometry.

2.1.3 C-V characteristics

The Capacitance-voltage (C-V) characteristics study is significant to extrapolate the bias voltage at which the silicon sensor is fully depleted.
The C-V measurements were performed using a HP 4284A PRECISION LCR METER and the HP 4142B Modular DC Source/Monitor. The HP 4284A PRECISION LCR METER is an instrument that outputs a sinusoidal voltage signal to the circuit one wants to investigate. Signal amplitude and frequency can be set by the user. Considering the distortion of the output signal, the instrument measures two components of the complex impedance (parameters) at the same time in a measurement cycle. According to the model that the user chooses before starting the measurements, the instrument provides the physical quantity one is interested in.
In this particular case, it was chosen the model C_P-D, which provides the measured capacitance and the dissipation factor.
The instrument is really precise and accurate: it was tested with a well known capacitance of 4.7 pF directly connected to the output terminals of the instrument itself and it showed an uncertainty of the order of tenths of femtoFarads. It was then performed a test with the same capacitance but with

long cables connecting it to the instrument (to better simulate a realistic setup) and this induced an error of the order of 70 fF: the setup highly influences the measurements. Moreover, considering that the measurements of the capacitance of 3D sensors is much more complex than the measurement of a classical one, also the model could influence the result. To summarize all these contributions, an uncertainty of ± 100 fF was assumed for the C-V characteristics measurements.

As for the measurement that were performed with the 3D sensors, the bias voltage was provided by means of a SMU coming from the HP 4142B directly connected to the HP 4284A. The "high" pole of the latter instrument was connected to the cable leading inside the probe station to the probe station chuck, giving the bias from the backside, the "low" pole was connected to the probe needle contacting the metal pad on the device surface.
The sinusoidal voltage signal was chosen of amplitude 10 mV and frequency 10 kHz. By means of a dedicated software, it was possible to perform automatically the C-V measurements of a certain strip, allowing to choose the voltage range, the number of voltage steps inside the interval and the number of measurements to average to get the final capacitance value. The chosen range was $[0; -60]$ V and in this case the average was not taken since the HP 4284A instrument already perform the integration of several signals before giving the final result.

The result of the recorded C-V characteristics of strip device number 392 from batch 1 (left) and batch 2 (right) are displayed in Figure 2.9.

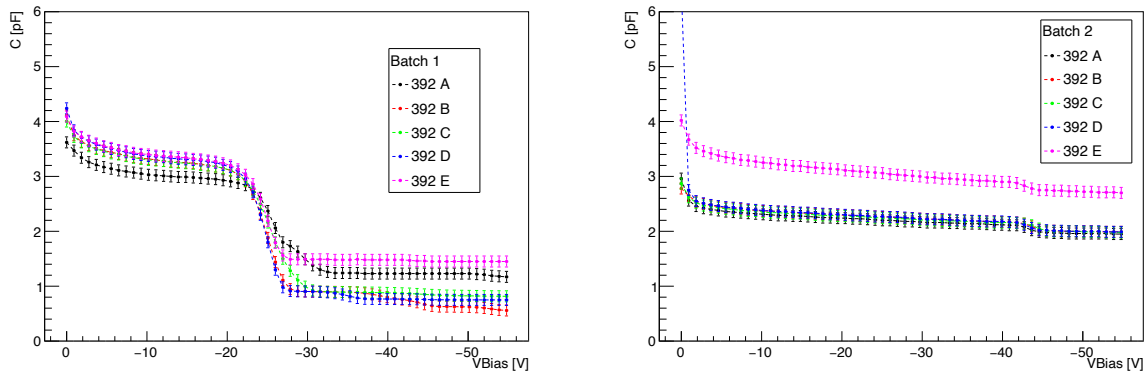

Figure 2.9: C-V characteristics of strip device 392 from batch 1 (left) and batch 2 (right).

In the case of the device from batch 1, there is a sudden depletion around $V_{bias} = -25$ V that is due to complex MOS effects. In the case of batch 2 sensor, the C-V characteristics is more regular, showing a small step around $V_{bias} = -45V$ that can be interpreted as the depletion of the junction induced by the presence of the p-spray layer. Moreover, in this case it is possible to see that the strip connected to the pad E has higher capacitance with respect to the others: this is expected since the pad E is connected to two strips (Figure 2.1, right). The same behaviour was expected also for pad A for the same reason, but, as it will be seen also in the following, the technology behind these devices has still some issues; the most probable hypothesis is that only one of the two strips was actually electrically connected to the pad A.

The C-V characteristics of all the strip devices from batch 2 I tested are reported in the Appendix.

2.1.4 Inter-strip resistance

To complete the study of strip devices, an inter-strip resistance measurement was performed. To do so, the HP 4142B Modular DC Source/Monitor was used in combination with three needle probes inside the probe station, following the scheme in Figure 2.10 as an example. The chuck was put at -10 V, the central strip (in Figure 2.10 the strip relative to pad B) was put at a variable voltage in the interval

$[-0.5; 0.5]$ V by means of a SMU and the lateral ones (in Figure 2.10 the strips relative to pad A and C) were grounded also by two other independent SMUs.

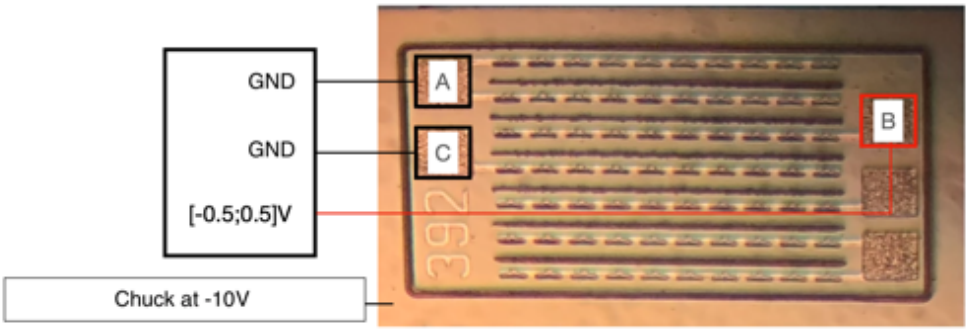

Figure 2.10: Layout for the inter-strip resistance measurement.

The current is measured in each of the three probes and the results are reported in Figure 2.11 for the resistance between the strips B, C, D from strip device number 392 from both batches. As expected, the current measured by the probe of the central strip is equally distributed in between the lateral ones.
In Figure 2.11, left, it is possible to see that the I-V characteristics for the strips from batch 1 follows the Ohm's law and the resistance is of the order of tens of MOhms.
In Figure 2.11, right, it is displayed the current flowing in the strips in the case of batch 2 devices, which are well isolated due to the presence of the p-spray layer. In this case the I-V characteristics is not symmetrical. Given the high electric isolation of the strips, it is likely that the current we are measuring is not the one going from one electrode to the other, but it is coming from the substrate. Anyway in this case the inter-strip resistance is 1000 times higher than in the case of batch 1.

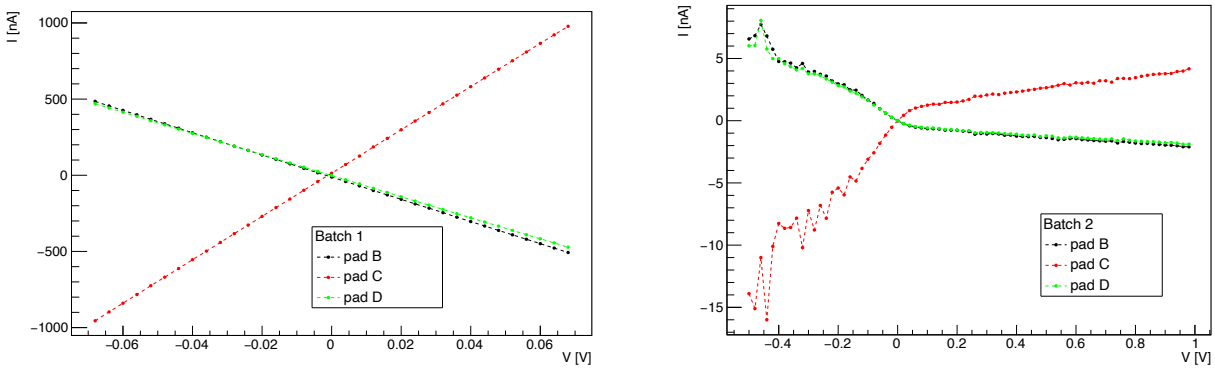

Figure 2.11: Current flowing in strips B,C,D from device number 392 in the case of batch 1 (left) and batch 2 (right).

In the Appendix the Figures relative to all the possible combinations of inter-strip resistance are displayed.

2.2 Pixel sensors

Pixel sensor devices are composed by single and double fundamental 3D trench sensor units of 55x55 μm^2. Two kinds of device were produced within the batch 2, depending on the shape of the ohmic p^+ trenches. The layout and reference nomenclature to the metal pads are displayed in Figure 2.12. In the following, I will refer to Figure 2.12, left, as the "vert" version of the device, to Figure 2.12, right, as the standard version.

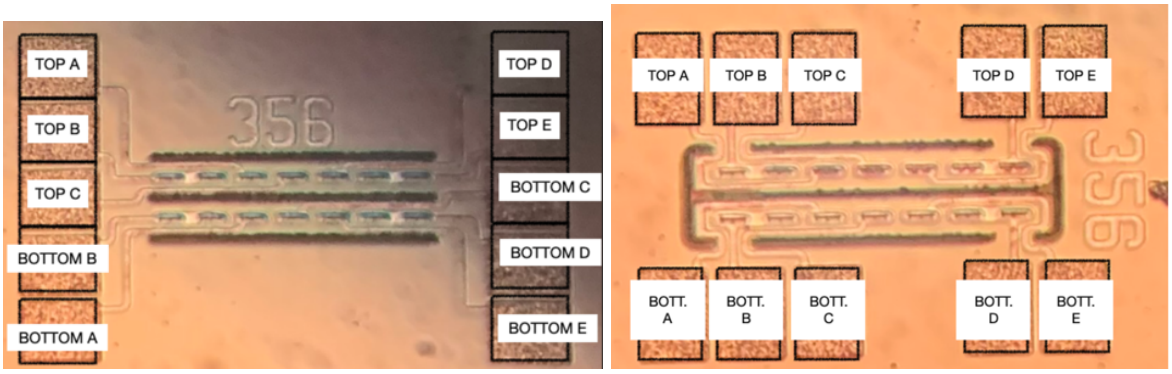

Figure 2.12: Layout and reference nomenclature for pixel devices from batch 2.

Metal pads B and D are connected to two pixels, meanwhile C, D, E are connected to single ones.

The number identifying the single device is coded in a similar way of the strip devices: the first two digits represent the length in micrometers of the n^+-doped trenches, the third digit stands for the geometry of the metal contact. In the case of pixel devices, it was available only the version with surface geometry number 6, which is equivalent to the number 3 for strip devices (Figure 2.2).

The pixel devices have been tested performing both current-voltage characteristics and capacitance-voltage characteristics, as it will be shown in the following sections.

2.2.1 I-V and C-V characteristics

I-V characteristics were recorded in the same way of strip devices, by means of the probe station combined to the HP 4142B Modular DC Source/Monitor.
Many of the pixel devices available were not electrically connected to the respective metal pads due to issues during the production process. Moreover, very often it was not possible to complete all the desired measurements since the device got damaged in the meantime.
The results collected for the pixel device number 356 in the vert versions are reported in Figure 2.13. It is possible to notice that, in general, pixel devices show breakdown voltages above $V_{bias} = -100$ V, so they are in general more resistant than strip devices.

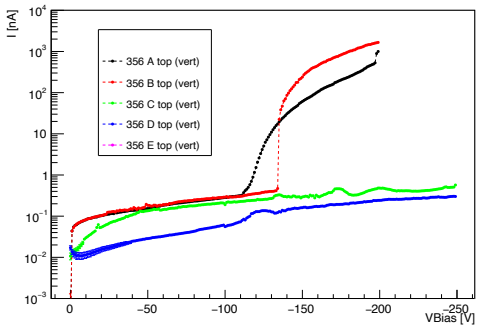

Figure 2.13: I-V characteristics of pixel device number 356 in vert version.

An example of the C-V characteristics of the pixel devices is displayed in Figure 2.14 for the device number 406. As it is possible to notice, it has the same features of the strip devices C-V characterization, showing the step due to the p-spray layer around $V_{bias} = -50V$, even though the absolute value of the capacitance is lower as expected.

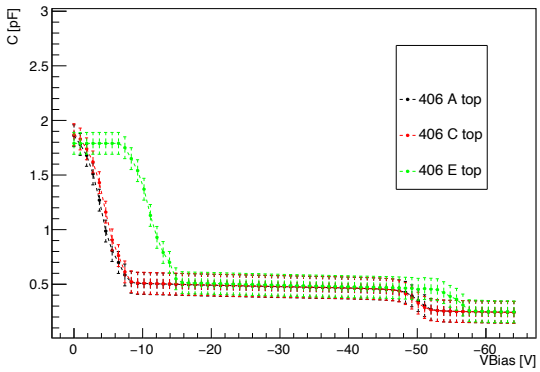

Figure 2.14: C-V characteristics of pixel device number 406 from batch 2.

2.2.2 Inter-pixel capacitance

Inter-pixel capacitance is a relevant parameter to understand how neighboring pixels share charges. To evaluate it, the setup scheme reported in Figure 2.15 was considered: two probes linked the external single pixels (pad A, E) of device number 406 to the high pole of the HP 4284A, which delivers a sinusoidal voltage signal with amplitude 10 mV, the third probe linked the central pixel (pad C) to the low pole.
The resulting capacitance measurement is the parallel of the two inter-pixel capacitance between pixels A and C, C and E.

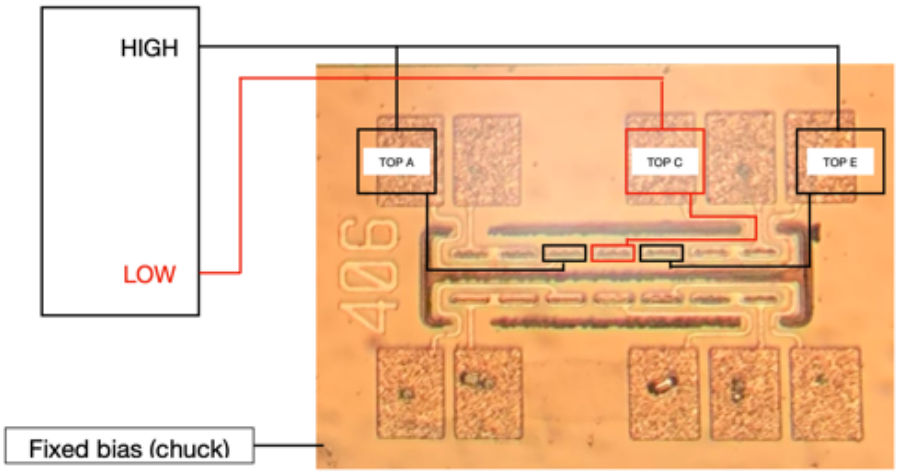

Figure 2.15: Setup used to perform the inter-pixel capacitance measurements.

Chosen a fixed bias voltage, a set of 100 capacitance measurements was recorded. The mean is reported in Figure 2.16. As it is possible to see, the inter-pixel capacitance value is lower than 100 fF and as previously stated the instrument combined with the probe station setup implies that the measurements can be considered precise only if the capacitance is of the order of picoFarads. For this reason, in Figure 2.16 the uncertainties are not reported since they are of the same order of magnitude of the result itself; the plot as to be intended as a qualitative indication.

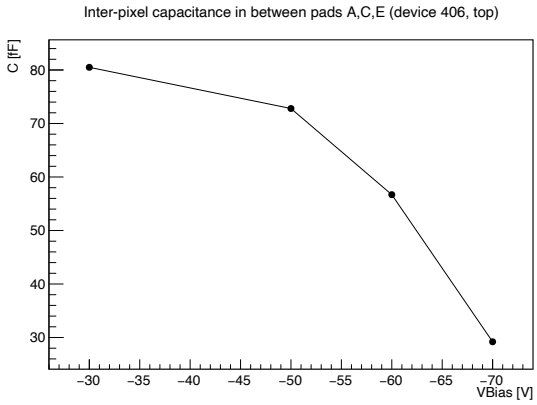

Figure 2.16: Inter-pixel capacitance measurement results for different bias voltage values.

We can conclude that the inter-pixel capacitance of this kind of pixel devices is of order of 100 fF or less, since the setup allows only to reach this level of precision.

2.2.3 Comparison between simulated and measured pixel capacitance

When the sensor substrate is fully depleted, its capacitance value stop to vary as function of the bias voltage, since equilibrium has been reached and there is no more charge migration. It is possible to see this effect in Figure 2.14 for the case of pixel device number 406 when $V_{bias} < -55$ V.

Let's take as an example the pad C of pixel device number 406, connected to a single pixel. The final capacitance of this sensor when fully depleted is 240 pF (Figure 2.14), to be compared to the 100 pF expected from TCAD simulations (Figure 1.26). To account for this excess, in the calculation also the contribution coming from the neighboring pixels (pad A and pad E) should be included. So, on a first approximation, when the C-V of a certain single pixel is recorded by polarizing it, also the floating nearby pixels contribute, according to the simplified scheme reported in Figure 2.17, left, and the relative equivalent circuit in Figure 2.17, right.

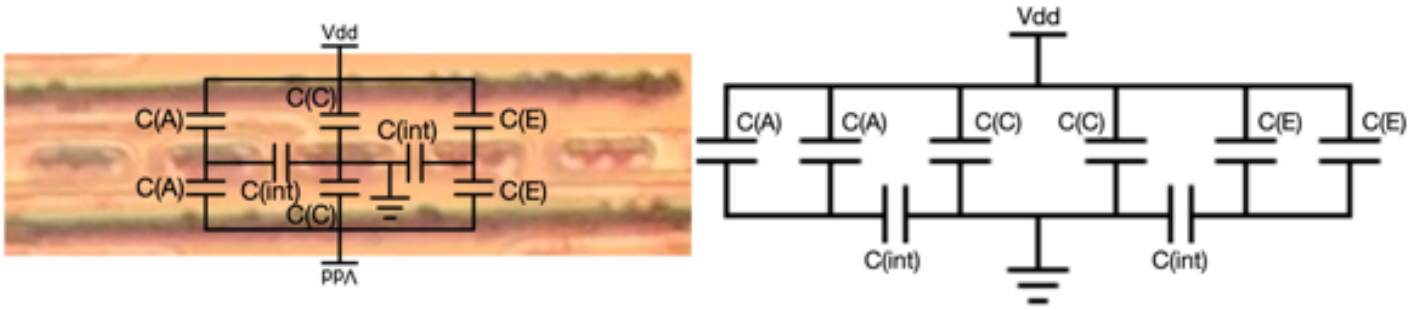

Figure 2.17: Schematic layout of capacitance contributions when recording a C-V on a pixel device.

Within this simplified model, it has been assumed that the inter-pixel capacitance is equal for the two pixel pairs and that the capacitance contributions coming from the two sides of the n^+ electrodes are the same.
Fixing $V_{bias} = -60$ V, for pixel device number 406 it has been measured the capacitance composed by the parallel of the capacitance contributions coming from the two sides of the n^+ electrodes for pad A, C, E (that is $C'(A) = C(A) \parallel C(A)$, $C'(C) = C(C) \parallel C(C)$, $C'(E) = C(E) \parallel C(E)$ with reference to Figure 2.17).

C-V characteristics have been performed only biasing the pixel of interest and leaving the neighboring ones floating. In order to get a capacitance measurement closer to the real one for the central pixel (pad C), another C-V characteristic was recorded, this time connecting the nearby pixels readout

electrodes to ground. This results in a smaller parasitic contribution to the central pixel capacitance measurement, which, at $V_{bias} = -60$ V, turns out to be about 200 pF (to be compared to the previous value of 240 pF).

When a C-V measurement is performed, what it is recorded is not only the value of $C'(C)$, but the capacitance with all the contributions reported in Equation 2.1, where the S symbols means that the two capacitance are in series.

$$C'(C)^{mis} = (C'(A)\ S\ C(int)) \parallel C'(C) \parallel (C'(E)\ S\ C(int)) \tag{2.1}$$

Finally the value for the single pixel capacitance relative to pad C can be expressed as in Equation 2.2.

$$C'(C) = C'(C)^{mis} - C(int) \cdot \left(\frac{C'(A)}{C'(A) + C(int)} + \frac{C'(E)}{C'(E) + C(int)} \right) \tag{2.2}$$

So considering $C'(C)^{mis} \approx 200$ fF, $C'(A) \approx 240$ fF, $C'(E) \approx 240$ fF and $C(int) \approx 60$ fF, $C'(C)$ results about 150 fF. Within the uncertainties of the instrument, the result can be considered compatible with the one from simulations, meaning that the physical contributions to the capacitance measurements are quite understood.

Chapter 3

Dynamic Characterization

A second important goal of this work is to characterize the signals produced by the 3D devices in order to estimate the time resolution and the uniformity of the response across the sensor active area. To do so, a dedicated setup was designed and built with the final goal of performing a test beam at the AN2000 accelerator in Legnaro. The AN2000 is a Van de Graaff electrostatic-type accelerator: protons or helium beams are used to probe the samples and detailed measurements for the elemental composition analysis of any material can be performed, by bombarding samples and identifying, through appropriate detection techniques, the particles or radiation which are produced in the beam interaction with material. The AN2000 is endowed also with the "microbeam line" which can provide an ions pencil beam, having just a few micrometer transverse size.

The purpose of the test beam is to irradiate a strip device with protons of 2 MeV energy: thanks to the microbeam facility it is possible to know the hit position of the proton with a precision of 1 μm, allowing to relate the signals to a certain area of the strip. A 2 MeV proton is expected to penetrate the silicon device for ≈ 40 μm before loosing all its energy.
The idea of the physical mechanism considered to perform the time resolution measurement on the Timespot devices is the following. First, a layer of ≈ 10 μm of P-terphenyil [18], an organic scintillator, is deposited right above the strip to be investigated. Then a Silicon Photo-Multiplier (SiPM) is placed facing the strip. With this configuration, before the proton hits the strip, it ionizes the scintillator layer, which emits photons to be revealed by the SiPM.
It should be noted that the signals induced by 2 MeV protons are roughly 35 times bigger than those produced by Minimum Ionizing charged Particles (MIP) ($dE/dx(Si) = 1.67$ MeV/g/cm^2 [1]) therefore time resolution and pulse height distributions for MIP have to be extrapolated accordingly.

In the next Sections the components of the experimental setup will be explained in detail, followed by the results obtained in the test beam.

3.1 Experimental setup

A schematic drawing of the experimental setup is shown in Figure 3.1 and 3.2.

[1] Particle Data Group 2018, figure 33.8

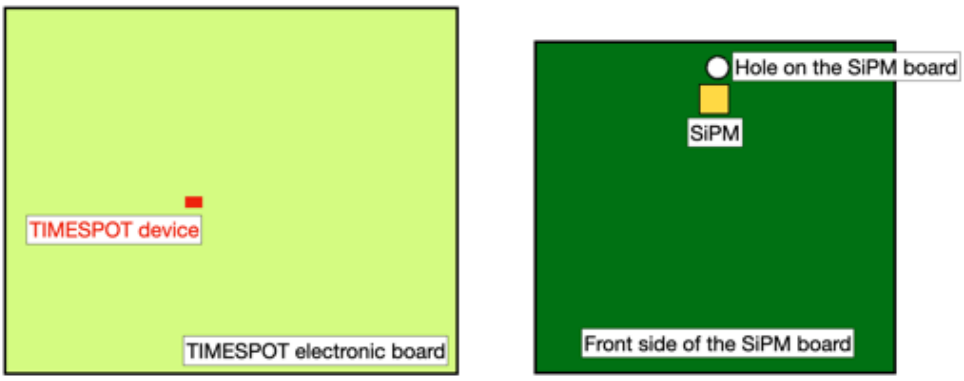

Figure 3.1: The TIMESPOT electronic board with the silicon device (left) and the SiPM with its electronic board (right).

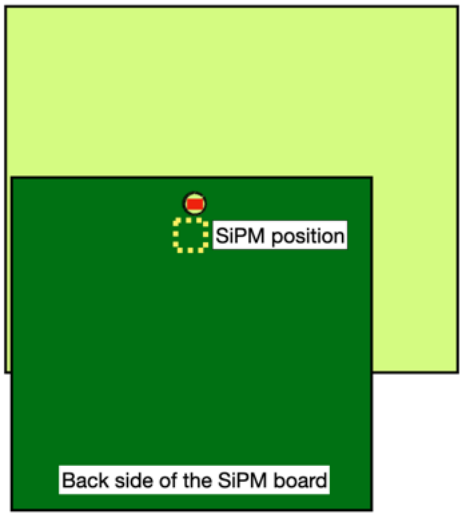

Figure 3.2: Disposition of the TIMESPOT and SiPM electronic board for the test beam, with the SiPM facing the strip device and the hole aligned with the strip device.

In Figure 3.1, left, there is the schematic layout of the TIMESPOT electronic board with the strip device in red; it will be described in detail in Section 3.1.1.
In Figure 3.1, right, there is the scheme of the Silicon Photo Multiplier (SiPM) electronic board, with the SiPM position in yellow and the hole in the upper part. It will be described in Section 3.1.2.
Finally in Figure 3.2 there is the layout of the full setup, with the hole on the SiPM board aligned with the TIMESPOT strip device and the SiPM facing the strip. A more detailed explanation is reported in Section 3.1.3.

3.1.1 Timespot Strip device

The 3D pixel strip device was mounted onto a custom front end board (FEE) developed by the Cagliari INFN group specifically for these devices. The FEE uses a SiGe transimpedence amplifier for very fast signal response and the sensor was mounted very close to the input stage to minimize noise. For this characterization, a strip device with codification number 351 from batch 1 was chosen: in particular, the single strip related to pad C (with reference to Figure 2.1) was tested. The sensor, located in the middle, is polarized through the backside and through a wire-bonding which connects the metal pad on the surface of the device to the tracks of the front-end board. The bias voltage was delivered by means of a Keithley 6487 Picoammeter/Voltage source, which allowed both to deliver the desired voltage to the sensor and to monitor the current flowing in it.

Figure 3.3: Electronic board for thee Timespot sensors designed in Cagliari.

3.1.1.1 Characterization of the pixel strip test detector

Due to the short time between the delivery of the sample and the scheduled beam time, a full I-V and C-V characterization of the strip of interest was not possible. Nevertheless a quick I-V characteristics was recorded by means of the Keithley with the sensor already mounted on the electronic board. The result is shown in Figure 3.4. This characteristics was used as a qualitative reference to verify the status of the device. The details of the I-V curve are affected by the rest of the electronics mounted on the front end board. It is possible to notice that when positive bias voltages are applied, the strip is polarized forward and the current has a rapid increase.
The uncertainties from the Keithley 6487 Picoammeter/Voltage source on current measurements are of tens of pA and uncertainties on the voltage set are of the order of mV, thus it is not possible to observe them in Figure 3.4.

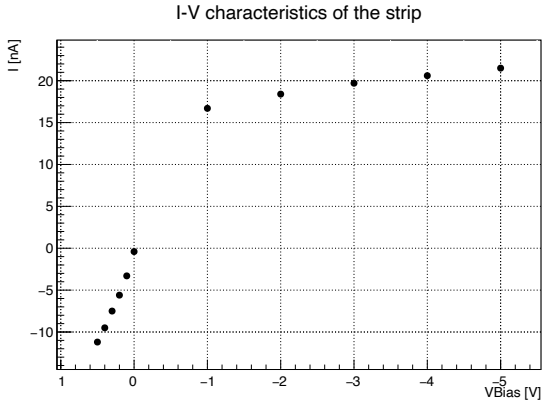

Figure 3.4: I-V characteristics of the strip recorded by means of the Keithley, measuring directly from the electronic board.

A penetrating infrared laser (1060 nm) was used to verify the response of the device. The rise time of the laser pulse was too slow for timing purposes therefore, in order to study the time resolution and risetime, a blue laser with 40 ps pulse width and sub-picosecond stability was used. The blue laser pulse penetrates only partially in the silicon bulk simulating the proton signal.
To collect the signal induced by the blue laser in the strip, a Tektronix MSO64 oscilloscope was used. One channel of the oscilloscope was linked to the trigger exit of the laser, the another one was connected with the exit of the electronic board from which comes the strip output signal. The electronic board was put in a metal box, in order to reduce the photo-generation of electron-hole pairs.
Pointing the blue laser on the strip with its highest intensity generated a signal with pulse height from 12 mV to 30 mV, depending on the chosen bias voltage, comparable to the proton expected signal.
The time resolution is extracted from the root mean square of the time difference between the laser

trigger signal and the 3D pixel strip signal at 20% threshold. The resolution was computed for various values of the 3D pixel strip bias voltage in order to optimize the working point. The results are displayed in Figure 3.5, left. It is possible to notice that there is a sudden improvement in time resolution after $V_{bias} = -15$ V, going from approximately 30 ps to 13 ps. This trend is similar to the one of the C-V characteristics of batch 1 strip devices as it is possible to see in Figure 3.5, where it is reported the C-V characteristics of strip device number 392 as the one relative to device number 351 was not recorded. In this particular case the drop in capacitance happens at a different bias voltage, but probably the different geometries of these devices implies also the appearance of this step at different voltages.
The capacitance of the sensor is strictly linked to its timing performances, the higher the capacitance the worst the time resolution.
So the Timespot 3D sensors are demonstrated to be capable of time resolutions of the order of ten picoseconds if the applied bias voltage is high enough.

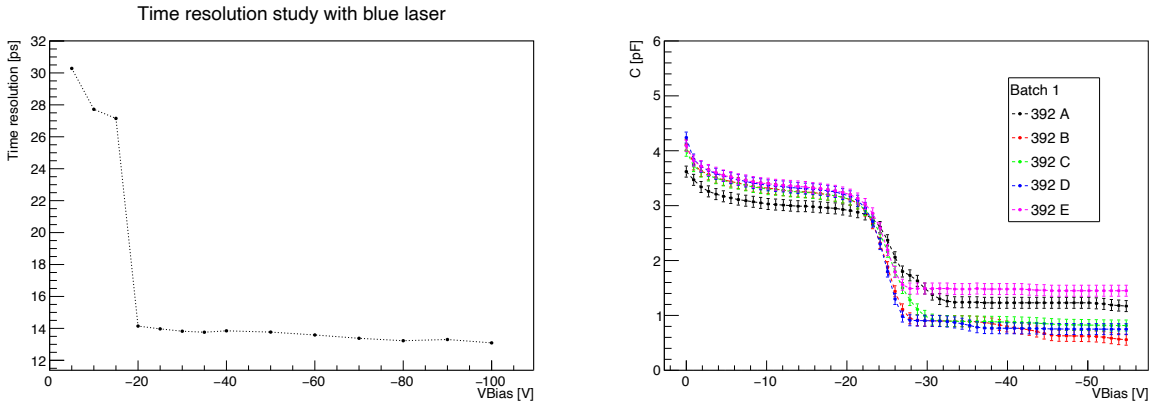

Figure 3.5: Time resolution of the Timespot strip with respect to the fast blue laser as a function of different bias voltages (left) and the C-V characteristics of strip device number 392 from batch 1 (right).

Then setting the trigger on the strip signal, keeping the laser pointed to the sensor, a signal risetime analysis was performed for different bias voltages. The risetime was extrapolated as the mean of the histogram automatically filled by the oscilloscope by means of the function "risetime", which calculates it considering the times relative to the 20% and 80% of the maximum of the signal.
The result is displayed in Figure 3.6. One can observe that as the bias voltage increases in absolute value, the risetime becomes shorter. The customized FEE for the test beam was optimized for giving fast responses since the goal of the analysis is the estimation of a time resolution of order of tens of picoseconds. The design of the FEE implies that only a signal with risetime shorter than a certain threshold is correctly amplified and passed to the output terminal; signals with lower risetimes are filtered out by the capacitance present in the circuit board. The amplitude of the signal is proportional to its speed, so a fast signal will have a great height, a slow signal will be characterized by a very small amplitude.

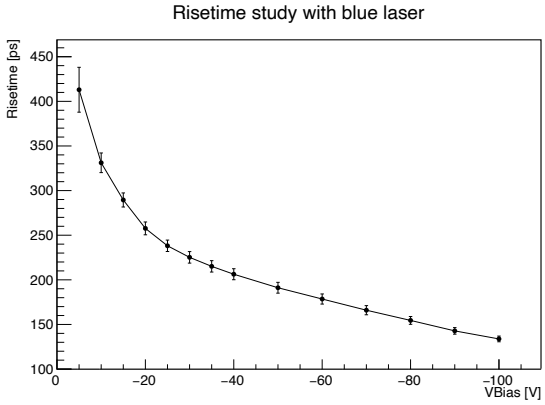

Figure 3.6: Risetime of the strip signal induced by the blue laser for different bias voltages.

Considering the lowest bias voltage applied in absolute value, $V_{bias} = -5$ V, it was measured a pulse height of approximately 12 mV, a risetime around 400 ps and a signal noise of order of 1 mV. Meanwhile if one considers the highest bias voltage applied in absolute value, $V_{bias} = -100$ V, it was measured a pulse height of approximately 30 mV, a risetime around 150 ps and a signal noise of order of 2 mV. Given this quantities, it is possible to estimate the expected time resolution of the strip by means of the following equation:

$$\sigma_t = \tau_{rise} \cdot \frac{\sigma_{noise}}{A}$$

where τ_{rise} stands for the risetime, σ_{noise} is the root mean square of the noise distribution in mV and A is the pulse height. So considering the quantities related to the two limit cases of bias voltages applied, -5 V and -100 V, one obtains a time resolution in the interval [10;30] ps.

3.1.2 Silicon Photo-Multiplier

A Silicon Photomultiplier is a dense array of small, independent, in parallel Single Photon Avalanche Diode (SPAD) sensors, each with its own quenching resistor. The SPAD sensors are photodiodes operated in Geiger mode [19]. This means that in the depletion region there is a very intense electric field (induced by the design of the device and by an appropriate bias voltage), so when a photon crosses it generating electron-hole pairs the charge carriers created are accelerated to a point that they are able to create secondary charge pairs through impact ionization. This fact implies an avalanche generation of the electron-hole pairs resulting in the flow on an electric current limited by the series electrical resistance. The overall process can be summarized as the amplification of the original electron-hole pair. The growing current is then stopped by means of passive quenching through a series of resistors, which limits the current flowing in the device restoring the SiPM to Geiger mode.
The need of having an array of SPAD sensors comes from the fact that the single unit gives the same signal if is hit by one or more photons: to have information about the flux, it is necessary to have more cells ready to detect each a photon at the same time. Each microcell detects photons identically and independently, and the final signal is the combination of all these photocurrents [19].
The equivalent circuit of an array of SPADs that compose a SensL SiPM with fast output is displayed in Figure 3.7, left. It can be used for simulation purposes, in order to study the static and dynamic behaviour of the SiPM. In Figure 3.7, right, a typical spectrum of the photoelectrons of the SiPM can be seen.

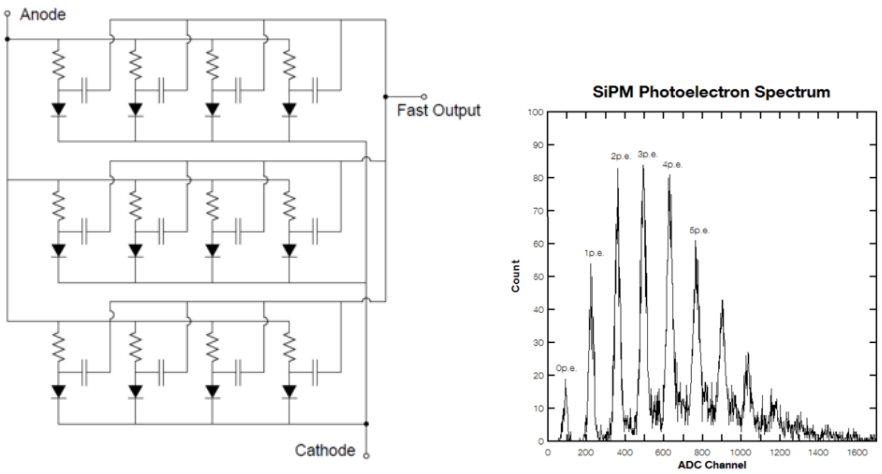

Figure 3.7: Schematic electronic layout of a SiPM (left) and typical voltage spectrum of SiPM signals (right) [19].

The SiPM fast output terminal allows to carry an ultra-fast output signal. As it can be seen in the equivalent circuit in Figure 3.7, left, each microcell has a capacitively coupled output, so that the fast output signal is the derivative of the internal fast switching of the microcell in response to the detection of a single photon [19]. The shape of the signals coming from the fast output depends on both the quench resistors and the capacitance of the single cell. A typical signal shape for a 6 mm SiPM is shown in Figure 3.8. This kind of signals coming from the fast output terminal can be used to make ultra-fast timing measurements, so they are suitable for the goal of the test beam.

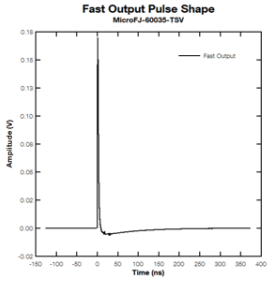

Figure 3.8: Fast output pulse from a 6 mm SiPM [19].

The SiPM considered for the test beam is a 3x3 mm^2 SensL (model: MICROFC-SMA-30035-GEVB); a photo of the device is reported in Figure 3.9. The bias voltage is given from the below exit, then there are other two exits for the output, of which it was taken the fast one (the one on the left of the electronic board). The SiPM fast output terminal was then connected to a Mini-Circuit amplifier (model TB-409-5+), which needed to be powered with 8 V.

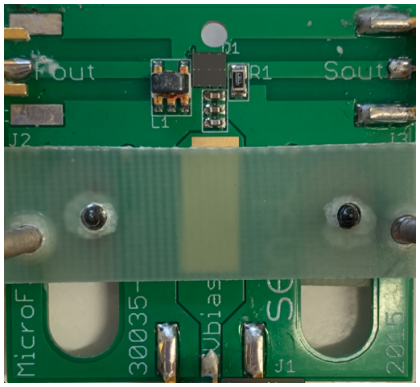

Figure 3.9: Silicon Photo-multiplier with its electronic board.

3.1.2.1 SiPM characterization

In order to find the suitable bias voltage, the SiPM was characterized by means of the Tektronix MSO64 oscilloscope in the following way. The SiPM with the amplifier connected was placed inside a light tight metallic box in order to avoid natural light hitting hit. The output of the amplifier was then connected to the oscilloscope. Given the dark conditions, the characterization of the SiPM was performed delivering a certain bias voltage and observing in the oscilloscope the signals produced by the thermally generated electron-hole pairs, producing the avalanche. The oscilloscope automatically displayed in an histogram the peak of the SiPM voltage signals, and waiting for a certain amount of time to have enough statistics it was possible to observe the photoelectron spectrum of the SiPM, similar to the one in Figure 3.7, right. The difference of the voltages relative to different peaks is the definition of gain of the SiPM and it was estimated from the pulse height distribution recorded with the oscilloscope. The gain as a function of the chosen bias voltage is displayed in Figure 3.10.

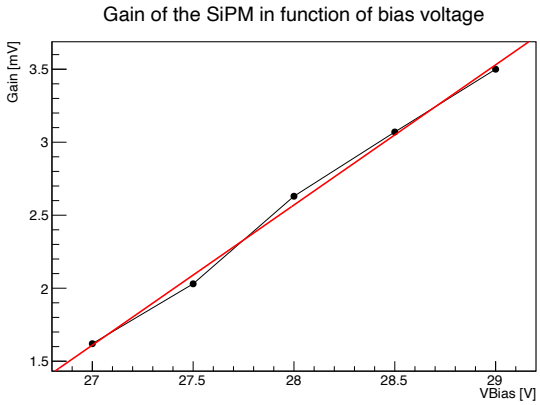

Figure 3.10: SiPM gain in function of the chosen bias voltage.

Performing a linear fit of the data, it was possible to extrapolate the breakdown voltage of the SiPM as the intercept; the result is $V_{br}^{SiPM} = 25 \pm 1$ V.
For the test beam it was chosen to operate the SiPM at a bias voltage of 28.5 V, with an expected gain of approximately 3 mV/photon.

3.1.3 Full setup

To perform the time resolution measurements, the Timespot device with its electronic board and the SiPM with its amplifier where combined together. To better clarify the assembly, in Figure 3.11 it is reported the electronic board onto which there is the Timespot device, highlighted in red, and the semi-transparent layer of P-terphenyil, highlighted in yellow. The right side shows a zoom on the strip device, with highlighted the pad relative to the strip under test. In Figure 3.12 the electronic board of the SiPM is shown in its front side and back side.

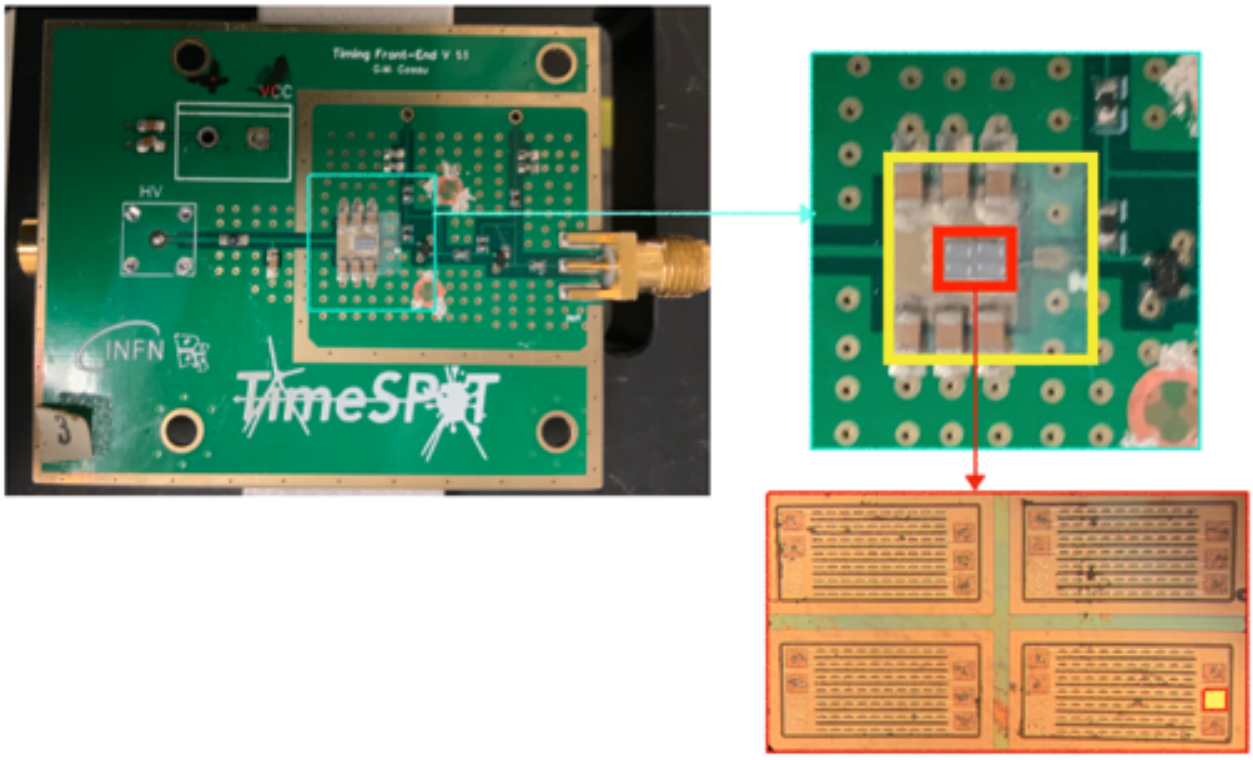

Figure 3.11: Electronic board onto which there is the Timespot device with a zoom in the sensor region: in red it is highlighted the strip device, in yellow the semi-transparent layer of P-terphenyil.

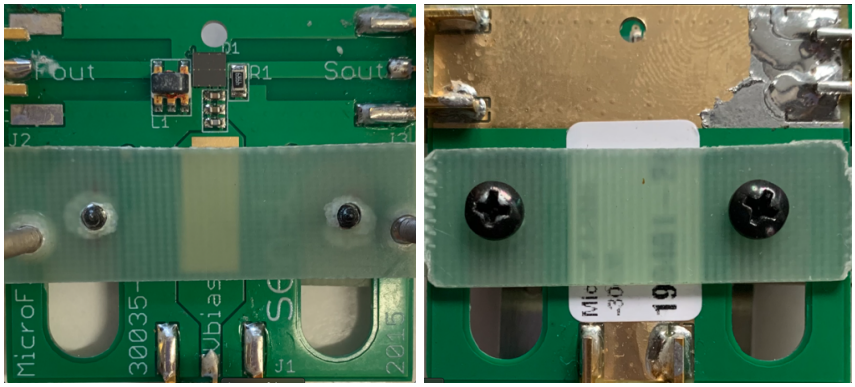

Figure 3.12: Front and back side of the SiPM board.

Finally in Figure 3.13 the full setup is displayed. The SiPM board is placed in front of the electronic board of the strip, so that the Timespot sensor is facing the SiPM and is aligned with the hole in the SiPM board (Figure 3.14). The alignment was performed by means of a microscope: the two electronic boards were placed in the microscope plate and the SiPM board was properly adjusted so that the strip was visible from the hole.
Two vetronite pieces were put over and under the SiPM board, tighten by two screws (Figure 3.12): loosening them it was possible to move the board to perform the alignment of the hole with the strip. The vetronite piece under the SiPM board is endowed with two fixed screws which link it to the Timespot electronic board and two metallic shims, so that it is possible to choose the distance between the strip and the SiPM.

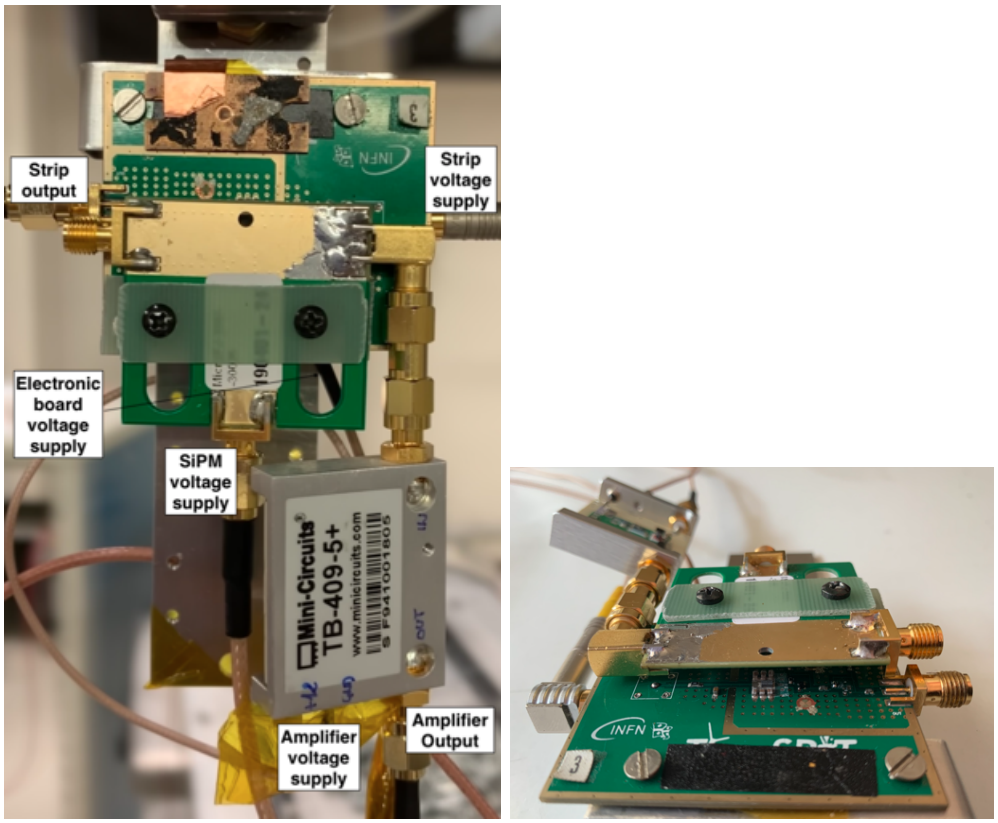

Figure 3.13: Full setup used for the test beam, seen from the front (left) and from the above (right).

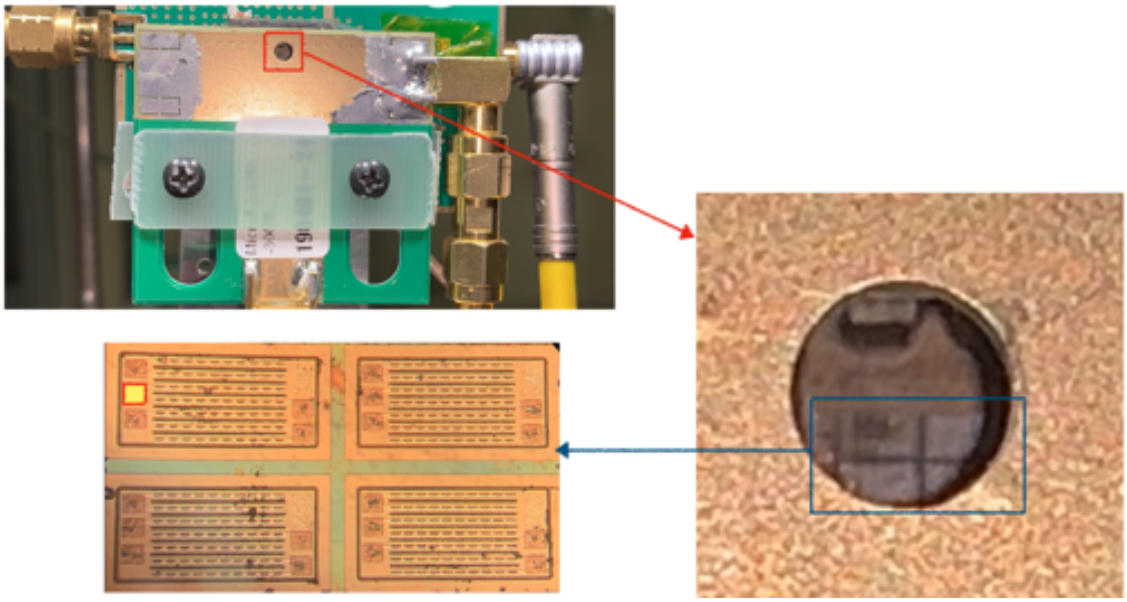

Figure 3.14: Full setup used for the test beam, with a zoom on the hole of the SiPM board which is aligned to the strip device.

3.1.3.1 Setup optimization

To find the SiPM-strip distance which maximizes the number of photons reaching the Silicon Photomultiplier, a toy model of the setup was studied. The relative positions of the SiPM and of the strip were considered as fixed and the only variable was the distance between the two electronic boards, which will be referred as the z variable.
Considering the strip as point-like, the solid angle which the SiPM covers was evaluated for different

z values.
The missing information was the expected number of photons reaching the SiPM. Given that the stopping power of protons in P-terphenyil is $S = 160$ MeV/g/cm^2 [2] and the P-terphenyil density is $\rho = 1.23$ g/cm^3, the energy that protons loose in the organic scintillator layer, which is ≈ 10 μm thick, is $E_{loss} \approx 0.197$ MeV. The P-terphenyil is expected to emit 35000/MeV [18], so every proton crossing generates approximately $n = 7000$ photons. Among these n photons, assuming that the emission is isotropic, half of them will be emitted towards the electronic board and thus will never reach the SiPM board. Another fraction of these is reflected inside the scintillator: considering its refraction index, this fraction comes out to be approximately the 40%.
Given all these considerations, every time a proton hits the P-terphenyil layer, approximately 1200 photons are emitted towards the SiPM electronic board. Finally, considering the solid angle covered by the SiPM and the efficiency of the SiPM itself, which is assumed to be $\approx 25\%$, the number of photons reaching the SiPM in function of the variable z was evaluated.
The result is displayed in Figure 3.15. The expected number of photons detected by the SiPM reaches a maximum at $z = 5mm$, so this distance was chosen for the two electronic boards.

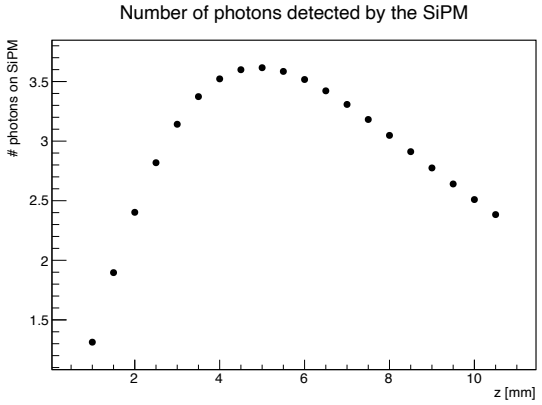

Figure 3.15: Number of photons detected by the SiPM in function of z, the distance between the two electronic boards, as predicted by the toy model.

Anyway, the number of photons expected to reach the SiPM is quite low (3/4 photons), so it was chosen to add to the SiPM electronic board a customized reflector, made of a plastic support enriched with a Copper reflective surface, so that the SiPM could cover a larger solid angle.
Since the Copper reflective surface is adhesive, after building up the reflectors they where tested by means of a vacuum pump, in order to make sure that it would not degas or change shape in vacuum conditions such as the ones that are needed for the test beam in Legnaro.
The two reflector geometries considered and their assembly in the SiPM board are displayed in Figure 3.16.

[2] `https://physics.nist.gov/cgi-bin/Star/ap_table.pl`

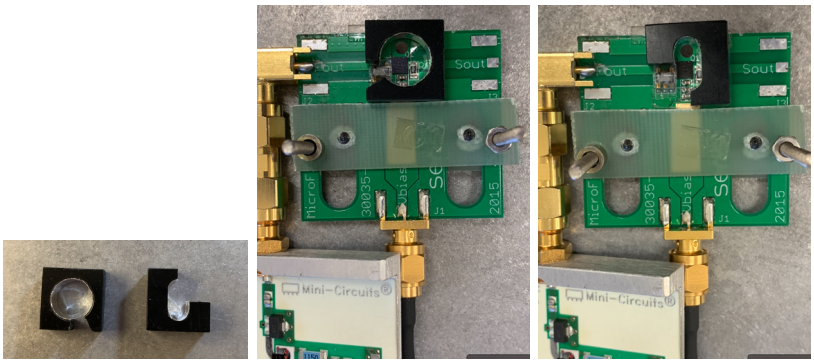

Figure 3.16: The two reflector geometries considered (left) and their assembly in the SiPM board (center and right).

To test whether the reflectors were effective or not, the fast blue laser was used. A dedicated setup was built: the SiPM board with its amplifier was placed in the light tight metallic box (in order to avoid natural light) with the blue laser positioned approximately were the strip was supposed to be. The SiPM was polarized with 28.5 V and the 8 V supply was delivered to the amplifier. The laser was put at its minimum intensity and opportunely diffused with a piece of paper in order to simulate the photons originated by the P-therephenil layer. The output signal of the SiPM was collected and visualized with the Tektronix MSO64 oscilloscope, and it was observed qualitatively that when the reflectors were added the SiPM signal had a significant increase. With this setup it was not possible to place the laser fiber in exactly the same position with and without the presence of the reflectors, so a quantitative measurement was not meaningful in this case.
For the final setup the circular reflector (Figure 3.16, center) was chosen, which allowed to approximately double the signal amplitude.

3.2 Test Beam at LNL@AN2000

As anticipated, the setup described in Section 3.1 was brought to Legnaro in order to perform a test beam using the microbeam facility at the AN2000 accelerator. The setup was mounted inside the vacuum chamber (Figure 3.17, right), the strip was polarized using the Keithley 6487 Picoammeter/-Voltage source, and the voltages needed to polarize the SiPM and to be delivered to the Timespot electronic board and to the Mini-Circuit amplifier were provided by a standard DC power supply.
The output terminals from the strip and the SiPM were connected to a Lecroy WavePro 254HD, 2.5GHz High Definition Oscilloscope (20 GS/s), which recorded the waveforms and saved it into binary files, to be converted for an offline analysis. In Figure 3.17, left, the workstation is shown.

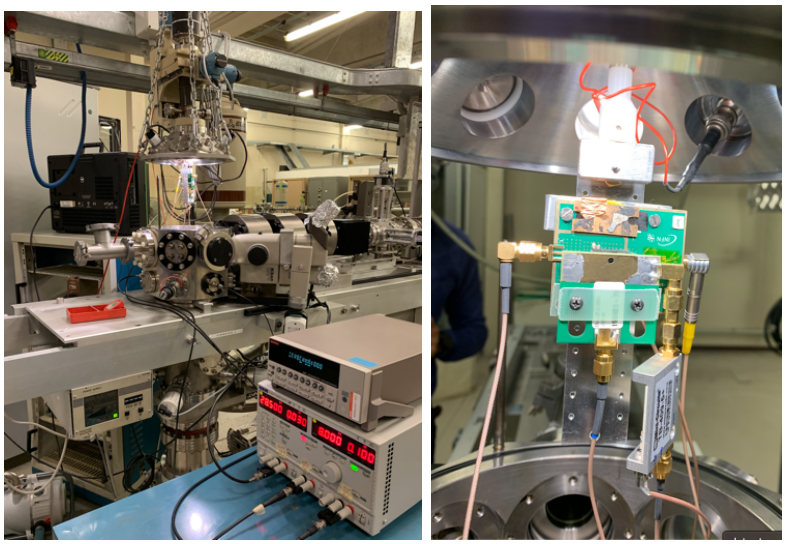

Figure 3.17: Workstation at AN2000 with the setup mounted in the vacuum chamber (right), the oscilloscope, the Keithley and the DC power supply (left).

As previously mentioned, the microbeam facility allows to know the hit position of the proton with a precision of 1 μm thanks to a rastering system: its working principle is based on electric fields which deviate the collimated proton beam coming from the accelerator. In this way it is possible to know the x,y coordinates of the proton in the vertical plane orthogonal to the beam. The x,y information is passed to the oscilloscope as well, which stores also these information for the offline analysis.

Once the vacuum was induced in the vacuum chamber with inside the setup, all the power supplies were turned on and all the lights in the accelerator room were turned off. The beam was then focused on the Timespot electronic board by means of a quartz, glued to the board, which emitted visible light when hit by the protons. The 2 MeV-proton microbeam could then be delivered. Monitoring the frequency of trigger on the strip signal waveform by means of the oscilloscope, which was controlled remotely from the control room, it was possible to adjust the dimension of the area to be scanned by the microbeam. Chosen that, several run of data acquisitions could be recorded changing the trigger conditions. Moreover also the bias voltage of the strip was changed alongside the test beam time.

3.2.1 Data analysis

The ultimate goal of the data analysis is the time resolution estimation of the strip device. To check whether the sensor is behaving as expected, the frequency of triggers and the maximum amplitude of the signals are studied, also in the case of the SiPM signals. Moreover by means of the bidimensional distribution study, the spatial distribution of the quantities just mentioned could be investigated, to check possible inhomogeneities in the behaviour of the sensor within its sensitive zone.

The data analysis was performed offline using the waveforms saved in the binary files of the Lecroy oscilloscope. A dedicated Python code[3] could convert the binary files into a ROOT file.

Several data acquisition were recorded during the test beam time, modifying both the bias voltage and the beam intensity. A summary of the most relevant ones is reported in Table 3.1.
Run 3 was collected with $V_{bias} = -100$ V and the good quality of the beam allowed to record data useful for the analysis even with a trigger level of 10 mV, which is low if one considers that the strip signal in this bias conditions were of order of 100 mV.
After Run 3 the Timespot strip was damaged due to the intense proton irradiation: high leakage currents, of order of few microAmpere, were observed flowing in the strip device by means of the

[3]Code available at `https://gitlab.com/gabriele.simi/timespot_tb_lnl/-/blob/master/lecroy_pixel-sipm.py`

Keithley and so it was necessary to lower the bias voltage. Unluckily, it is not possible to know the dose which was absorbed by the device, since the intensity of the proton beam can be known only if a dedicated dosimeter is placed inside the vacuum chamber.
Moreover after Run 3 the proton beam collimators were adjusted and the quality of the beam got worse. This fact alongside with the radiation damage induced on the strip device implied that the background signals became more persistent. As a consequence, in the case of Run 8, Run 16, Run 18 the trigger level was raised up to respectively 90 mV and 70 mV (Table 3.1).
Due to the radiation damage, a characteristic type of radiation induced strip signals were observed: they will be addressed as "trains" (see Sections 3.2.1.2 and 3.2.1.3). This kind of pulses are characterized by a significant underflow, of order of -10 mV, so a Run 10 acquisition was recorded with a negative trigger level in order to select these events.
Finally Run 11 was acquired triggering on the SiPM signal and a trigger level of -15 mV was chosen in order to select only the pulses generated by at least four photons.

	Trigger on:	Trigger level [mV]	V_{bias} [V]	Radiation damage
Run 3	strip signal	10	-100	No
Run 8	strip signal	90	-40	Yes
Run 10	strip signal	-5	-40	Yes
Run 11	SiPM signal	-15	-40	Yes
Run 16	strip signal	90	-50	Yes
Run 18	strip signal	70	-50	Yes

Table 3.1: Summary of the characteristics of the runs acquired during the test beam.

3.2.1.1 Run 3 analysis

Run 3 was acquired with the trigger at 10 mV on the strip signal waveform and a bias voltage on the strip equal to $V_{bias} = -100$ V.
A typical event recorded with the oscilloscope useful for the time resolution estimation is reported in Figure 3.18, in which the blue waveform is the one relative to the strip and the orange one is the one relative to the SiPM.

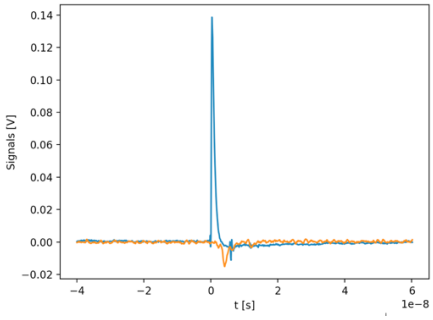

Figure 3.18: Typical event with the strip (blue) and SiPM (orange) waveforms from Run 3 data.

Pulse height analysis

As previously mentioned, the distribution in the bidimensional plane of the frequency of triggers was studied; the result is displayed in Figure 3.19. The x,y information coming from the rastering system is expressed in Volts; the conversion factor is 1 V=300 μm.

Figure 3.19 shows that the Timespot sensor works correctly: trigger events which happened more than 120 times during the acquisition time are localized in the sensitive area of the strip.
A mean of 50 events is also recorded in the strip metal pad position. This could be due to the fact that a residual electric field is generated by the potential difference between the metal pad (which is

grounded) and the back of the device, which has negative potential in order to polarize the silicon sensor. Protons are able to completely cross the metal pad reaching the substrate and producing electron-hole pairs, that menage to reach the readout electrodes thanks to the residual electric field.
Few events are recorded outside the expected sensitive region: a possible explanation is given in the following. The trigger settings ("random trigger") in the oscilloscope implied that in some cases a signal was recorded even if not satisfying the trigger conditions, so also this effect contributes to the events which do not fall in the sensitive region in Figure 3.19. Moreover some signals could be induced by X-rays emitted by the protons scattering on the edges of the metallic hole on the SiPM board. Finally some events could derive from the scattering of the protons on the beam collimators, as it will be deepened in Section 3.2.1.2.

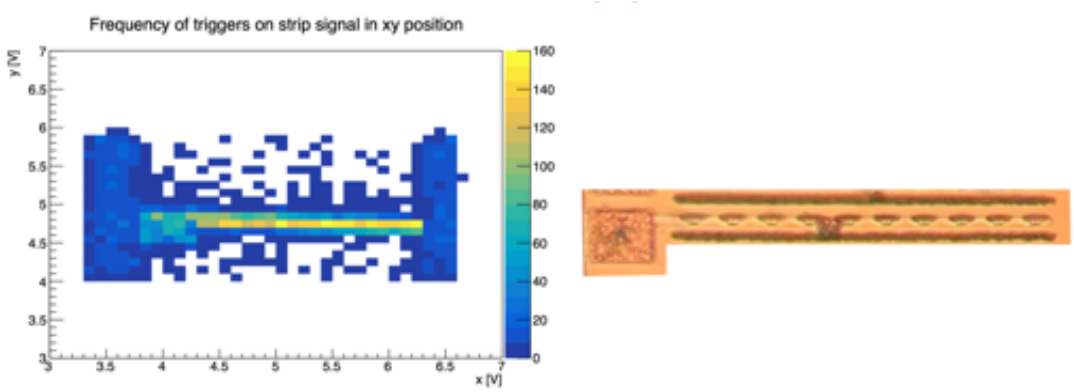

Figure 3.19: Bidimensional plot of the frequency of triggers from Run 3 ($10mV$ on the strip signal waveform, $V_{bias} = -100$ V) in a certain x,y position (conversion factor 1V=300μm).

Figure 3.20, left, shows the bidimensional plot of the maximum heights of the strip signal waveform; when a proton hits a certain position more than once, the average value is taken.
To estimate the maximum of the waveforms the first interval of the strip signal (Figure 3.18) was fitted with a constant function in order to estimate the baseline, which was then subtracted to the maximum height of the waveform. The color scale is expressed in Volts, so that the highest signals are approximately 140 mV and appear in the sensitive region of the strip. For the signals outside of it, the considerations done above still hold.
Figure 3.20, right, displays the distribution of the strip maximum height: the peak which arises close to zero is due to the events recorded with the random trigger functionality. The peak relative to approximately 20 mV arises from signals coming from the strip metal pads, as one can see from the bidimensional plot in Figure 3.20, left: the residual electric field does not allow an efficient charge collection, so the pulses originated in that area have low amplitudes.

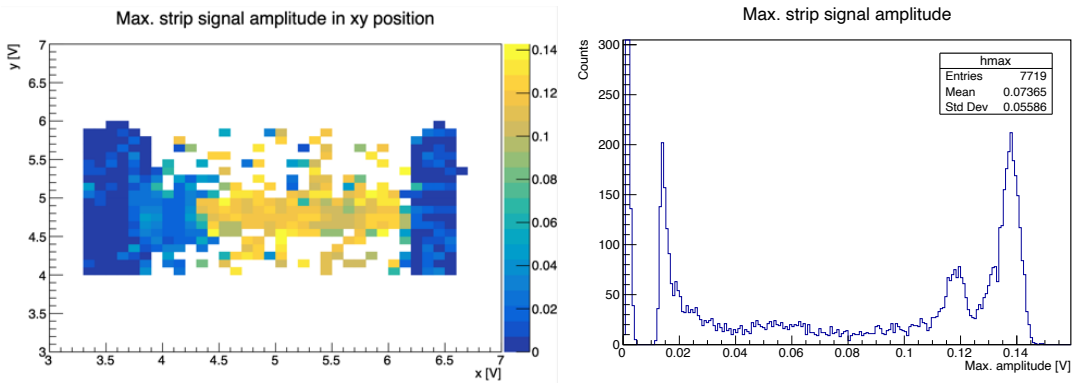

Figure 3.20: Bidimensional plot of the maximum amplitude of the strip signal waveform from Run 3 in a certain x,y position (conversion factor 1V=300μm, the color scale is expressed in Volts), left, and the distribution of the strip pulse maximum height, right.

The two peaks present at approximately 120 mV and 140 mV in the maximum pulse height distribution in Figure 3.20 have been further investigated: the bidimensional distribution of the frequency of triggers was studied dividing the data corresponding to the two peaks. The results are shown in Figure 3.21. Signals with amplitude approximately 120 mV comes from a localized are of the strip (3.21, left), which means that the strip behaves differently in that specific zone, probably due to a manufacturing unevenness.

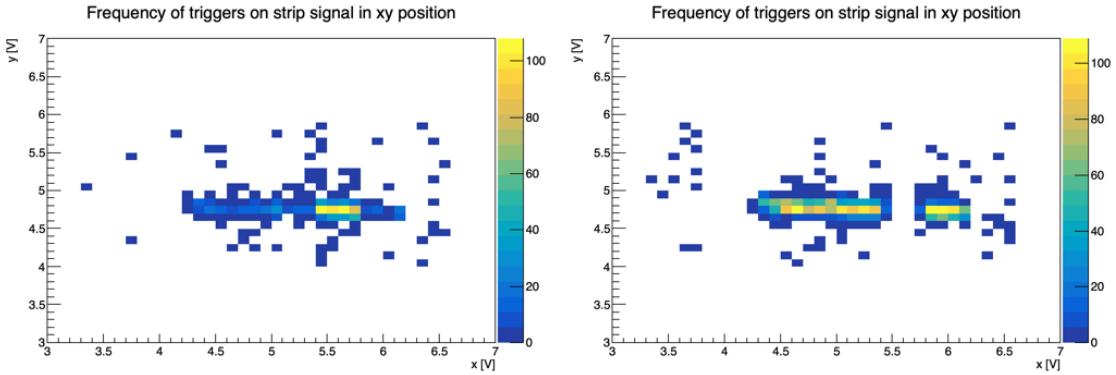

Figure 3.21: Bidimensional plot of the frequency of tiggers on strip signal, selecting the data coming from events with maximum amplitude in thee interval [105;125] mV (left) and [125;150] mV, with reference to Figure 3.20.

Given that the SiPM pulses have negative polarity, the distribution of the minimum of the waveforms was extrapolated. To estimate the minimum, a fit was performed in the first interval of the SiPM signal (Figure 3.18) with a constant function in order to estimate the baseline, which was then subtracted to the minimum value of the waveform. The results are displayed in Figure 3.22. The first peak appears at ≈ 2 mV: this peak is due to noise, as it will be shown in the following. The one photon peak arises at ≈ 3.5 mV, so the gain is similar to the one estimated in laboratory. Any difference is however justified since temperature changes imply also changes in the gain of the SiPM.
In general, most of the SiPM signals are induced by one or two photons.

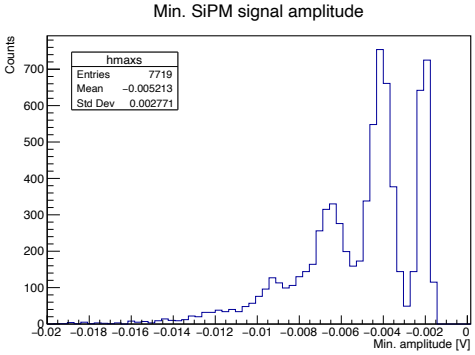

Figure 3.22: Distribution of the minimum of the SiPM waveforms.

Time resolution analysis

In order to perform the time resolution analysis, a proper selection of the events was needed:

- *Signals in time*: only events in which the SiPM signal was in time with the strip signal were considered. This was done requiring the SiPM signal appearance within 10 ns apart the strip signal.
- *Background rejection*: a selection on the maximum of the strip signals was performed in order to avoid noise induced signals.

These selections implied that starting from a data set of 7719 events, only 4003 were useful for the timing analysis. The distribution of the maximum of strip signals for the selected events is displayed in Figure 3.23 and one can notice that the peak around 0 V totally disappeared, since it has a non physical origin.

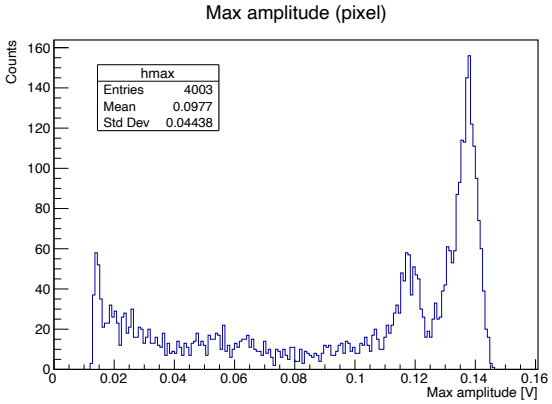

Figure 3.23: Distribution of the maximum of strip signal waveforms for the data from Run 3 selected for the timing analysis (trigger on strip signal at 10 mV, $V_{bias} = -100$ V).

The time of the signals t_0 was extracted by a fit of the waveforms of strip and SiPM signals using the function reported in Equation 3.1. The normalization parameter N was chosen in order to match the amplitude of the function with respectively the maximum for the strip pulse, the minimum for the SiPM pulse.

$$f(t) = \begin{cases} b_0 & t \leq t_0 \\ b_0 + A \cdot e^{t/\tau_F}(1 - e^{t/\tau_R})/N & t > t_0 \end{cases} \tag{3.1}$$

Finally the difference between the SiPM and strip reference times is taken: the result is displayed in Figure 3.24.
A Gaussian fit of the peak of the distribution was performed and its standard deviation gives the time resolution estimation. The results comes out to be ≈ 400 ps, meanwhile the expected result was of order of 50 ps.

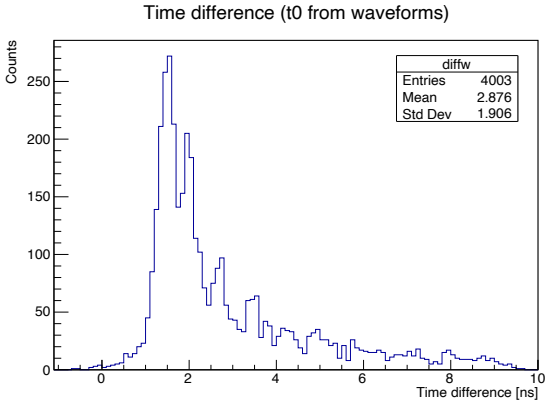

Figure 3.24: Time difference between SiPM and strip reference times from Run 3 data (trigger on strip signal at 10 mV, $V_{bias} = -100$ V).

In order to improve the resolution on the SiPM time the same analysis is performed dividing the strip signal events referred to different peaks in the SiPM voltage spectrum (Figure 3.25, left).
One can notice that the SiPM peak arising around -2 mV contributes with a uniform background to

the time difference distribution (Figure 3.25, right), so the first peak has to be attributed to noise. Moreover, requiring that the SiPM signal is induced by more than one photon implies that the time difference distribution becomes narrower. This effect is expected since the higher is the SiPM signal, the lower will be the jitter noise (as explained in Section 1.3). Performing a Gaussian fit of the distribution regarding the highest SiPM pulses gives a time resolution of 350 ps.

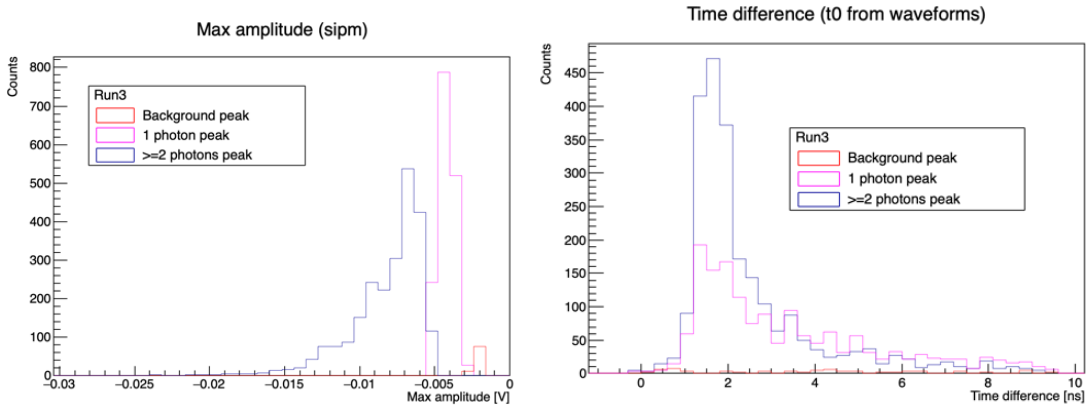

Figure 3.25: Distribution of the minimum of the SiPM signal waveforms for the data selected for the timing analysis (left) and time difference between SiPM and strip reference times, dividing the strip signal events with respect to the relative SiPM signal amplitude (right). (Trigger on strip signal at 10 mV, $V_{bias} = -100$ V)

3.2.1.2 Run 18 analysis

Run 18 was acquired with the trigger at 70 mV on the strip signal waveform and a bias voltage on the strip equal to $V_{bias} = -50$ V. The signal events collected were of the kind reported in Figure 3.26.
In Figure 3.26, right, there are the so called "trains" of noise: these sets of subsequent strip signals are induced by radiation damage. In Figure 3.26, left, there is a single strip signal (in blue) useful for the time resolution analysis, but the SiPM signal (in orange) is degraded, probably due to the consumption of the P-terphenyl layer during the test beam time.

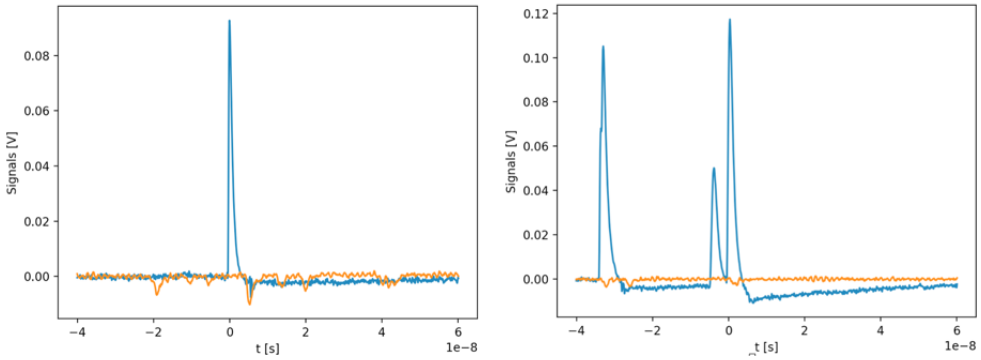

Figure 3.26: Typical waveforms recorded during Run 18 acquisition ($V_{bias} = -50$ V and the trigger on the strip signal at 70 mV). The strip signal is in blue, the SiPM signal is in orange.

Pulse height analysis

The bidimensional plot of the frequency of triggers on the strip signal waveform with trigger at 70 mV and $V_{bias} = -50$ V is displayed in Figure 3.27. Figure 3.28 shows the bidimensional plot of the maximum amplitude of the strip signal waveform (left) and the distribution of the maximum strip pulses height (right).

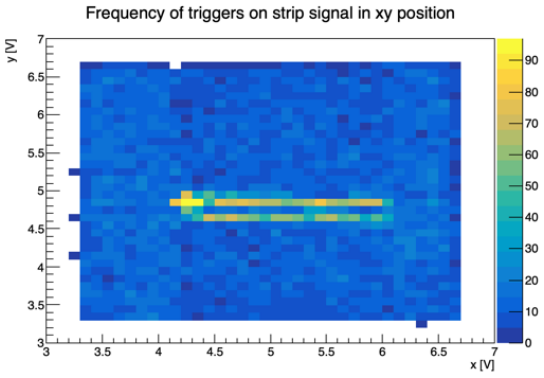

Figure 3.27: Bidimensional plot of the frequency of triggers on the strip signal waveform with trigger at $70mV$ and $V_{bias} = -50$ V (conversion factor 1V=300μm).

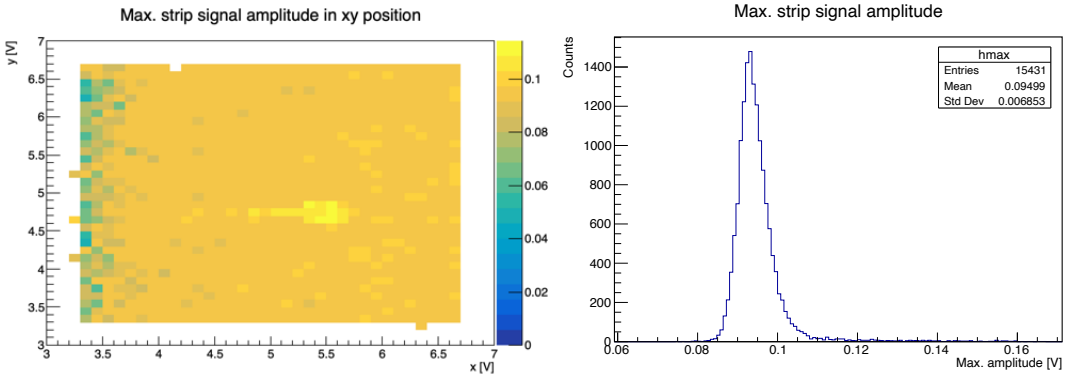

Figure 3.28: Bidimensional plot of the maximum amplitude of the strip signal waveform from Run 18 in a certain x,y position (conversion factor 1V=300μm, the color scale is expressed in Volts), left, and the distribution of the strip pulse maximum height, right.

In Figure 3.27 one can notice the sensitive area of the device highlighted, since most of the events are triggered in that region. However, there is also a uniform distribution of few events which are triggered outside the sensitive region. Moreover, looking in Figure 3.28, left, the distribution of the maximum value of the strip waveforms have a uniform distribution in the x,y plane. This implies the following consideration.
Since the proton beam intensity can be adjusted using two sets of sledges positioned outside the accelerator and right before the rastering system, it can happen that if a proton collides with the sledges its trajectory can divert from the one of the collimated beam. This implies that when the deviated proton encounters the electric fields used to deflect the beam, even though the rastering system predicts it to hit a certain region, in reality the proton hits the sensible region and thus a signal is induced.
This hypothesis is validated if one constraints the data analysis to inside and outside the sensitive region, as highlighted in Figure 3.29.

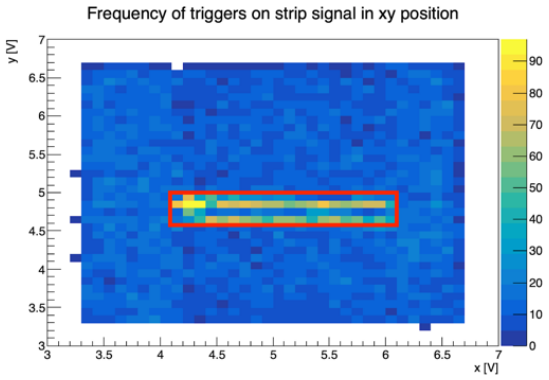

Figure 3.29: Bidimensional plot of the frequency of triggers on the strip signal waveform with highlighted the region chosen to divide the analysis in inside and outside the sensitive zone.

The time resolution analysis have been performed in the same way illustrated in Section 3.2.1.1, but the data selection was stricter since the events related to "trains" must be discarded for the timing analysis.

The selection criteria were the following:

- *Signals in time*: only events in which the SiPM signal was in time with the strip signal were considered. This was done requiring the SiPM signal appearance within 10 ns apart the strip signal.
- *Trains rejection*: if more than one pulse is present before the time $t = 0$, the event is discarded. This allows to keep "train" events in which multiple pulses are present after the triggering signal, so that the timing analysis is still possible.

Starting from a statistics of 15468 events, 1243 of them were "trains". Of the remaining events, only 4010 had the strip and SiPM signal in time, due to the degradation of the SiPM signal previously shown.
The results for the distribution of the maximum of strip waveforms and for the time difference between strip and SiPM signal is shown in Figure 3.30. Apart from statistics, the distributions do not show significant differences, so the hypothesis of the protons deviated from the collimated beam seems validated.

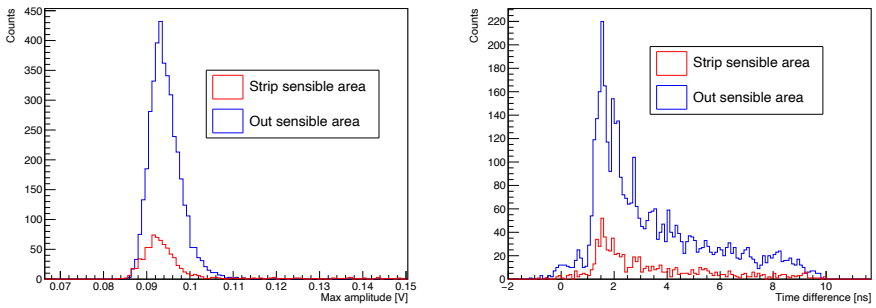

Figure 3.30: Distribution of the maximum of strip waveforms and for the time difference between strip and SiPM signal relative to the regions inside and outside the sensor sensitive zone.

Time resolution analysis

The time resolution analysis was performed also in this case subdividing the events relative to different SiPM signal amplitudes (Figure 3.31, left). The result is displayed in Figure 3.31, right. Also in this case, requiring that the photons hitting the SiPM are more than one makes the time difference

distribution narrower. Performing a Gaussian fit of the distribution regarding the highest SiPM pulses gives a time resolution of 460 ps.

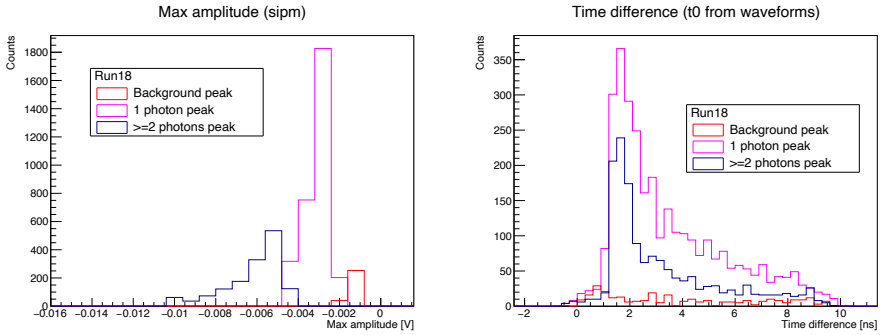

Figure 3.31: Distribution of the minimum of the SiPM signal waveforms for the data selected for the timing analysis (left) and time difference between SiPM and strip reference times, dividing the strip signal events with respect to the relative SiPM signal amplitude (right). The trigger level was 70 mV, $V_{bias} = -50$ V.

3.2.1.3 Run 16 analysis

Moving the trigger level on the strip signal to 90 mV, keeping the $V_{bias} = -50$ V, changes the type of strip signals observed and their distribution. Some examples are reported in Figure 3.32. In these conditions what it is observed are the strip signals related to two protons which hit the sensor at the same time: as it is possible to see in Figure 3.32, left, the signal maximum is at ≈ 175 mV, which is approximately two times the signals observed in the case of trigger at 70 mV (Figure 3.30, left). The two signals relative to the pair of protons can be perfectly overlapping, as in the case of Figure 3.32, left, or partially overlapping, showing the typical double-peaked waveforms that one can see in Figure 3.32, center. Alongside these two kinds of signals, there are also the radiation damage induced "trains" (3.32, right).

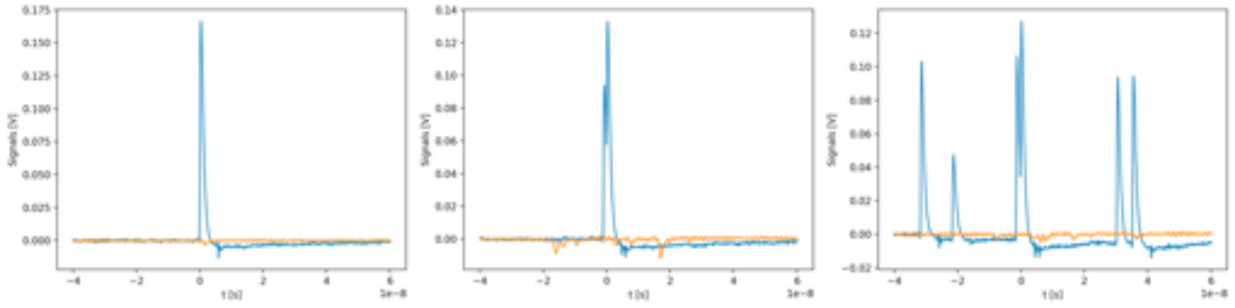

Figure 3.32: Typical waveforms recorded with the strip at $V_{bias} = -50$ V and the trigger on the strip signal at 90 mV. The strip signal is in blue, the SiPM signal is in orange.

Pulse height analysis

The bidimensional plot of the frequency of triggers on the strip signal waveform with trigger at 90 mV and $V_{bias} = -50$ V are reported in Figure 3.33. In this case the events are more localized in the sensor sensitive area: this happens because the probability that a proton deviated by the collimator hits the sensitive area of the sensor in coincidence with another proton is quite low.

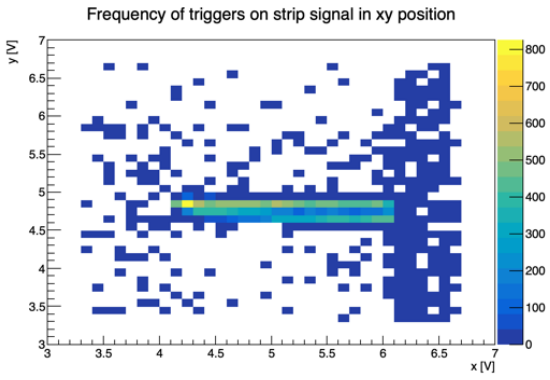

Figure 3.33: Bidimensional plot of the frequency of triggers on the strip signal waveform with trigger at 90 mV and $V_{bias} = -50$ V (conversion factor 1V=300μm).

Figure 3.34 shows the bidimensional plot of the maximum amplitude of the strip signal waveform (left) and the distribution of the maximum strip pulses height (right). As one can see in Figure 3.34, right, the typical height of the pulses from this data acquisition almost doubles the ones taken in Run 18.

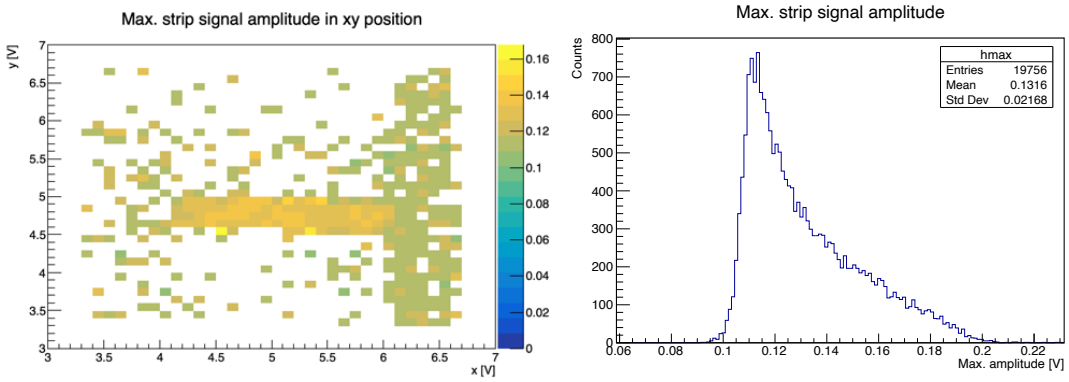

Figure 3.34: Bidimensional plot of the maximum amplitude of the strip signal waveform from Run 16 in a certain x,y position (conversion factor 1V=300μm, the color scale is expressed in Volts), left, and the distribution of the strip pulse maximum height, right.

Time resolution analysis

For completeness the time resolution analysis have been performed also in this trigger condition.

The selection criteria were the following:

- *Signals in time*: only events in which the SiPM signal was in time with the strip signal were considered. This was done requiring the SiPM signal appearance within 10 ns apart the strip signal.
- *Trains rejection*: if more than one pulse is present before the time $t = 0$, the event is discarded. This allows to keep "train" events in which the multiple pulses are present after the triggering signal, so that the timing analysis is still possible.
- *Double-peaked pulses selection*: events with two pulses partially overlapped are kept, considering for the timing analysis only the first peak.

Starting from a statistics of 20067 events, 6274 of them were "trains". Of the remaining events, only 6431 had the strip and SiPM signal in time.
The events were subdivided with reference to different SiPM signal amplitudes (Figure 3.35, left). The result is displayed in Figure 3.35, right. Performing a Gaussian fit of the distribution regarding the highest SiPM pulses gives a time resolution of 480 ps.

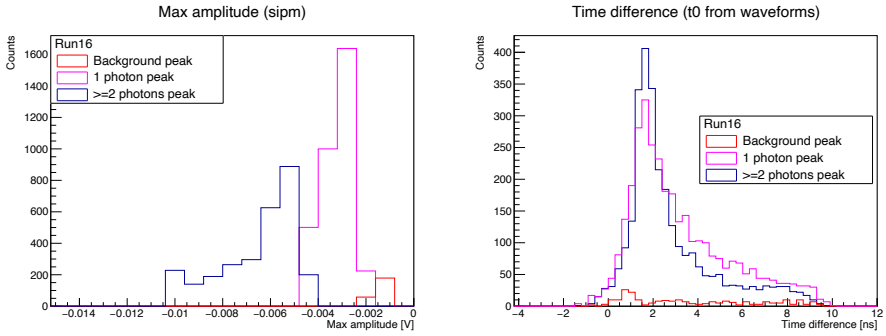

Figure 3.35: Distribution of the minimum of the SiPM signal waveforms for the data selected for the timing analysis (left) and time difference between SiPM and strip reference times, dividing the strip signal events with respect to the relative SiPM signal amplitude (right). The trigger level was 90 mV, $V_{bias} = -50$ V.

3.2.1.4 Run 3,16,18: summary

The results obtained with the time resolution analysis are reported in Table 3.2.

	σ_t [ps]
Run 3	350
Run 16	460
Run 18	480

Table 3.2: Summary of time resolution estimation obtained analyzing Run 3, 16, 18.

3.2.1.5 SiPM time resolution estimation with laser for low amplitude pulses

The strip time resolution extrapolation was not possible with the sets of data from Run 3, 16, 18 because the SiPM time resolution worsens when its pulse amplitude is low. To perform a good timing analysis high signals are needed: possible solutions will be to increase the number of photons reaching the SiPM or to improve the amplifier of the signal itself.
To check this fact, a study of the SiPM time resolution with such low amplitude signals was performed using the fast blue laser and the Lecroy oscilloscope. The laser, at its minimum intensity and properly diffused with some pieces of paper, was pointed directly to the SiPM, in order to produce signals of order of mV. The trigger exit of the laser and the output of the amplifier of the SiPM were connected to the oscilloscope. Finally, triggering on the laser signal, approximately 10000 laser and SiPM waveforms were recorded in the oscilloscope binary files.
As in the case of the test beam data, the file was then converted to a ROOT file and the SiPM signal was fitted in the same way described above, by means of Equation 3.1. The reference time for the laser signal was taken as the time of the 50% of the signal itself, since it is the point of maximum derivative. The difference between laser and SiPM was taken and the time resolution was estimated by a gaussian fit of the distribution.
Adjusting the laser intensity, several data acquisition were recorded, in order to find a trend of the SiPM time resolution as a function of the magnitude of the signal amplitude. So for each data acquisition, the most frequent minimum amplitude of the SiPM signal was evaluated by fitting the histogram of their distribution.
Given the absolute value of the most frequent amplitude and the time resolution value, the results are displayed in Figure 3.36. As expected, for signals of order of few mV the time resolution is of the order of ≈ 400 ps.

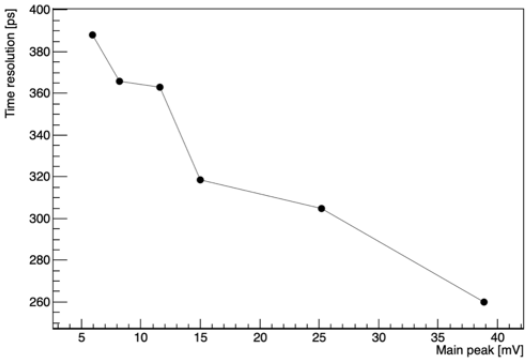

Figure 3.36: SiPM time resolution evaluated with the blue laser in function of the main signal peak which arose.

3.2.1.6 Run 8,10,11: qualitative analysis

Other data acquisition were taken at different V_{bias}, but, due to poor statistics, they were not considered for the timing analysis. Anyway, I report in Figure 3.37 the bidimensional plot of the frequency of triggers and the bidimensional plot of the maximum amplitude of the strip signal waveform for different trigger conditions at $V_{bias} = -40$ V.
Figure 3.37, central column, was taken from data with trigger on the strip signal but at a negative level: in this way only "train" signals are selected, they are the only ones having a relevant underflow. These signals come exclusively from the sensor sensitive region.
Finally, Figure 3.37, right column, displays the data taken with trigger on the SiPM signal: looking at the distribution of the maximum of the strip signals, it is possible to see that the sensitive region have the highest signals. Regarding the frequency plot, it is possible to notice the shape of the Timespot device, as it is pointed out in Figure 3.38. The frequency of trigger on the SiPM signal is strictly linked to the layer of P-terphenyil and on the reflectivity of the surface over which it is deposited. So it makes sense that the signals are most frequent right above the squared metallic pads of the device.

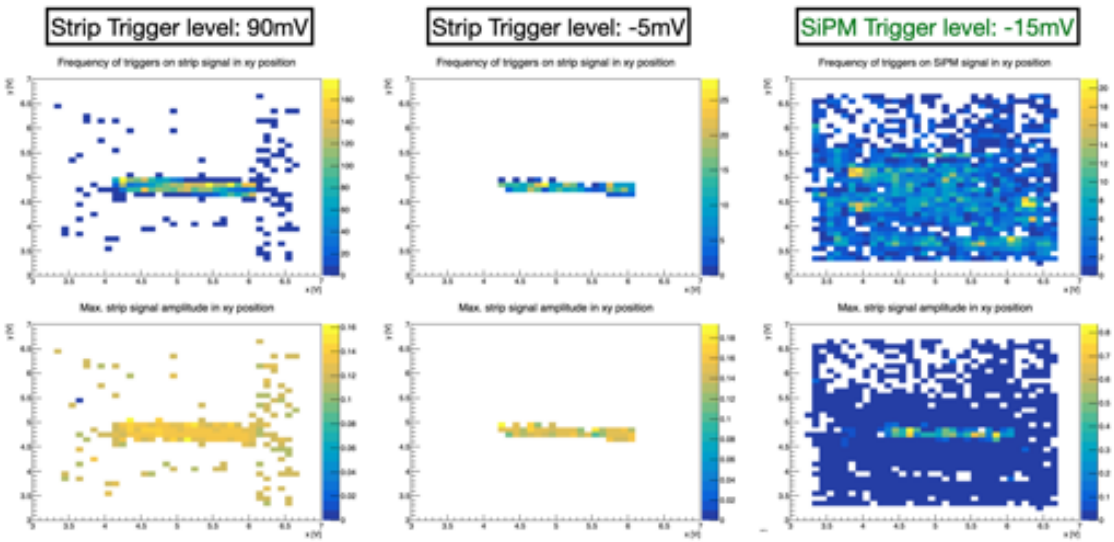

Figure 3.37: Bidimensional plot of the frequency of triggers (up) and bidimensional plot of the maximum amplitude of the strip signal waveform (down) for different trigger conditions, written on top of the three columns. $V_{bias} = -40$ V.

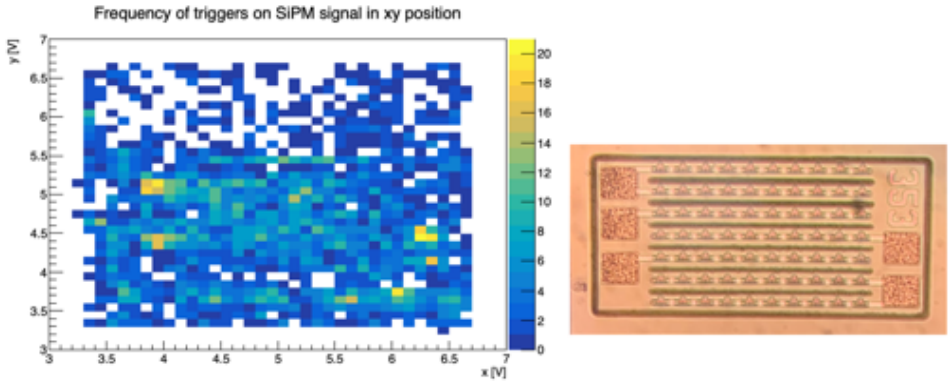

Figure 3.38: Comparison between the bidimensional plot of the frequency of trigger on the SiPM signal with the shape of the Timespot strip device.

3.2.1.7 I-V characteristics

In the final part of the test beam, after each proton irradiation an I-V characteristics of the strip device was recorded using the Keithley. The result is shown in Figure 3.39, left (uncertainties on current and voltages are too small to appear in the plot). After each irradiation, the breakdown voltage becomes closer to zero as a consequence of the irradiation damage.
Another I-V characteristics was taken one month after the irradiation; its comparison with the last step irradiation characteristic is displayed in Figure 3.39, right. There is a visible annealing since the breakdown is now higher than 100 V in absolute value. Anyway, the leakage current is still high with respect to the one measured before irradiation (Figure 3.4): this could mean that the annealing is still not complete or that some bulk damage could be present.

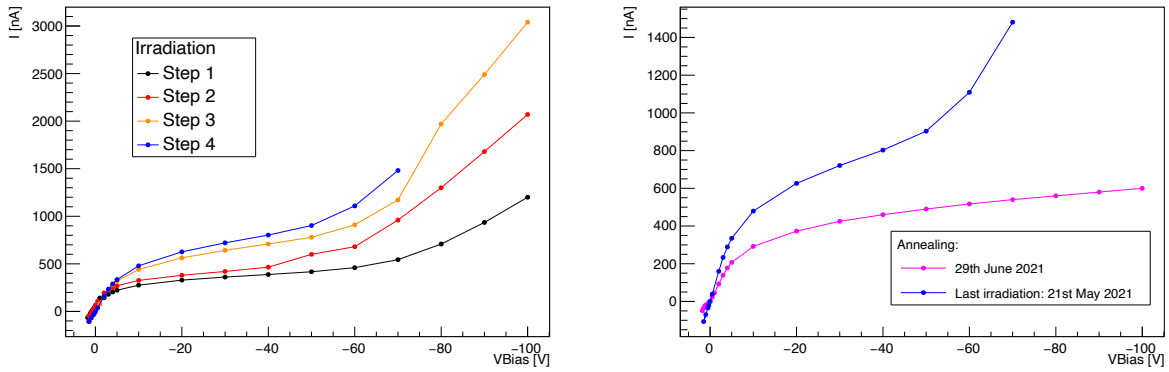

Figure 3.39: I-V characteristics of the strip device taken after subsequent irradiation (left) and the comparison between the last step of irradiation I-V characteristic with the one recorded one month after (right).

Chapter 4

Conclusions

During the high luminosity runs of the LHC collider the detectors will face great challenges due to the increase in the particle density. Precise time information will be fundamental to maintain a good detector performance, in particular for subdetectors which are really close to the beamline, as in the case of LHCb VELO.
The TIMESPOT project aims at developing a complete tracking demonstrator capable of copying with such high luminosities and can offer a possible solution to the issues coming with it.
In this context, 3D-trenched electrode silicon sensor with timing precision of order of 10 ps and high radiation resistance are fully characterized. Several devices with different trench geometries have been studied in order to find the best design, guarantying the highest breakdown voltage possible, low leakage currents and low capacitance.
Also a dynamic characterization of a 3D strip has been performed, first using a fast laser, finding a time resolution of order of 10 ps. Then the strip have also been characterized using a 2 MeV-proton beam at the AN2000 accelerator in Legnaro: an innovative setup, built using a layer of organic scintillator deposited above the strip and a SiPM facing it, allowed to make an estimation of the time resolution of the device. The data collected during this test beam did not allow a satisfying time resolution estimation, because the geometry of the setup implied a low number of photons reaching the SiPM, degrading its time resolution. Further test beams will need to be performed in order to perform a timing analysis with enough precision, increasing the layer of the organic scintillator or the number of photons reaching the SiPM.

In conclusion, the TIMESPOT 3D sensors demonstrated to be efficiently working, being a possible solution for the need of precise timing information that will arise with the next generation LHC experiments.

Appendix A

Characterization of batch 2 Timespot devices

A.1 Strip devices

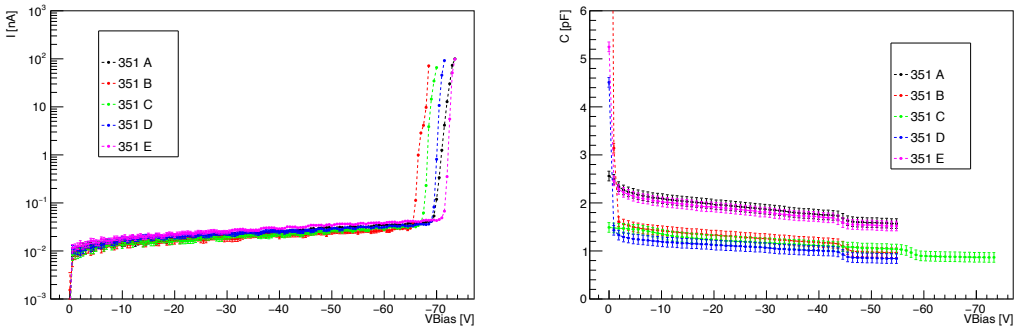

Figure A.1: I-V (left) and C-V (right) characterization of strip device number 351.

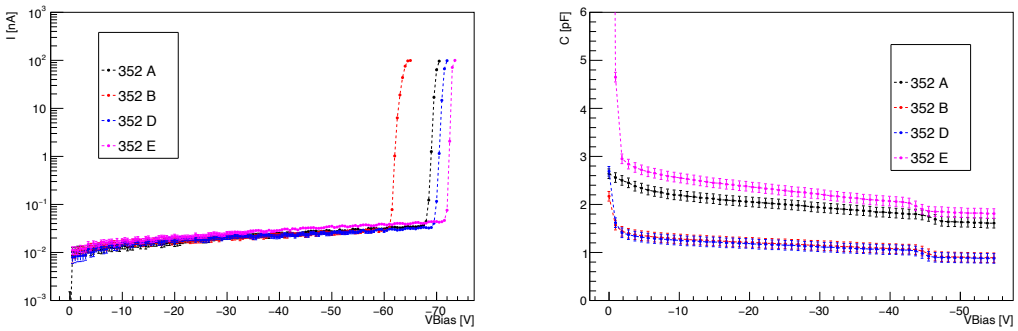

Figure A.2: I-V (left) and C-V (right) characterization of strip device number 352.

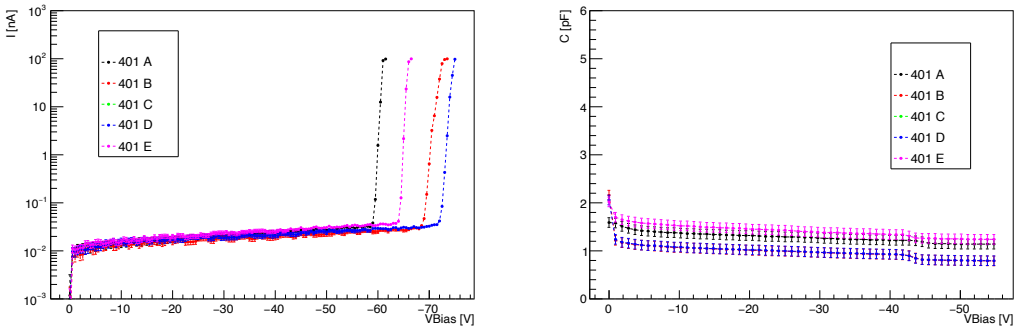

Figure A.3: I-V (left) and C-V (right) characterization of strip device number 401.

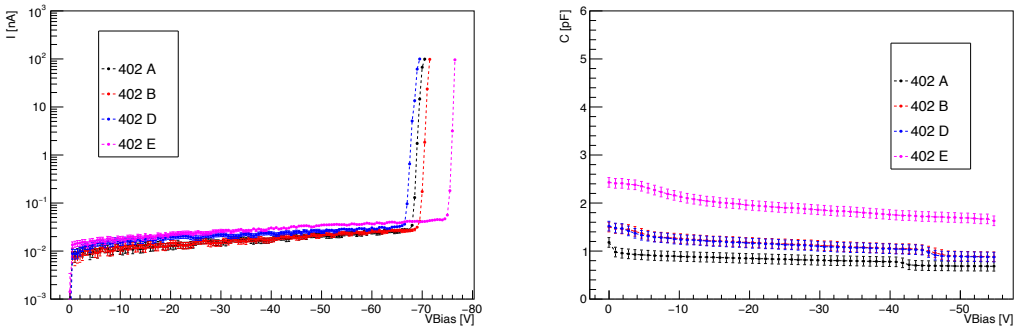

Figure A.4: I-V (left) and C-V (right) characterization of strip device number 402.

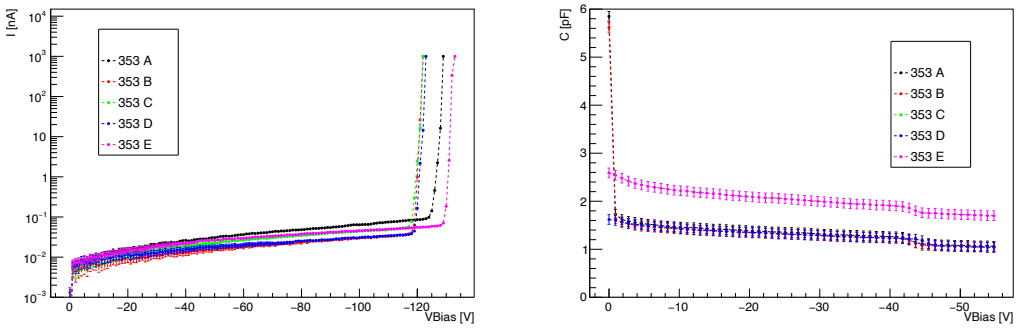

Figure A.5: I-V (left) and C-V (right) characterization of strip device number 353.

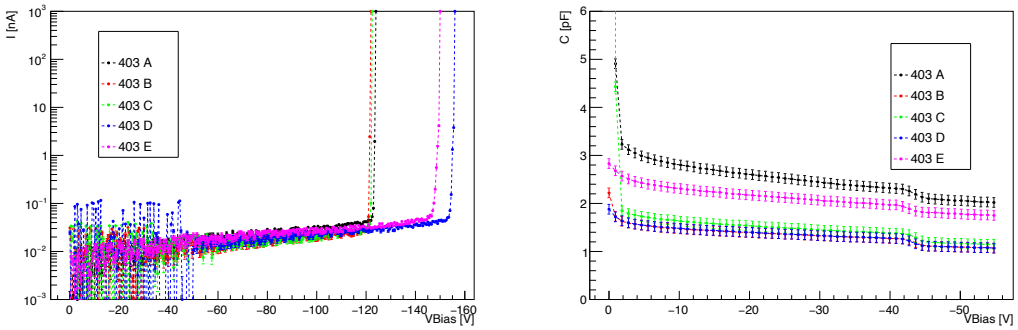

Figure A.6: I-V (left) and C-V (right) characterization of strip device number 403.

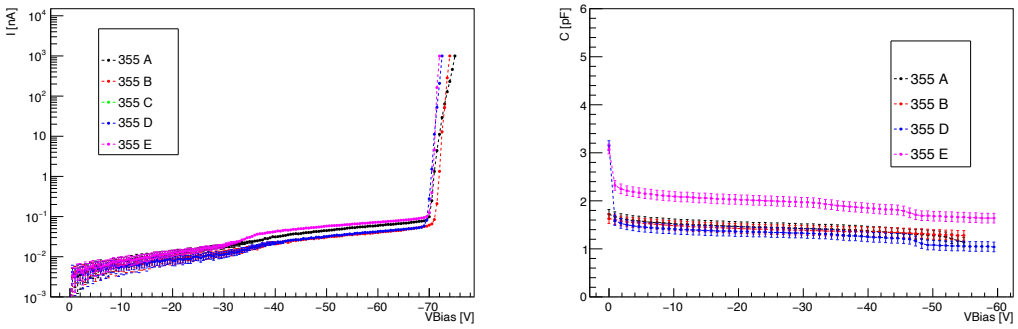

Figure A.7: I-V (left) and C-V (right) characterization of strip device number 355.

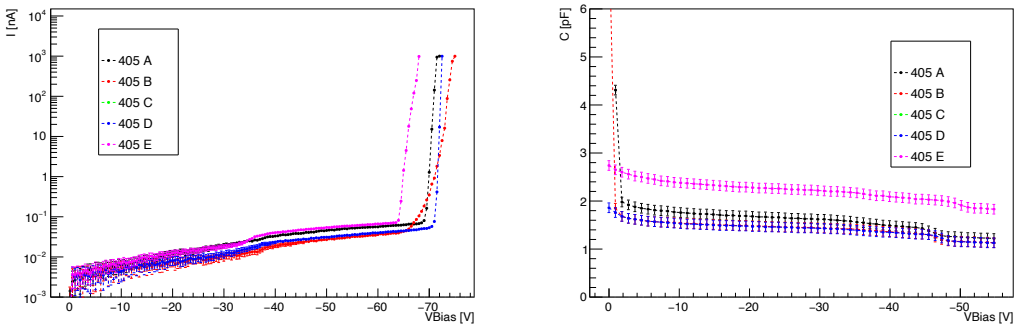

Figure A.8: I-V (left) and C-V (right) characterization of strip device number 405.

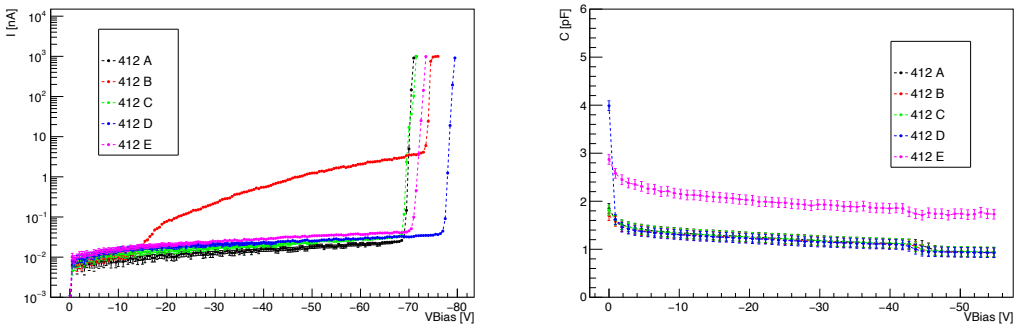

Figure A.9: I-V (left) and C-V (right) characterization of strip device number 412.

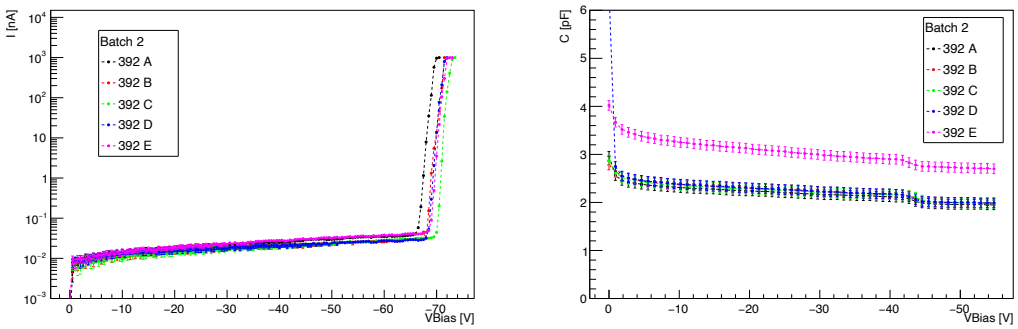

Figure A.10: I-V (left) and C-V (right) characterization of strip device number 392.

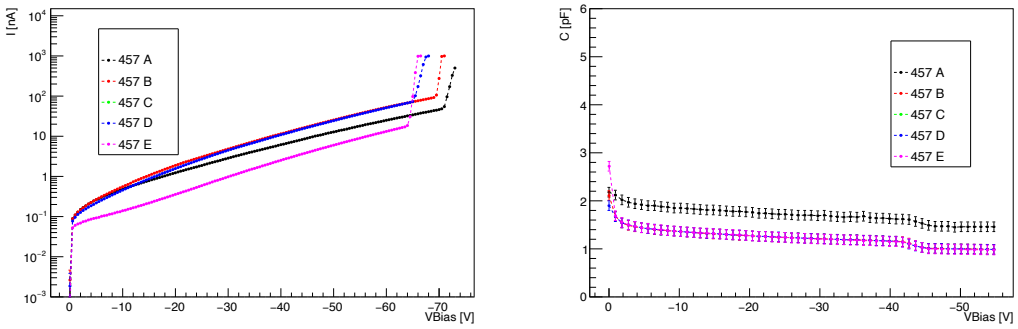

Figure A.11: I-V (left) and C-V (right) characterization of strip device number 457.

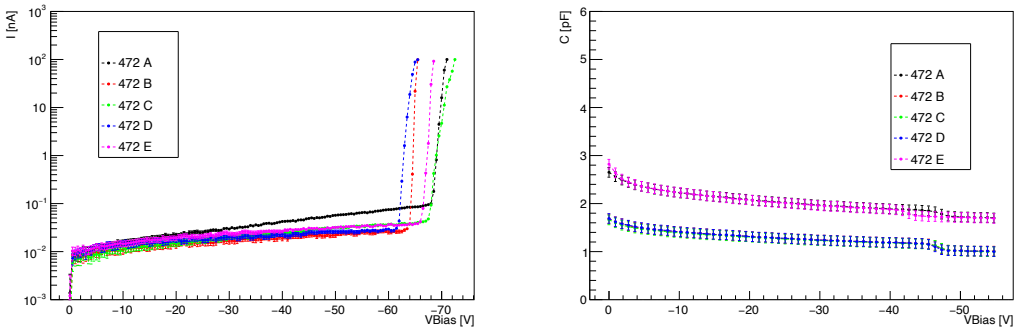

Figure A.12: I-V (left) and C-V (right) characterization of strip device number 472.

A.1.1 Comparison between strip devices with different metallic contacts geometries

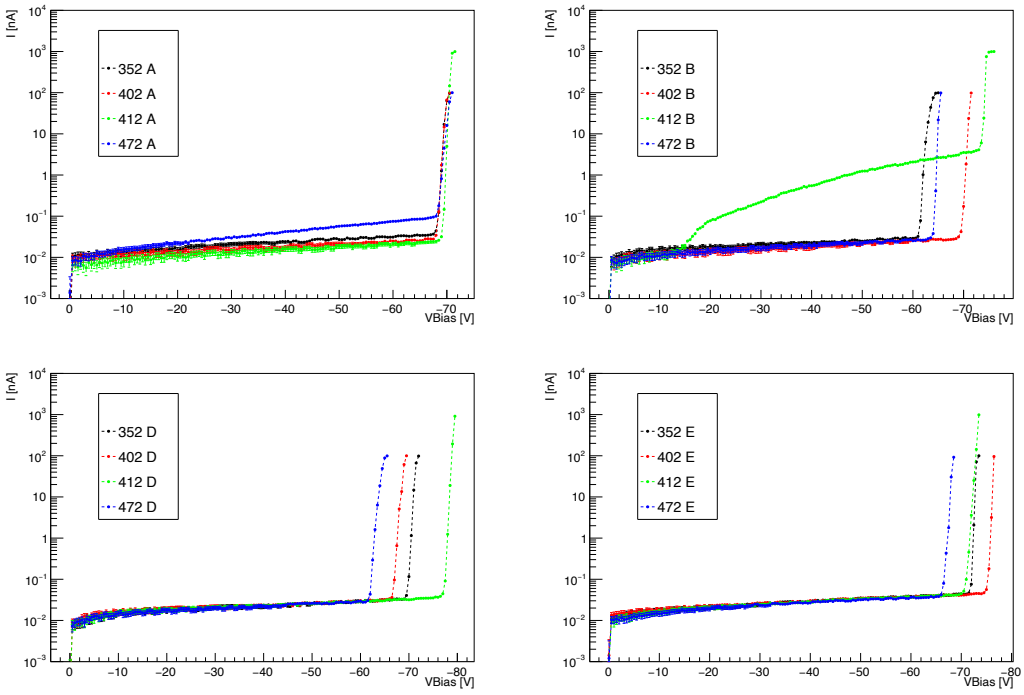

Figure A.13: Comparison between strip devices with same metallic contact geometry (number 2) but different length of the n-doped trenches.

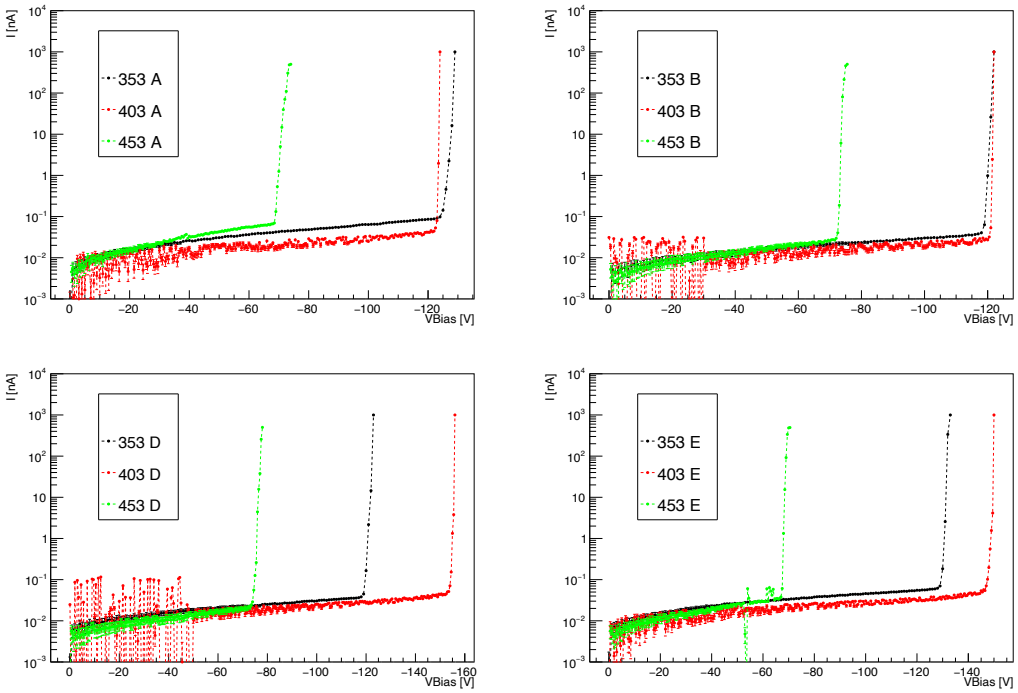

Figure A.14: Comparison between strip devices with same metallic contact geometry (number 3) but different length of the n-doped trenches.

A.1.2 Comparison between strip devices with different length of the n-doped trench

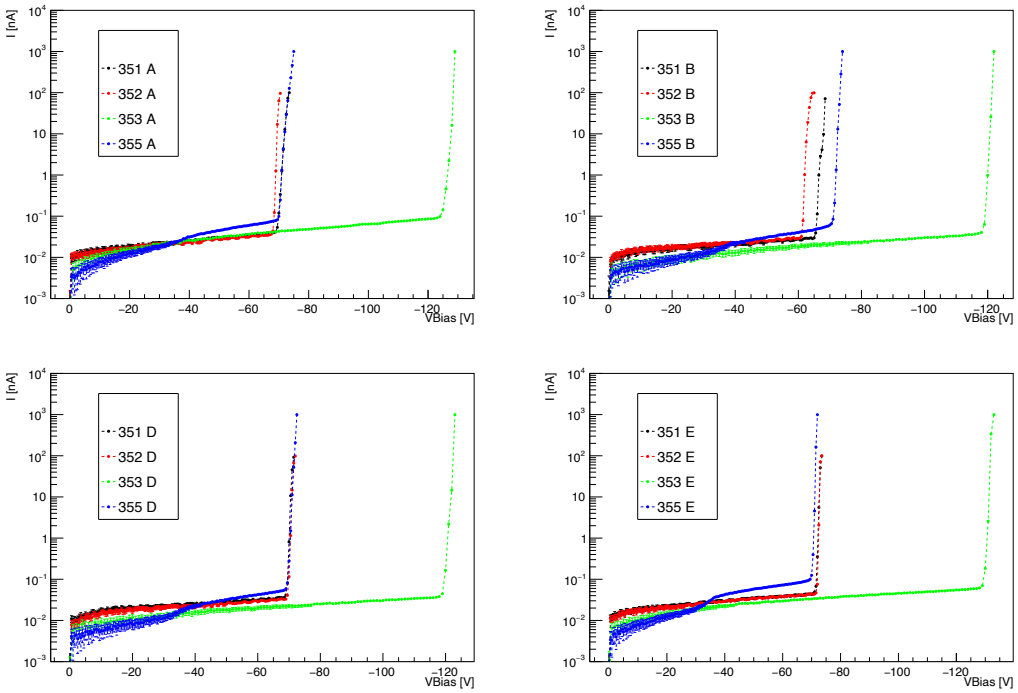

Figure A.15: Comparison between strip devices with same length of the n-doped trenches (35μm) but different metallic contact geometry.

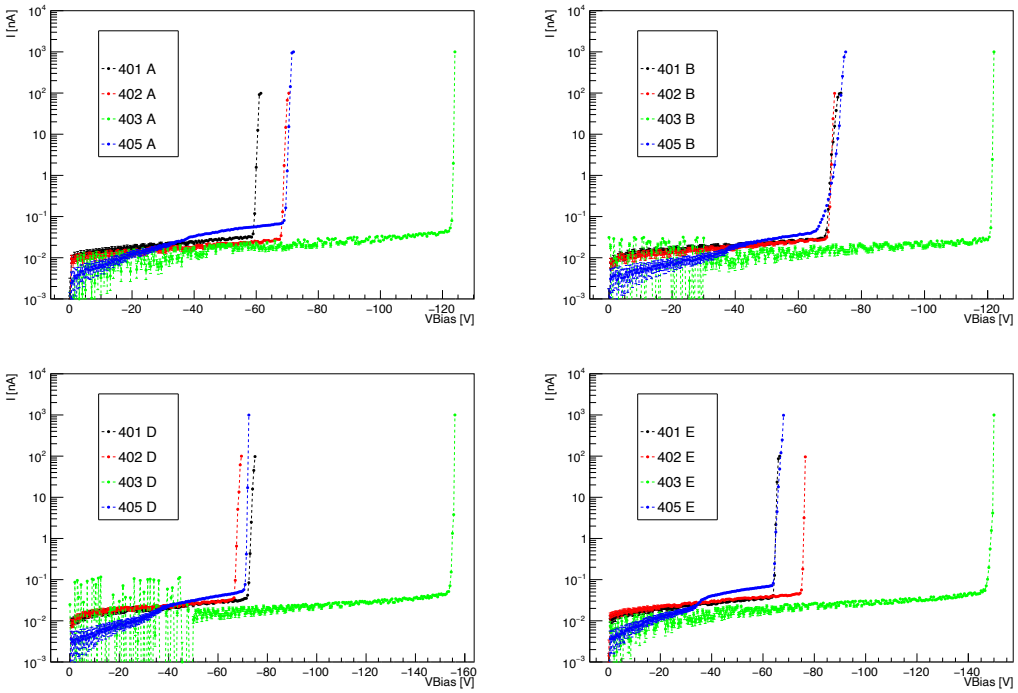

Figure A.16: Comparison between strip devices with same length of the n-doped trenches (40μm) but different metallic contact geometry.

A.1.3 Irradiation with X-rays

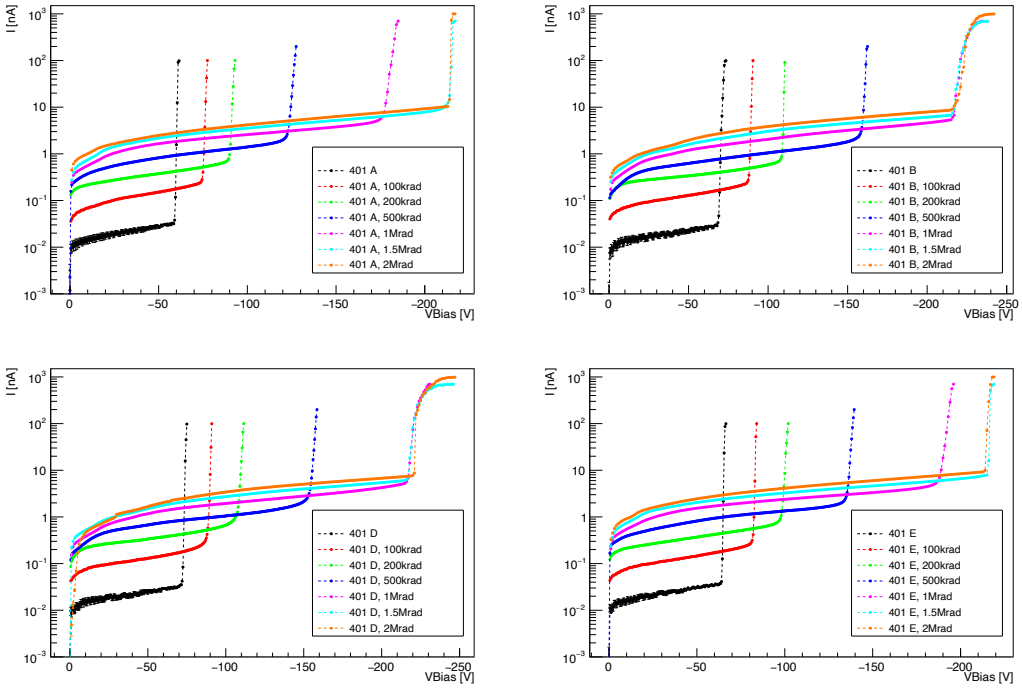

Figure A.17: I-V characteristics of the five pad of strip device number 401 under irradiation of X-rays.

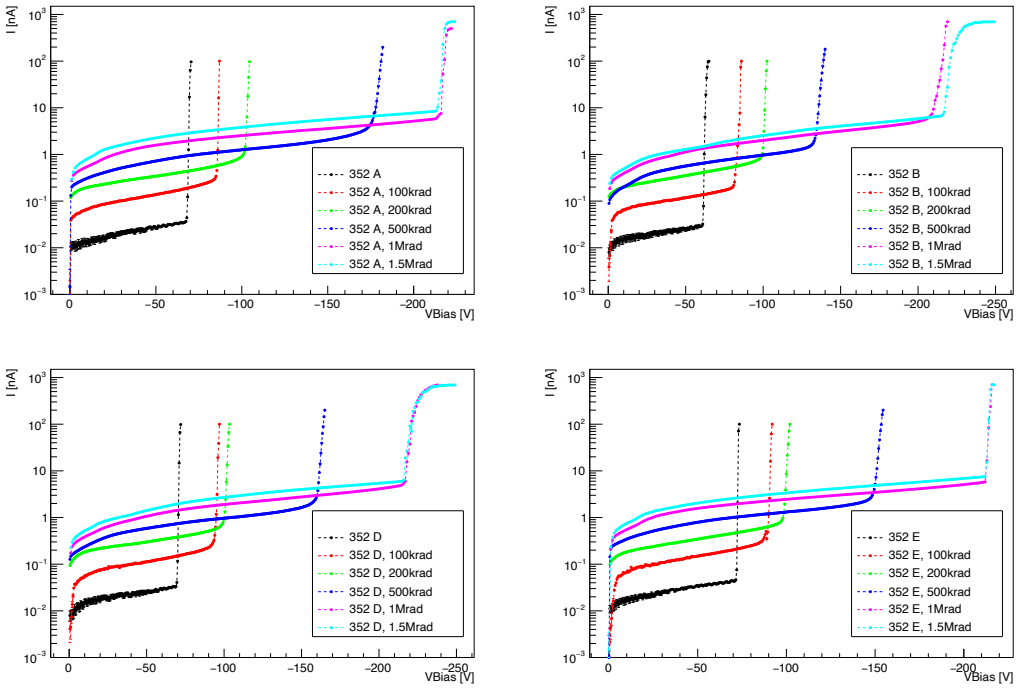

Figure A.18: I-V characteristics of the five pad of strip device number 352 under irradiation of X-rays.

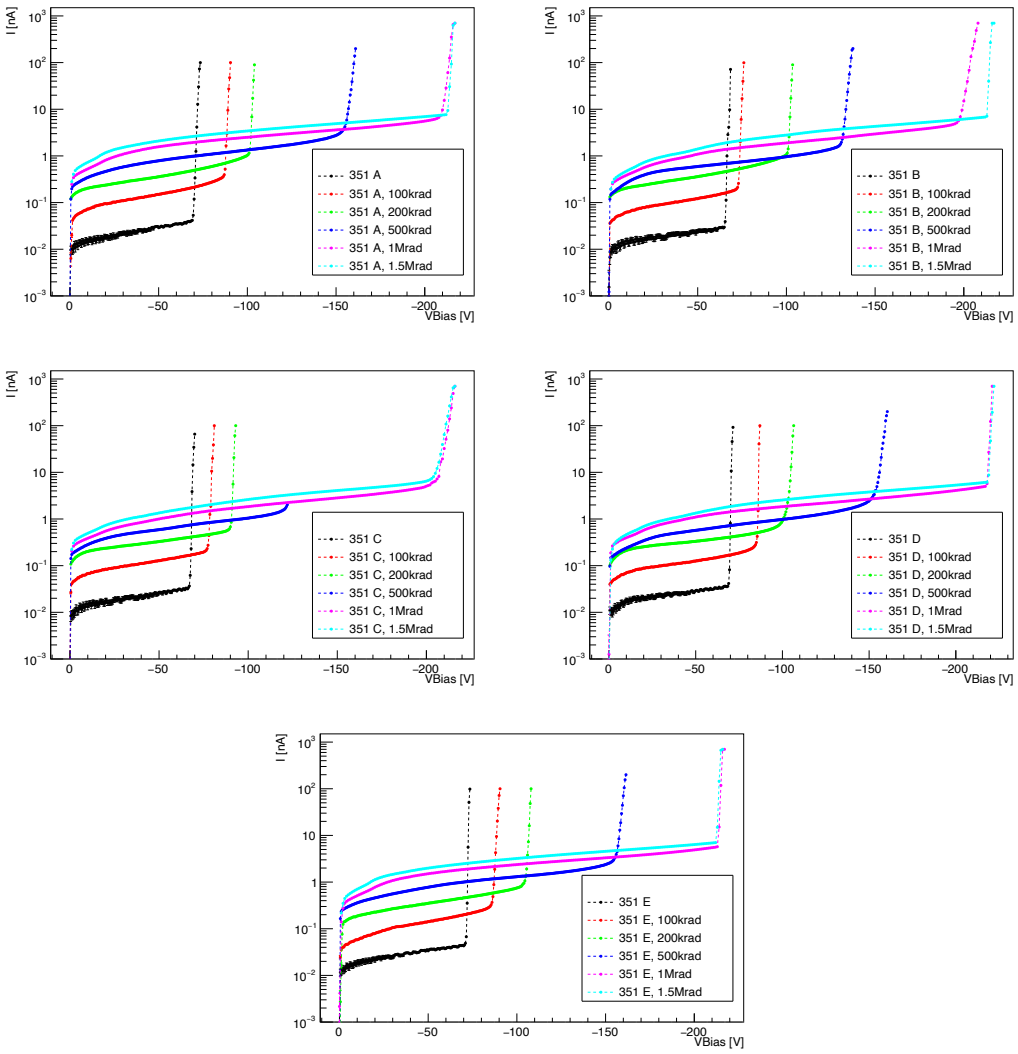

Figure A.19: I-V characteristics of the five pad of strip device number 351 under irradiation of X-rays.

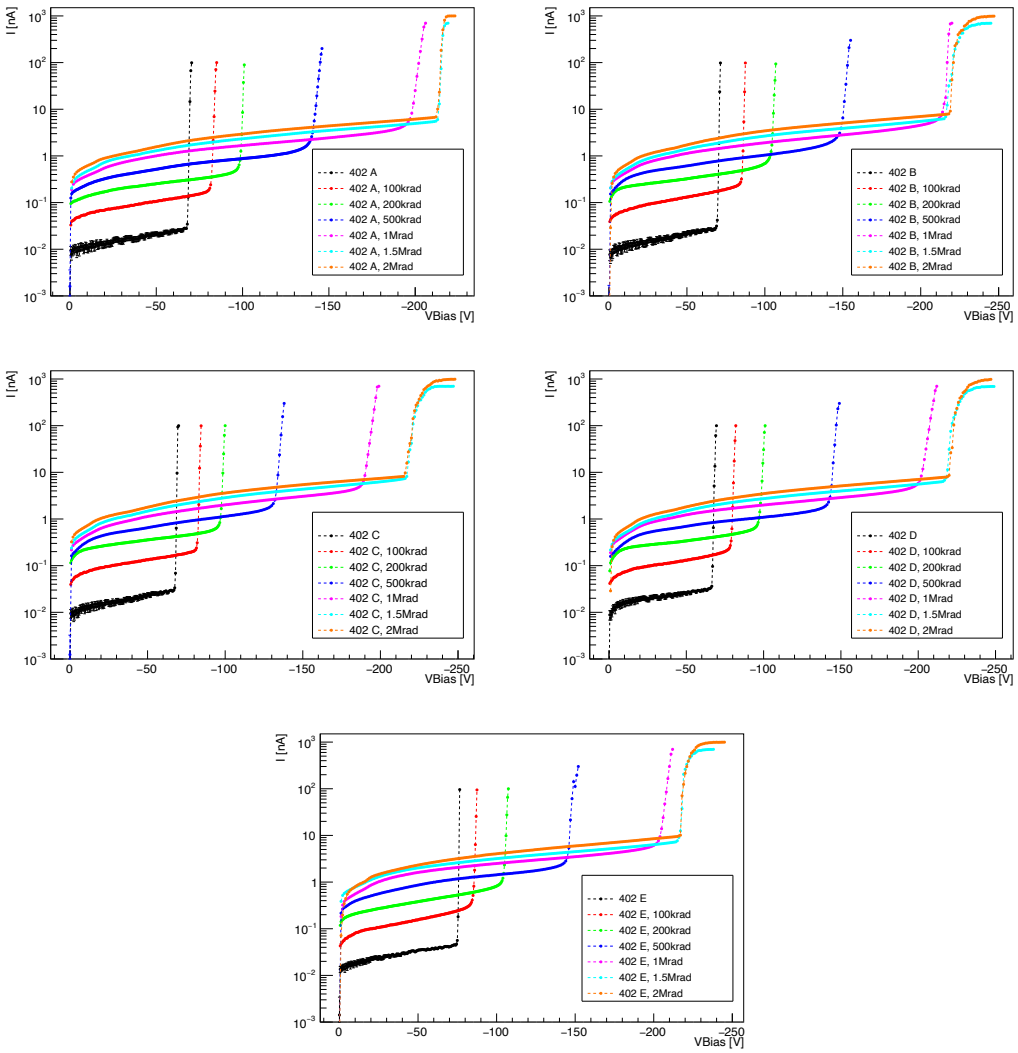

Figure A.20: I-V characteristics of the five pad of strip device number 402 under irradiation of X-rays.

A.1.4 Inter-strip resistance

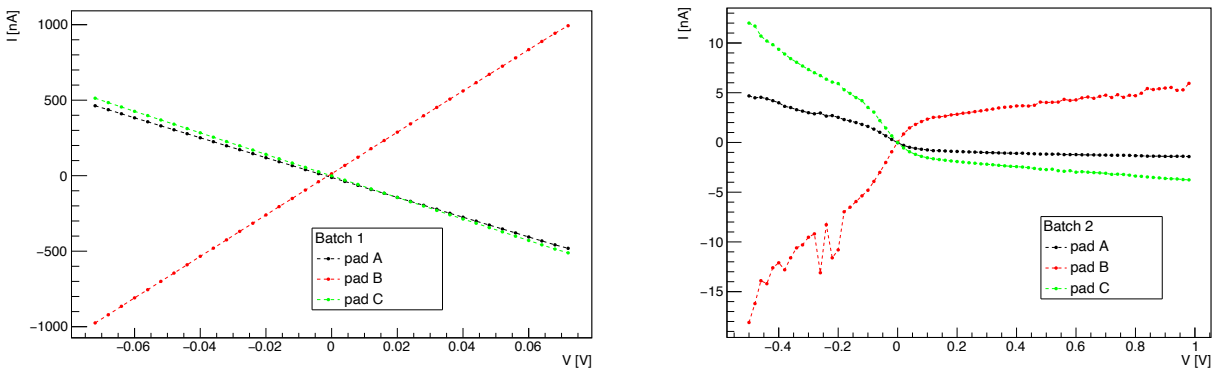

Figure A.21: Current flowing in strips A,B,C from device number 392 in the case of batch 1 (left) and batch 2 (right).

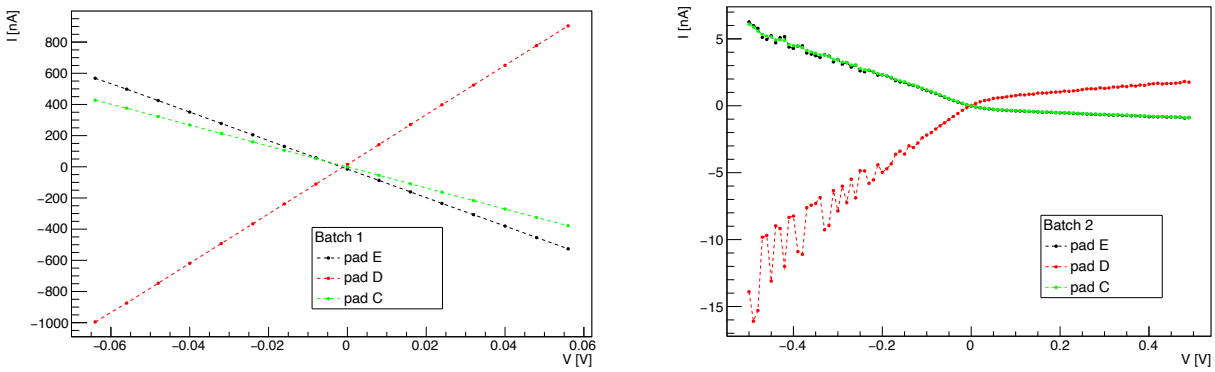

Figure A.22: Current flowing in strips C,D,E from device number 392 in the case of batch 1 (left) and batch 2 (right).

A.2 Pixel devices

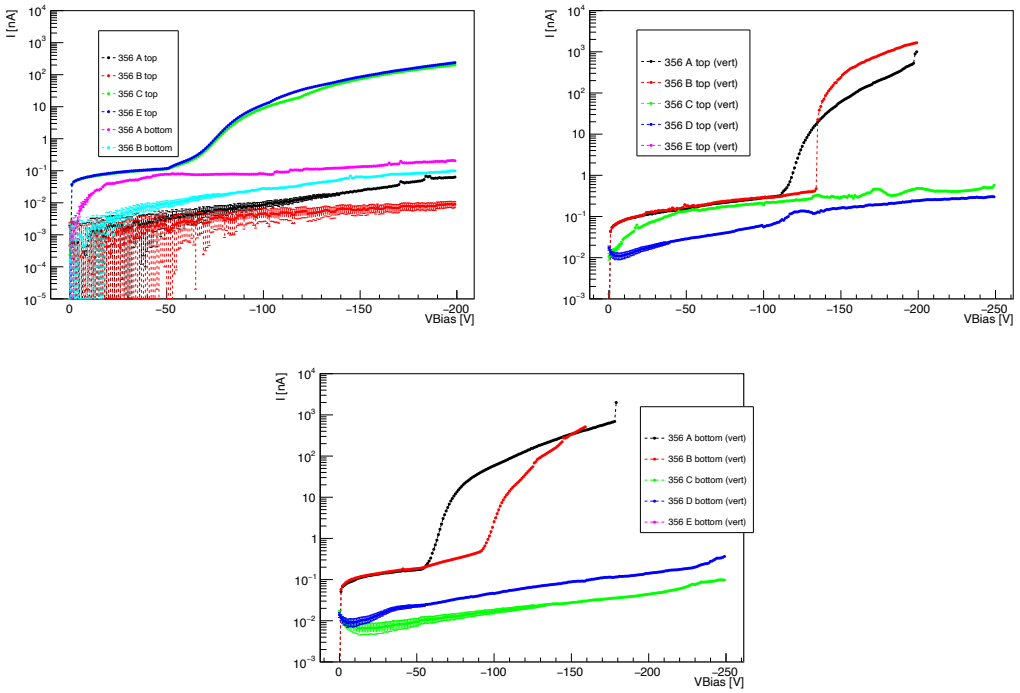

Figure A.23: I-V characteristics of pixel device number 356 in its two versions (vert or not).

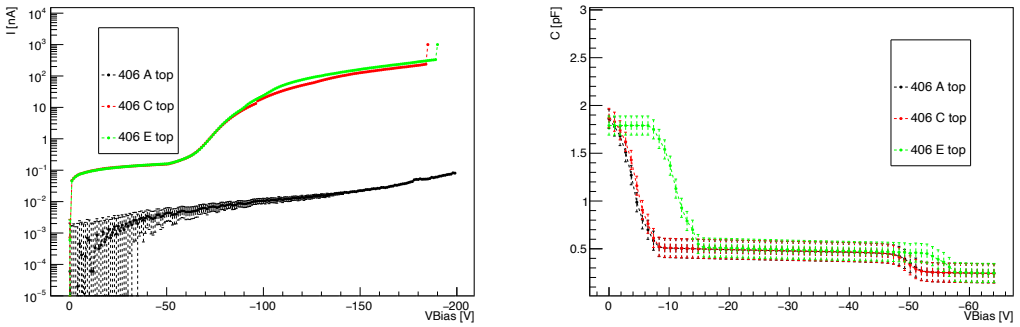

Figure A.24: I-V (left) and C-V (right) characteristics of pixel device number 406.

Bibliography

[1] I. Belyaev, G. Carboni, N. Harnew, C. Matteuzzi, F. Teubert. The history of lhcb. January 13, 2021.

[2] Measurement of charged particle multiplicities and densities in pp collisions at $\sqrt{s} = 7$ tev in the forward region. April 30, 2014.

[3] Emma Buchanan. Spatial resolution studies for the lhcb velo upgrade. October 2018.

[4] R. Aaij et al. Performance of the lhcb vertex locator. *JINST 9 P09007*, 2014.

[5] LHCb Calorimeter group. Calibration and performance of the lhcb calorimeters in run 1 and 2 at the lhc. August 26, 2020.

[6] G. Martellotti. Performance of the lhcb muon system.

[7] Federico Alessio. The lhcb upgrades for run3 and run4. 2020.

[8] Alessio Piucci. The lhcb upgrade. *J. Phys.: Conf. Ser. 878 012012*, 2017.

[9] Martin van Beuzekom. Vertex detector for lhcb upgrade-ii. December 11, 2020.

[10] The LHCb collaboration. Expression of Interest for a Phase-II LHCb Upgrade. February 8, 2017.

[11] Donald A. Neamen. *Semiconductor Physics and Devices: Basic Principles*. McGraw-Hill, 2003.

[12] Sherwood Parker Cinzia Da Vià, Gian-Franco Dalla Betta. *Radiation Sensors with 3D Electrodes*. CRC Press, 2019.

[13] The TIMESPOT project. *https://web.infn.it/timespot/*.

[14] G.T. Forcolin, M. Boscardin, F. Ficorella, A. Lai, A. Loi, R. Mendicino, S. Ronchin, G.-F. Dalla Betta. 3D trenched-electrode pixel sensors: Design, technology and initial results. *Nuclear Inst. and Methods in Physics Research*, A 981 (2020) 164437, July 18, 2020.

[15] Hartmut F.-W. Sadrozinski, Abraham Seiden, Nicolò Cartiglia. 4-dimensional tracking with ultra-fast silicon detectors.

[16] Roberto Mendicino, Giulio Tiziano Forcolin, Maurizio Boscardin, Francesco Ficorella, Adriano Lai, Angelo Loi, Sabina Ronchin, Stefania Vecchi, Gian-Franco Dalla Betta. 3D trenched-electrode sensors for charged particle tracking and timing. *Nuclear Inst. and Methods in Physics Research*, A 927 (2019) 24–30, February 13, 2019.

[17] Claudio Piemonte. Device simulations of isolation techniques for silicon microstrip detectors made on p-type substrates. *IEEE TRANSACTIONS ON NUCLEAR SCIENCE*, VOL. 53, NO. 3, JUNE 2006.

[18] M. Angelonea, G. Battistoni, F. Bellini, V. Bocci, F. Collamati, E. De Lucia, R. Faccini, F. Ferroni, S. Fiore, M. Marafini, D. Materazzo, I. Mattei, S. Morganti, V. Patera, L. Piersanti, M. Pillon, L. Recchia, A. Russomando, A. Sarti, A. Sciubba, E. Solfaroli Camillocci, C. Voena. Properties of para-terphenyl as detector for α, β and γ radiation. May 2, 2013.

[19] Introduction to sipm, technical note. 2011.

[20] Maurizio Boscardin, Sara Ferrari, Francesco Ficorella, Adriano Lai, Roberto Mendicino, Marco Meschini, Sabina Ronchin, Md. Arif Abdulla Samy and Gian-Franco Dalla Betta. Advances in 3D Sensor Technology by Using Stepper Lithography. *Frontiers in Physics*, Volume 8, Article 625275, January 2021.

[21] G. Kramberger, V. Cindro, D. Flores, S. Hidalgo, B. Hiti, M. Manna, I. Mandić, M. Mikuž, D. Quirion, G. Pellegrini, M. Zavrtanik. Timing performance of small cell 3D silicon detectors. *Nuclear Inst. and Methods in Physics Research*, A 934 (2019) 26–32, April 30, 2019.

[22] Bollini D. et al. The microbeam facility of the an-2000 accelerator of the laboratori nazionali di legnaro. *Nuclear Instruments and Methods in Physics Research Section A: Accelerators, Spectrometers, Detectors and Associated Equipment*, 328, 173–176, 1993.